UV and VUV Photoionization of Some Metal Atoms and Ions

A thesis submitted for the degree of:

DOCTOR OF PHILOSOPHY

Presented to:

Dublin City University (DCU)	University of Padua (UniPD)
School of Physical Sciences	Scuola di Dottorato in Ingegneria dell'Informazione

Submitted by:

Hu Lu

B.Sc., M. Sc.

Research Supervisors

Prof. John T Costello (DCU)

Prof. Piergiorgio Nicolosi (UniPD)

Co-Supervisor

Dr. Patrick Hayden (UCD)

February 2021

Declaration

I hereby certify that this material, which I now submit for assessment on the programme of study leading to the award of Doctor of Philosophy is entirely my own work, that I have exercised reasonable care to ensure that the work is original, and does not, to the best of my knowledge, breach any law of copyright, and has not been taken from the work of others save and to the extent that such work has been cited and acknowledged within the text of my work.

Signed: ___ Hi Lu ____

ID No.: 13212577

Date: 25/02/2021

Acknowledgements

Firstly, I would like to thank my supervisor Prof. John Costello for giving me the opportunity to undertake this research. His constant support, help and encouragement over these years make this work possible. I would also like to thank Dr. Paddy Hayden for his continued support and advice throughout the PhD.

I would like to thank Prof. Piergiorgio Nicolosi for giving me the opportunity to work in the University of Padova and his help and support while I was in Padova. Sincere thanks to Dr. Daniele Scarpa for the kind help in the lab.

Thanks to all the members of the group – Ares, Muhammad, Mossy, Stephen, Sadaf, Colm, Get, Pramod and many others. It was a pleasure working with you and I wish you all the best. I would like to extend my thanks to all the support staff in physics department and the NCPST.

I would like to thank my friend Andrew for his help and support during my study.

Finally, I would like to thank my family. Thanks for your continued support and encouragement. I appreciate it so much.

Abstract

UV and VUV Photoionization of Some Metal Atoms and Ions

The first part of the thesis concerns a study of vacuum ultraviolet (VUV) photoabsorption spectroscopy of metal atoms and ions using laser plasma generated continuum radiation at DCU. Photoabsorption spectra have been measured using the Dual Laser Plasma (DLP) photoaborption technique. Using this technique, the absorption spectra of lowly charged ions of lead and bismuth have been obtained. Then calculations with a relativistic time dependent local density approximation (RTDLDA) code are used to reproduce the overall spectral shapes of the spectra. Also, the calculations with the Cowan suite of atomic structure codes are used to identify unknown lines in the spectra. The simulated spectra broadened with our instrumental function are used to compared with experimental spectra and new features which are due to photoabsorption from both ground state and excited states of the Pb^+, Bi^+ and Bi^{2+} ions are identified.

The second part of the project was focused on optogalvanic spectroscopy (OGS) of molybdenum atoms. Three-step, two colour ionization of Mo was performed using a molybdenum hollow cathode lamp as the atomic Mo sample. Both the slow and fast optogalvanic signals were measured. There are few OGS studies of Mo in the literature the current study represents, to the best of the author's knowledge, the first multicolour OGS study on Mo. The experiments were carried out at the Legnaro National Laboratories (LNL-INFN), Padova, Italy in the SPES (Selective Production of Exotic Species) laboratory. The focus is on isotope selection using tuned (resonant) laser ionization techniques of atomic vapours or the so-called AVLIS (atomic vapour laser ionization separation) technique. The experiments were designed to prove OGS as a simple and economic sensor for laser tuning. Specifically, the wavelength dependence of both 'fast' and 'slow' optogalvanic signals was studied, where the former comes from photo-generated electrons emitted during the laser pulse(s) and the latter originates from ion population redistribution following the laser pulse(s). Both the slow and fast optogalvanic signals are suitable for instantaneous laser tuning (and both are selective), however the former yields higher signal to noise ratios (SNRs).

Sintesi

Fotoionizzazione UV e VUV di Alcuni Atomi e Ioni Metallici

La prima parte della tesi riguarda uno studio della spettroscopia di fotoassorbimento nell'ultravioletto da vuoto (VUV) di atomi e ioni metallici utilizzando radiazione a spettro continuo generata da plasma laser presso DCU. Gli spettri di fotoassorbimento sono stati misurati utilizzando la tecnica di fotoassorbimento cosiddetta a due plasmi (DLP). Utilizzando questa tecnica, sono stati ottenuti gli spettri di assorbimento di ioni a bassa carica di piombo e bismuto. Quindi si è utilizzato un codice di calcolo basato su approssimazione della densità locale dipendente dal tempo (RTDLDA) relativistico per riprodurre gli spettri nel loro complesso. Inoltre, si è utilizzata la suite di calcolo Cowan di codici di struttura atomica per identificare righe spettrali ignote. Gli spettri simulati convoluti con la nostra funzione strumentale sono confrontati con gli spettri sperimentali così sono state identificate nuove caratteristiche spettrali dovute al fotoassorbimento sia dallo stato fondamentale che dagli stati eccitati degli ioni Pb^+, Bi^+ e Bi^{2+}.

La seconda parte del progetto si è concentrata sulla spettroscopia optogalvanica (OGS) degli atomi di molibdeno. La ionizzazione di Mo in tre passi e due colori è stata eseguita utilizzando una lampada a catodo cavo al molibdeno come campione di Mo atomico. Sono stati misurati sia i segnali optogalvanici lenti che veloci. Ci sono solo pochi studi OGS su Mo in letteratura, lo studio attuale rappresenta, per quanto ne sa l'autore, il primo studio OGS multicolore su Mo. Gli esperimenti sono stati effettuati presso i Laboratori Nazionali di Legnaro (LNL-INFN), Padova, Italia nel laboratorio SPES (Selective Production of Exotic Species). L'attenzione si concentra sulla selezione degli isotopi utilizzando tecniche di ionizzazione laser sintonizzate (risonanti) di vapori atomici, la cosiddetta tecnica AVLIS (atomic vapor laser ionization Separation). Gli esperimenti sono stati progettati per dimostrare che OGS è una tecnica semplice ed economica per la sintonizzazione laser. In particolare, è stata studiata la dipendenza dalla lunghezza d'onda dei segnali optogalvanici sia 'veloci' che 'lenti', dove il primo proviene da elettroni foto-generati emessi durante gli impulsi laser e il secondo dalla ridistribuzione della popolazione ionica dopo l'impulso laser. Entrambi i segnali optogalvanici lenti e veloci sono adatti per la sintonizzazione laser istantanea (ed entrambi sono selettivi), tuttavia il primo produce rapporti segnale / rumore (SNR) più elevati.

Contents

List of Figures

List of Acronyms

AVLIS: Atomic Vapour Laser Ionization Separation

BNCT: Boron Neutron Capture Therapy

BRV: Ballofet, Romand, and Vodar

CCD: Charge-Coupled Device

CEMA: Channel Electron Multiplier Array

DLP: Dual Laser Plasma

EBIT: Electron Beam Ion Trap

EUV/XUV: Extreme Ultraviolet

EURISOL: European Isotope Separation On-Line facility

FWHM: Full Width at Half-Maximum

HCL: Hollow Cathode Lamp

HF: Hartree-Fock

HHG: High Harmonic Generation

ISOL: Isotope Separation On-Line

KDP: Potassium Dihydrogen Phosphate

LDA: Local Density Approximation

LHD: Large Helical Device

MOLAS: MOlybdenum production with LASer technique

MOS: Metal-Oxide Semiconductor

OGS: Optogalvanic Spectroscopy

PDA: Photo Diode Array

RFQ: Radio-Frequency Quadrupole

RIBs: Radioactive Ions Beams

RILIS: Resonant Ionization Laser Ion Source

RIS: Resonance Ionization Spectroscopy

RTDLDA: Relativistic Time-Dependent Local Density Approximation

SFG: Sum Frequency Generation

SPES: Selective Production of Exotic Species

TDLDA: Time-Dependent Local Density Approximation

ToF-MS: Time of Flight Mass Spectrometer

UCx: Uranium Carbide

UV: Ultraviolet

VUV: Vacuum Ultraviolet

ZEKE: Zero Electron Kinetic Energy

List of Tables

Chapter 1 Introduction

1.1 Early Development of VUV/EUV Photoionization

It is challenging both experimentally and theoretically to study the interaction of short wavelength photons with atoms and ions in the vacuum ultraviolet and extreme ultraviolet spectral regions. Individual photons have enough energy to excite either inner-shell electrons or more than one electron at a time at these wavelengths. However, photoabsorption experiments performed at these wavelengths have provided important data for the interpretation of atomic and ionic processes in laboratory and astrophysical plasmas, information on the inverse processes of radiative and dielectronic recombination for modelling astrophysical and laboratory plasmas [1], and data on single and multiple charged ions to understand photon interactions with solids etc [2].

Successive improvements in instrumentation and light sources have helped scientists to study the interaction of short wavelength radiation with atoms and ions experimentally. In 1893 Schumann [3] built the first vacuum spectrograph using a fluorite prism as the dispersive element. He also introduced the use of the 'Schumann' photographic plate which possessed a very low gelatin content. He reached wavelengths as short as 125 nm, however he was unable to measure the short wavelengths observed because the dispersion curve of fluorite was not known at that time. Lyman [4,5] was the first to make wavelength measurements in the vacuum ultraviolet (VUV) by using a concave diffraction grating in his vacuum spectrograph. This enabled him to measure wavelengths and so to place a wavelength scale on Schumann's H_2 spectrum, demonstrating that Schumann certainly reached 126.7 nm, and perhaps 123 nm. Lyman [6] then discovered the principal series in hydrogen in 1914. The first member of the principal series in hydrogen lies at a wavelength of 121.6 nm. The Lyman series provided an important confirmation of the Bohr [7] theory of the atom. The principal series of helium was observed in Lyman's later work [8,9], along with the series limit at 50.4 nm along with the continuum beyond that limit and he, in fact, reached wavelengths as short as 25 nm with this spectrograph. The extreme ultraviolet

(EUV/XUV) spectrum of helium and the series limit confirmed conclusively the energy levels and ionization potential of He obtained by Franck [10] by the electron impact method. The helium inter-combination line $1s^2\ ^1S - 1s2p\ ^3P$, produced by a transition from the first excited level of orthohelium to the ground state of parahelium, was recorded and identified.

In 1924 Millikan and Bowen [11] observed the spectra of many highly stripped atoms using a vacuum spark [12] as a light source and showed that they could be arranged into isoelectronic sequences. Elements were introduced in the form of solid compounds inserted in holes in the electrodes. They detected very faint lines with wavelengths as short as 14 nm using the combination of a vacuum spark source and gratings with good reflectivity. Due to the rapid fall off in reflectivity with decreasing wavelength, they did not detect extremely short wavelengths. The gap between X-rays and the XUV remained open until Osgood [13] constructed the first grazing incidence concave grating spectrograph and observed spectra extending from 21.5 nm down to the K_{α} X-ray line of carbon at 4.4 nm in 1927. Dauvillier [14] bridged from X-ray spectra to the XUV at 12.1 nm using a fatty acid crystal of large grating space in the same year. The gap was closed, and the stage was set for the exploration of spectra of atoms in many stages of high ionization. Edlen and his collaborators [15] studied the spectra of highly stripped ions and established the energy levels of many atoms in different stages of ionization using the vacuum spark source. One major achievement during this period was the proof in 1942 that the sun's corona was at a temperature of the order of one million degrees [16]. This work completely changed our picture of the sun's atmosphere. The author was able to show that the spectral lines in the solar corona were in fact due to transitions occurring between levels in the ground terms of highly stripped atoms.

Many new light emission sources became available in the following years. A large number of plasma sources were developed due to controlled fusion research and some of them had been used as spectroscopic sources [17]. Fawcett et al. [18] found that an extremely versatile spectral line source was formed when a Q-switched laser pulse was focused onto a target in vacuum to produce a hot dense plasma. This spectral line source could be used to study the high ion stages of almost all elements. Laser produced plasmas [19] had been introduced for the generation and identification of many spectral lines found in astrophysical sources including the sun and in fusion plasmas.

Many light sources had been developed to carry out photoabsorption studies as well. Absorption spectroscopy can provide access to transitions where the upper level is strongly autoionizing such as inner-shell or multiple electron excitations or where photoionization continua are investigated. These atomic and ionic levels usually do not show up in emission spectra. The continuous spectrum emitted by a hydrogen discharge was the first to be used as a practical continuum background source for absorption spectroscopy in the VUV. In 1924 Lyman [8] introduced a new continuum source produced by a short duration capacitor-discharge through a low-pressure gas contained in a glass capillary of small internal diameter (~ 1 mm). Wavelengths as short as 90 nm were observed with this continuum source. In 1935 Beutler [20] found numerous absorption lines attributable to excitation of inner-shell electrons and subject to autoionization phenomena. He made his measurements in the 60 - 100 nm spectral range using, as a background source, the Hopfield [21] continuum of helium. The BRV spark discharge source was developed by Ballofet, Romand, and Vodar in 1961 [22] and is named after its inventors. The anode consisted of a high Z material, usually uranium. A continuum emission spectrum (from the visible down to the XUV (~8 nm)) was produced by using a low inductance circuit to connect the discharge capacitors to the spark gap. In 1969 Garton et al. [23] recorded the absorption spectra of neutral metal atoms over a wide spectral range (12 – 65 nm) using a BRV source in conjunction with a containment device for metal vapours. Cantu and Tondello [24] extended the source to the 13-50 nm spectral range by adding a narrow capillary made of insulating material to the tip of the anode in 1975.

1.2 Synchrotron Radiation Sources

In the 1960s synchrotron radiation was pioneered as a suitable photon source for inner shell studies [25,26]. As synchrotrons of higher energy were built, the major energy loss mechanism was found to be due to the emission of radiation as the charged particles undergo centripetal acceleration. The loss mechanism sets an upper limit on the energies achievable in synchrotrons (Iwanenko and Pomeranchuk [27]). Schwinger [28] published his detailed calculations on synchrotron radiation theory based on classical concepts in 1949. The calculations showed that the spectrum extends into the X-ray region for E ~ 1 GeV. In 1956, Tomboulian and Hartman [29] made some measurements using the radiation from the 300 MeV electron synchrotron at Cornell. They pointed out the advantages of such a source for absorption spectroscopy studies in the ultra-soft X-ray (or XUV) region.

The loss mechanism of synchrotron radiation [27] is being employed in important experiments involving the interaction of XUV and VUV radiation (1 – 100 nm) with atoms in the free and bound states. In 1961, the National Bureau of Standards in Washington modified its 180 MeV synchrotron for use as a synchrotron radiation facility. Madden and Codling [30] reported new autoionizing levels in helium, neon and argon in the 18-47 nm region using this facility in 1963. The Stoughton (Wisconsin) [31] storage ring was repurposed solely as a source of XUV radiation in 1969, while the 2.5 GeV Bonn synchrotron was used as a background continuum source for VUV to X-ray photoabsorption experiments on gases and vapours [32] Advances in synchrotron radiation sources have since played an important role in further studies of doubly excited helium [33] and in double ionization measurements [34]. Through successive generations of development, synchrotron radiation sources have exploited magnetic wiggler and undulator beamlines to provide even more intense photon beams [35]. Early studies on photoionization of ions at synchrotrons suffered from weak signal rates due to the low currents achievable in the target beams. Measurements at third generation synchrotron sources such as SOLEIL [36], ALS [37] and PETRA III [38] led the way to the partial resolution of this issue as a result of the increased brightness of the sources.

1.3 Development of the Dual Laser Plasma (DLP) Photoabsorption Technique

When a high-power laser beam is focused onto a solid target in vacuum, a high temperature, high density, short-lived plasma is formed. For light or medium atomic number targets the emission consists mainly of discrete spectral lines. If a high atomic number target such as tungsten or a rare-earth target is used, then a clean and relatively uniform continuum is emitted throughout the VUV and EUV spectral regions. A series of time-resolved and time-integrated spectroscopic measurements were carried out by Carroll and co-workers [39,40] who found that the elements from samarium to ytterbium all exhibit strong, line free and extensive continuum emission in the XUV spectral region. This laser plasma continuum is ideal for a wide range of absorption experiments at short wavelengths. When used as a back-lighting source with a second laser generated plasma which creates the absorbing atomic or ionic species of interest, the combination provides a flexible approach to the study of inner-shell and multiple electron excitations in atoms and ions [41]. The technique, termed the dual laser plasma (DLP) photoabsorption technique, has been used to investigate the VUV/EUV photon interactions in a wide range of atoms and ions. The method is versatile as solid targets are used and even refractory elements can be explored.

The first DLP experiment was carried out by Carillon et al. [42] in 1970. Line emission, with a small number of narrow bands (≤ 1 nm) of featureless continuum, dominates aluminium plasma emission in the XUV region and therefore they used these regions to perform the DLP experiments. These continuum bands were absorbed by a second aluminium plasma. Both plasmas were produced by splitting a single Nd: YAG laser pulse (1J, 40 ns FWHM (full width at half-maximum)) into two laser pulses. The first laser pulse was used to produce the absorbing plasma and the second pulse, which was delayed with respect to the first, was used to produce the continuum source.

In 1977 Carroll and Kennedy [43] carried out a DLP experiment on Li^+. A single Ruby laser pulse (1J, 30-40 ns), split into two parts, was used to create both plasmas, where a high-Z metal tungsten target was used to generate a broadband

XUV continuum in the 5 to 20 nm region, which was then used to probe the absorbing plasma (containing Li^+ ions). They photographically captured the doubly excited $1s^2\ {}^1S_0 \rightarrow 2snp\ {}^1P_1$ series of He-like lithium for the first time and the photoabsorption spectrum of the principal series $1s^2\ {}^1S_0 \rightarrow 1snp\ {}^1P_1$ (up to n=7) of Li^+ was also observed. Key et al. [44] developed the DLP technique in the X-ray region in 1978. They used the X-ray emission from a brass (Cu+Zn) target as the backlighting source to study pulsed laser induced implosion of neon-filled glass micro-balloon targets.

In 1986 Carroll and Costello [45] improved the capabilities of the DLP technique in the XUV region with the introduction of a second laser. The power density on the target was increased by using two independent time-synchronized lasers. A small fraction of the first Q-switched laser pulse was directed to a fast photodiode that triggered an electronic delay generator. After a pre-set delay, an electronic pulse was sent to trigger the Pockels cell of the second Q-switched laser. The inter-plasma time delay could be varied over a wide range (0.25→100 μs). Carroll and Costello obtained the profile of the $5d \rightarrow \varepsilon f$ giant dipole resonance in atomic thorium [45] and uranium [46] using this improved version of the DLP technique. Costello et al. [47] performed a DLP photoabsorption experiment on silicon. They observed spectra due to 2p-subshell excitation from metastable quartet states of the $2p^63s3p^2$ electron configuration. The transitions $2p^63s3p^2$ - $2p^53s^23p^2$ were measured and compared to a spectrum synthesized with computed data. Further reviews about the early development of the laser plasma continuum source were provided by Costello et al. [48] and Kennedy et al. [42]. The Padova group of Tondello, Nicolosi and coworkers have used the DLP technique combined with multichannel XUV photon detection via an intensified photo diode array to investigate the interaction of ionizing radiation with few electron ions of light elements such as carbon [49], since the 80s. For example, the photoionization cross-section of C^+ was measured with the DLP technique by Nicolosi and Villoresi [50]. Recanatini and coworkers [51] extended the measurements, recording photoabsorption spectra from both the ground (${}^2P^0$) and the first excited (${}^4P$) levels in 2001.

1.4 Summary

This chapter describes the early development of VUV/EUV photoionization and the evolution of synchrotron radiation sources. The history of the dual laser plasma (DLP) technique is introduced at the end of this chapter.

References

[1] M. C. Weisskopf, The Chandra X-Ray Observatory: An overview. *Adv. Space Res.* **32**, 2005 (2003)

[2] S. P. Hatchett, C. G. Brown, T. E. Cowan, E. A. Henry, J. S. Johnson, M. H. Key, J. A. Koch, A. B. Langdon, B. F. Lasinski, R. W. Lee, A. J. Mackinnon, D. M. Pennington, M. D. Perry, T. W. Phillips, M. Roth, T. C. Sangster, M. S. Singh, R. A. Snavely, M. A. Stoyer, S. C. Wilks, and K. Yasuike, Electron, photon, and ion beams from the relativistic interaction of Petawatt laser pulses with solid targets. *Phys. Plasmas* **7**, 2076 (2000)

[3] V. Schumann, Über die Photographie der Lichtstrahlen kleinster Wellenlängen. *Sitzungsber. Akad. Wiss. Wien*, **102**, Abth. II a, 415 (1893)

[4] T. Lyman, The spectrum of hydrogen in the region of extremely short wavelength. *Mem. Am. Acad. Arts Sci. New Ser.* **13**, 125 (1906)

[5] T. Lyman, Preliminary measurement of the short wavelengths discovered by Schumann. *Astrophys. J.* **19**, 263 (1904)

[6] T. Lyman, An extension of the spectrum in the extreme ultraviolet. *Nature* **93**, 241 (1914)

[7] N. Bohr, On the Stability of Atoms and Molecules. Pt. III Systems with few Nuclei. *Phil. Mag.*, Ser. 6, **26**, 1 (1913)

[8] T. Lyman, The spectrum of helium in the extreme ultraviolet. *Astrophys. J.* **60**, 1 (1924)

[9] T. Lyman, The Spectroscopy of the Extreme Ultraviolet. 2nd Edition. Longmans, Green, New York (1928)

[10] J. Franck, Bemerkung über Anregungs- und Ionisierungsspannung des Heliums. *Z. Physik* **11**, 155 (1922)

[11] R. A. Millikan, I. S. Bowen, Extreme ultra-violet spectra. *Phys. Rev.* **23**, 1 (1924)

[12] R. A. Millikan, R. A. Sawyer, Extreme ultra-violet spectra of hot sparks in high vacuum. *Phys. Rev.* **12**, 167 (1918)

[13] T. H. Osgood, X-ray spectra of long wavelength. *Phys. Rev*. **30**, 567 (1927)

[14] A. Dauvillier, La spectrographie des rayons X de grande longueur d'onde. Séries N et O, et jonction avec l'ultraviolet extreme. *J. Phys*. Radium **8**, 1 (1927)

[15] B. Edlen, Wavelength measurements in the vacuum ultraviolet. *Rep. Prog. Phys.* **26**, 181 (1963)

[16] B. Edlen, Interpretation of the emission lines in the spectrum of the solar corona. *Z. Astrophys.* **20**, 30 (1942)

[17] A. H. Gabriel, Plasma Light Sources. *Nucl. Instrum. Meth.* **90**, 157 (1970)

[18] B. C. Fawcett, A. H. Gabriel, F. E. Irons, N. J. Peacock and P. A. H. Saunders, Extreme ultra-violet spectra from laser-produced plasmas. *Proc. Phys. Soc.* **88**, 1051 (1966)

[19] M. Richardson, In: J. A. Samson, D. L. Ederer (Eds.), Vacuum Ultraviolet Spectroscopy. Academic Press, New York (2000)

[20] H. Beutler, Über Absorptionsserien von Argon, Krypton und Xenon zu Termen zwischen den beiden Ionisierungsgrenzen ${}^{2}P_{3}^{2/O}$ und ${}^{2}P_{1}^{2/O}$. *Z. Physik* **93**, 177 (1935)

[21] J. J. Hopfield, Absorption and emission spectra in the wavelength region 600-1100 Å. *Phys. Rev*. **35**, 1133 (1930)

[22] G. Ballofet, J. Romand, B. Vodar, Emission source of continuous spectra extending from the visible to the far ultraviolet. *Compt. Rend.* **252**, 4139 (1961)

[23] W. R. S. Garton, J. P. Connerade, M. W. D. Mansfield, J. E. G. Wheaton, Atomic absorption spectroscopy in the 100-600 Å wavelength range. *Appl. Opt*. **8**, 919 (1969)

[24] A. M. Cantu, G. Tondello, Continuum source and focusing technique for the 80-500 Angstrom spectral range: improvements. *Appl. Opt*. **14**, 996 (1975)

[25] K. Codling, Applications of synchrotron radiation (ultraviolet spectral light source). *Rep. Prog. Phys*. **36**, 541 (1973)

[26] R. Tousey, The extreme ultraviolet-past and future. *Appl. Opt.* **1**, 679 (1962)

[27] D. Iwanenko and I. Pomeranchuk, On the maximal energy attainable in a betatron. *Phys. Rev.* **65**, 343 (1944)

[28] J. Schwinger, On the classical radiation of accelerated electrons. *Phys. Rev.* **75**, 1912 (1949)

[29] D. H. Tomboulian, P. L. Hartman, Spectral and angular distribution of ultraviolet radiation from the 300-Mev Cornell synchrotron. *Phys. Rev*. **102**, 1423 (1956)

[30] R. P. Madden, K. Codling, New autoionizing atomic energy levels in He, Ne and Ar. *Phys. Rev. Lett*. **10**, 516 (1963)

[31] D. W. Lynch, Tantalus, A 240 MeV dedicated source of synchrotron radiation. 1968-1986. *J. Synchrotron Rad*. **4**, 334 (1997)

[32] J. Hormes, Synchrotron radiation laboratories at the Bonn electron accelerators. A status report. *Phys. Scr.* **36,** 36 (1987)

[33] K. Schulz, G. Kaindl, M. Domke, J. D. Bozek, P. A. Heimann, A. S. Schlachter, J. M. Rost, Observation of new Rydberg series and resonances in doubly excited helium at ultrahigh resolution. *Phys. Rev. Lett.* **77**, 3086 (1996)

[34] J. H. McGuire, N. Berrah, R. J. Bartlett, J. A. R. Samson, J. A. Tanis, C. L. Cocke, A. S. Schlachter, The ratio of cross-sections for double to single ionization of helium by high energy photons and charged particles. *J. Phys. B: At. Mol. Opt. Phys.* **28**, 913 (1995)

[35] H. Wiedemann, Particle Accelerator Physics I. Springer, Berlin (1993)

[36] M. F. Gharaibeh, J. M. Bizau, D. Cubaynes, S. Guilbaud, N. El Hassan, M. M. Al Shorman, C. Miron, C. Nicolas, E. Robert, C. Blancard and B. M. McLaughlin, K-shell photoionization of singly ionized atomic nitrogen: experiment and theory. *J. Phys. B At. Mol. Opt. Phys.* **44**, 175208 (2011)

[37] A. M. Covington, A. Aguilar, I. R. Covington, M. F. Gharaibeh, G. Hinojosa, C. A. Shirley, R. A. Phaneuf, I. Álvarez, C. Cisneros, I. Dominguez-Lopez, M. M. Sant'Anna, A. S. Schlachter, B. M. McLaughlin, and A. Dalgarno, Photoionization of Ne^+ using synchrotron radiation. *Phys. Rev. A* **66**, 062710 (2002)

[38] S. Schippers, S. Ricz, T. Buhr, J. Hellhund, A. Müller, S. Klumpp, M. Martins, R. Flesch, E. Rühl, J. Lower, T. Jahnke, D. Metz, L. Ph H. Schmidt, R. Dörner, J. Ullrich and A. Wolf, Photon-ion spectrometer PIPE at the variable polarization XUV beamline of PETRA III. *J. Phys. Conf. Ser.* **388**, 142016 (2011)

[39] P. K. Carroll, E. T. Kennedy, G. O'Sullivan, Laser-produced continua for absorption spectroscopy in the VUV and XUV. *Appl. Opt.* **19**, 1454 (1980)

[40] P. K. Carroll, G. O'Sullivan, Ground state configurations of ionic species I though XVI for Z =57 -74 and the interpretation of 4d-4f emission resonances in laser produced plasmas. *Phys. Rev. A*. **25**, 275 (1982)

[41] E. T. Kennedy, J. T. Costello, J. P. Mosnier, P. van Kampen, VUV/EUV ionizing radiation and atoms and ions; dual laser plasma investigations. *Rad. Phys. Chem*. **70**, 291 (2004)

[42] A. Carillon, P. Jaégle and P. Dhez, Extreme ultraviolet continuum absorption by a laser generated aluminium plasma. *Phys. Rev. Lett.* **25**, 140 (1970)

[43] P. K. Carroll and E. T. Kennedy, Doubly excited autoionization resonances in the absorption spectrum of Li^+ formed in a laser-produced plasma. *Phys. Rev. Lett*. **38**, 1068 (1977)

[44] M. H. Key, C. L. S. Lewis, J. G. Lunney, A. Moore, T. A. Hall, and R. G. Evans, Pulsed-X-ray shadowgraphy of dense, cool, laser-imploded plasma. *Phys. Rev. Lett.* **41**, 1467 (1978)

[45] P. K. Carroll and J. T. Costello, Giant-dipole-resonance in atomic thorium by a novel two-laser technique. *Phys. Rev. Lett.* **57**, 1581 (1986)

[46] P. K. Carroll and J. T. Costello, The XUV photoabsorption spectrum of uranium vapour. *J. Phys. B* **20**, 201 (1987)

[47] J. T. Costello, E. T. Kennedy, J-P Mosnier, M. H. Sayyad and C. McGuiness, Extreme-UV photoabsorption spectrum of a laser-produced silicon plasma: evidence for metastable Si^+ ions. *J. Phys. B: At. Mol. Opt. Phys.* **31**, L547 (1998)

[48] J. T. Costello, J. P. Mosnier, E. T. Kennedy, P. K. Carroll, G. O'Sullivan, XUV absorption spectroscopy with laser-produced plasmas: a Review. *Phys. Scr.* **T34**, 77 (1991)

[49] E. Jannitti, P. Nicolosi, G. Tondello, Absorption spectra from 1s inner-shell electron of ionized and neutral carbon. *Phys. Scr.* **41**, 458 (1990)

[50] P. Nicolosi and P. Villoresi, Experimental measurement of the CII L-shell photoabsorption spectrum. *Phys. Rev. A* **58**, 4985 (1998)

[51] P. Recanatini, P. Nicolosi, P. Villoresi, ^2P and ^4P CII photoabsorption spectra. *Phys. Rev. A* **64**, 012509 (2001)

Chapter 2 Theory

2.1 The Structure of Multi-electron Atoms

2.1.1 The Schrödinger Equation

The starting point of all calculations on many-electron atoms is the central field approximation. The basic idea of this approximation is that, for an atom or ion containing a nucleus of charge Ze and N electrons, each of the atomic electrons moves in an effective spherically symmetric potential created by the nucleus and all the other electrons. They should take account of the kinetic energy of the electrons and their potential energy in the Coulomb field of the nucleus, the Coulomb force between the electrons, the spin-orbit interaction and spin-spin interactions between the electrons along with various relativistic effects, radiative corrections and nuclear corrections [1].

For the sake of simplicity only the attractive Coulomb interaction between the electrons and the nucleus (which we assume to be infinitely heavy), the Coulomb repulsions between the electrons and the spin-orbit interactions are included in what follows. Then the Hamiltonian of the N-electron atom (ion) in the absence of an external field is

$$H = \sum_{i=1}^{N}(-\frac{1}{2}\nabla_{r_i}^2 - \frac{Z}{r_i} + \xi_i(r_i)(\boldsymbol{l}_i \cdot \boldsymbol{s}_i)) + \sum_{i<j=1}^{N}\frac{1}{r_{ij}} \qquad (2.1)$$

Where r_i denotes the distance of the electron i from the nucleus, $r_{ij} = |\boldsymbol{r}_i - \boldsymbol{r}_j|$ is the separation between electrons '*i*' and '*j*' and the second summation is over all pairs of electrons. This expression assumes that the nucleus can be treated as a point charge with infinite mass. The spin-orbit interaction term $\xi_i(r_i)(\boldsymbol{l}_i \cdot \boldsymbol{s}_i)$ represents the sum over all electrons of the magnetic interaction energy between the spin of an electron and its own orbital motion. It involves the angular portion of the wavefunction through the operators l and s, and has a pronounced effect on the energy-level structure. It is necessary to retain it explicitly in the Hamiltonian. The proportionality factor ξ_i is measured in Rydbergs and is given by

$$\xi_i(r_i) = \frac{\alpha^2}{2}\frac{1}{r_i}(\frac{dV}{dr_i}) \tag{2.2}$$

where α is the fine structure constant (ca. 1/137) and $V(r)$ is an appropriate potential energy function for an electron in a multi-electron atom. For a stationary system such as an unperturbed atom, the Schrödinger equation can be written as

$$H\Psi^k = E^k\Psi^k \tag{2.3}$$

where *H* is the Hamiltonian for the system. The wavefunction Ψ^k and the energy E^k for every stationary state k of interest can be obtained by solving this equation. The total wavefunction is a function of $4N$ variables, three space and one spin coordinate for each electron. Exact solutions for the Schrödinger equation are known only for $N = 1$. For $N \geq 2$, exact solutions cannot be obtained at all and approximations of one sort or another are required. Hylleraas [2] generated accurate results for the ground state of helium using coordinates in 1929. Other forms of wavefunctions have been specifically chosen since [3,4]. The basic procedure consists of expanding the unknown wavefunction Ψ^k in terms of a set of known orthonormal basis functions Ψ_b:

$$\Psi^k = \sum_b y_b^k \, \Psi_b \tag{2.4}$$

Typically, the Ψ_b are calculated using a Hartree-Fock (HF) procedure. It should be chosen to preserve the accuracy of the calculations. The basis set has an infinite number of members and so, in practice, it is necessary to truncate the series to a finite number *M* of basis functions. Substituting equation 2.4 into 2.3 gives

$$\sum_{b'=1}^{M} H y_{b'}^k \, \Psi_{b'} = E^k \sum_{b'=1}^{M} y_{b'}^k \, \Psi_{b'} \tag{2.5}$$

Multiplying this from the left by Ψ_b and integrating over all $3N$ space coordinates, one can obtain

$$\sum_{b'=1}^{M} H_{bb'} y_{b'}^{k} = E^{k} \sum_{b'=1}^{M} y_{b'}^{k} < \Psi_b | \Psi_{b'} > \tag{2.6}$$

$$= E^{k} y_{b}^{k} \quad (1 \leq b \leq M)$$

Where $H_{bb'} \equiv < \Psi_b | H | \Psi_{b'} >$. The relations in equation 2.6 represent a set of M simultaneous linear equations in the *M* unknowns $y_{b'}^{k}$. This set of equations has a non-trivial solution only if the determinant of the matrix $(H_{bb'} - E^{k}\delta_{bb'})$ is zero.

$$|H - E^{k} I| = 0 \tag{2.7}$$

where I is the identity matrix. Expanding this determinant into a polynomial of degree M in E^k, zeros represent M different possible energy levels of the atom. Each of the values of E^k, substituted back into equation 2.5, gives $M - 1$ independent equations for the $M - 1$ ratios.

$$\frac{y_b^k}{y_b^i}, b \neq i \tag{2.8}$$

The value of y_b^i is chosen as

$$\sum_{b=1}^{M} |y_b^k|^2 = 1 \tag{2.9}$$

So that Ψ^k is normalized.

$$< \Psi^k | \Psi^k > = \sum_{b} |y_b^k|^2 \tag{2.10}$$

For M > 2 the above set of equations are usually solved numerically. The set of coefficients in the expansion (Eqn. 2.4) can be written in the form of a column vector

$$Y^k = \begin{pmatrix} y_1^k \\ y_2^k \\ y_3^k \\ y_4^k \\ \cdot \\ \cdot \\ \cdot \\ y_M^k \end{pmatrix} \tag{2.11}$$

Equation 2.6 can be written as the single matrix equation

$$HY^k = E^k Y^k \tag{2.12}$$

And now the problem is to find the M eigenvalues E^k of the matrix H, together with the corresponding eigenvectors Y^k. A matrix T is used to diagonalize the Hamiltonian H in order to compute the numerical values of the matrix elements $H_{bb'}$. The k^{th} diagonal element of the diagonalized Hamiltonian matrix is the eigenvalue E^k,

$$T^{-1}HT = (E^k \delta_{kb}) \tag{2.13}$$

Once the Hamiltonian matrix elements $H_{bb'}$ are computed, the energy levels of an atom can be calculated. The computing of H is the most difficult task. It involves setting up suitable basis functions required to evaluate the matrix elements.

2.1.2 Self-Consistent Solutions and the Hartree-Fock Method

In a multi-electron atom [5], each electron moves in an effective potential which represents the attraction of the nucleus and the average effect of the repulsive interactions between this electron and the *(N-1)* other electrons. In the central field, the probability distribution of electron '*i*' can be described by a one-electron wavefunction of the form

$$\varphi_i(\boldsymbol{r}_i) = \frac{1}{r_i} P_{n_i l_i}(r_i) Y_{l_i m_{l_i}}(\theta_i, \phi_i) \sigma_{m_{l_i}}(\boldsymbol{s}_i) \tag{2.14}$$

where $\boldsymbol{r}_i$ denotes the position (r_i, θ_i, ϕ_i) of the ith electron with respect to the nucleus while its spin is denoted by $\boldsymbol{s_i}$. Here $P_{n_i l_i}(r_i)$ represents the radial part of the wavefunction, $Y_{l_i m_{l_i}}(\theta_i, \phi_i)$ represents the angular part of the wavefunction and $\sigma_{m_{l_i}}(\boldsymbol{s_i})$ represents the spin. This function differs from the hydrogenic wavefunction only in the radial term, $P_{n_i l_i}(r_i)$, which results from the change in the potential V(r) as it is no longer a simple Coulomb function. An exact analytical solution of the differential equation is therefore not possible and numerical procedures are required for the calculation of $P_{n_i l_i}(r_i)$.

From the one-electron spin-orbitals one can construct the basis function for the entire atom. The probability that an electron lies at $\boldsymbol{r}_i$ from the nucleus is $|\varphi_i(\boldsymbol{r}_i)|^2$ and so the probability distribution of all the *N* electrons is $\prod_{i=1}^{N} |\varphi_i(\boldsymbol{r}_i)|^2$. This shows that for a multi-electron atom the basis function can be written as a product of spin-orbitals

$$\Psi = \varphi_1(\boldsymbol{r}_1)\varphi_2(\boldsymbol{r}_2)\varphi_3(\boldsymbol{r}_3)\cdots\varphi_N(\boldsymbol{r}_N) \tag{2.15}$$

The drawback of this product function is that it does not obey the Pauli exclusion principle. However, this can be rectified by using a wavefunction that is antisymmetric upon interchange of any two electron coordinates. If we denote P as a permutation of the electron coordinates, such a wavefunction can be formed by taking the following linear combination of product functions

$$\Psi = (N!)^{-1/2} \sum_{P} (-1)^P \varphi_1(\boldsymbol{r_1})\varphi_2(\boldsymbol{r_2})\varphi_3(\boldsymbol{r_3})\cdots\varphi_N(\boldsymbol{r_N}) \tag{2.16}$$

The total wavefunction must be antisymmetric with respect to the exchange of two arbitrary electrons. Such an anti-symmetrized linear combination can be written as the determinant

$$\Psi = \frac{1}{N!^{1/2}} \begin{vmatrix} \varphi_1(\boldsymbol{r}_1) & \varphi_1(\boldsymbol{r}_2) & \varphi_1(\boldsymbol{r}_3) & \cdots & \varphi_1(\boldsymbol{r}_N) \\ \varphi_2(\boldsymbol{r}_1) & \varphi_2(\boldsymbol{r}_2) & \varphi_2(\boldsymbol{r}_3) & \cdots & \varphi_2(\boldsymbol{r}_N) \\ \varphi_3(\boldsymbol{r}_1) & \varphi_3(\boldsymbol{r}_2) & \varphi_3(\boldsymbol{r}_3) & \cdots & \varphi_3(\boldsymbol{r}_N) \\ \vdots & \vdots & \vdots & \vdots & \vdots \\ \varphi_N(\boldsymbol{r}_1) & \varphi_N(\boldsymbol{r}_2) & \varphi_N(\boldsymbol{r}_3) & \cdots & \varphi_N(\boldsymbol{r}_N) \end{vmatrix} \tag{2.17}$$

which automatically fulfils this demand. In particular, when two electrons are exchanged, two columns of the determinant are interchanged, which inverts the sign of the determinant. This representation of an antisymmetric multi-electron wave function is called a Slater determinant [6]. It describes the wave function of an atom with many electrons as an anti-symmetric linear combination of products of one-electron wave functions [7].

The Hartree-Fock (HF) method is a frequently used approach to solve for the radial wavefunctions. It is based on the variational principle and used to find the optimum wavefunction represented by the Slater determinant Ψ (Eqn. 2.17) of single particle radial wavefunctions that are obtained using a central field potential. This wavefunction minimizes the following energy functional

$$E[\Psi]=\frac{<\Psi|\hat{H}|\Psi>}{<\Psi|\Psi>} \tag{2.18}$$

The single electron orbitals for different quantum numbers m_l and m_s are assumed to have the same radial wavefunctions $P_{n_il_i}(r_i)$ [8], and it is called the restricted Hartree-Fock method. When the radial wavefunctions $P_{n_il_i}(r_i)$ are orthonormal, the Hartree-Fock equations can be written as [9]

$$\begin{aligned}\Bigg[-\frac{\hbar^2}{2m}\frac{d^2}{dr^2}+\frac{l_i(l_i+1)\hbar^2}{2mr^2}-\frac{Z}{r}+\sum_{j=1}^{q}\left(w_j-\delta_{ij}\right)\int_0^\infty\frac{1}{r_>}P^2_{n_jl_j}(r')dr' \\ -(w_i-1)A_i(r)\Bigg]P_{n_il_i}(r_j) \\ =\epsilon_iP_{n_il_i}(r_i)+\sum_{j(\neq i)=1}^{q}w_j[\delta_{l_il_j}\epsilon_{ij}+B_{ij}(r)]\,P_{n_jl_j}(r_j)\end{aligned} \tag{2.19}$$

Where ϵ_i, ϵ_{ij} are the Lagrange multipliers which ensure the required orthonormality between the radial functions $P_{n_il_i}(r_i)$. $A_i(r)$ and $B_{ij}(r)$ account for the direct and exchange interactions respectively. The HF equations are the same as equation 2.19 but with additional terms when the variational principle is applied to the energy of a term with a specific LS symmetry rather than to the average energy of the electron configuration E_{av}.

The first three terms in the HF equation correspond to the radial part of the Schrödinger equation for the i^{th} electron in an effective potential V_{eff}, Eqn. 2.20.

V_{eff} comprises the attractive Coulomb and repulsive centrifugal potentials. The second term in equation 2.20, V_{Cou}, corresponds to the repulsive Coulomb interaction between electron i and all other electrons. V_{exc} represents the exchange interaction which is a purely quantum mechanical effect. Thus, the i^{th} electron moves in a local potential which is the summation of three terms and is expressed as:

$$V^{i}(r) = V_{eff}(r) + V_{Cou}(r) + V_{exc}(r) \tag{2.20}$$

An iterative procedure is used in order to solve the Hartree-Fock equations within the self-consistent field (SCF) approach. At first, an initial guess of the N single electron wavefunctions, usually screened hydrogenic wavefunctions, is used to calculate the Coulomb and exchange potentials. These are used to calculate a new set of single particle radial functions $P_{n_i l_i}(r_i)$ which are in turn used to compute a new potential. The procedure is repeated until self-consistency is obtained. In this case, the energy eigenvalues of the electrons explicitly depend on the principal quantum number n and the angular momentum quantum number l. The results presented in Chapter 5 of this thesis are calculated with the aid of the Cowan Code [9] which solves the Hartree-Fock equations for multielectron atoms. More details about the Cowan code can be found in Appendix A.

2.1.3 Angular Momentum Coupling

The way the orbital angular momenta $\boldsymbol{l}_i$ and the spins $\boldsymbol{s}_i$ of the individual electrons are coupled to form the total angular momentum $\boldsymbol{J}$ of the atom depends on the energetic order of the different interactions. We will discuss two limiting cases.

a) $L - S$ Coupling

If the Coulomb terms in equation 2.1 which include the electron-nucleus and electron-electron interactions are larger than the spin-orbit interaction energy, $\xi_i(\boldsymbol{r}_i)(\boldsymbol{l}_i \cdot \boldsymbol{s}_i)$, then the orbital angular momenta l_i of the different electrons couple to yield a total orbital momentum

$$\boldsymbol{L} = \sum \boldsymbol{l}_i \text{ with } |\boldsymbol{L}| = \sqrt{L(L+1)}\hbar \tag{2.21}$$

Where $\hbar$ is the reduced Planck constant. The individual spins $\boldsymbol{s}_i$ couple to yield a total spin

$$\boldsymbol{S} = \sum \boldsymbol{s}_i \text{ with } |\boldsymbol{S}| = \sqrt{S(S+1)}\hbar \tag{2.22}$$

The total angular momentum of the atom (ion) is then given by

$$\boldsymbol{J} = \boldsymbol{L} + \boldsymbol{S} \text{ with } |\boldsymbol{J}| = \sqrt{J(J+1)}\hbar \tag{2.23}$$

This limiting coupling case is designated *L-S* coupling. The electron configuration with total orbital angular momentum ***L*** and total spin ***S*** results (depending on the coupling of ***L*** *with* ***S***) in different fine structure components of a multiplet, which only differ in their quantum number ***J***. The number of possible fine structure components equals the smaller of the two numbers *(2S+1)* or *(2L+1),* because this gives the number of possible relative orientations between the two vectors ***S*** and ***L***, and therefore the number of different couplings ***L+S=J*** [7].

The energy of a fine structure component is

$$E_J = E(n, \boldsymbol{L}, \boldsymbol{S}) + C \cdot \boldsymbol{L} \cdot \boldsymbol{S} \tag{2.24}$$

where the last term gives the coupling energy of the interaction between total orbital angular momentum ***L*** and total spin ***S***. The coupling constant *C* is given in units of [kg^{-1}m^{-2}]. Because of the vector relation

$$\boldsymbol{J}^2 = (\boldsymbol{L} + \boldsymbol{S})^2 = \boldsymbol{L}^2 + \boldsymbol{S}^2 + 2\boldsymbol{L} \cdot \boldsymbol{S} \tag{2.25}$$

we obtain for the fine structure coupling energies

$$C \cdot \boldsymbol{L} \cdot \boldsymbol{S} = \frac{1}{2} C[J(J+1) - L(L+1) - S(S+1)]\hbar^2 \tag{2.26}$$

The labelling of a fine structure component is $n^{2S+1}L_J$.

b) $j-j$ Coupling

The spin-orbit interaction becomes increasingly important as Z increases. In this case, basis functions are formed by first coupling the spin of each electron to its own orbital angular momentum, and then coupling together the various resultant angular momenta $\boldsymbol{j}_i$ to obtain the total angular momentum $\boldsymbol{J}$. In other words, the individual $\boldsymbol{l}_i$ and $\boldsymbol{s}_i$ initially couple to form the resultant angular momentum

$$\boldsymbol{j}_i = \boldsymbol{l}_i + \boldsymbol{s}_i \tag{2.27}$$

for the electron e_i. The vectors $\boldsymbol{j}_i$ for the different electrons then couple to yield the total angular momentum $\boldsymbol{J}$ of the atomic state

$$\boldsymbol{J} = \sum \boldsymbol{j}_i \tag{2.28}$$

This limiting coupling case, which is mainly observed for heavy atoms with large Z values, is called j-j coupling.

2.1.4 (R)TDLDA

The so-called Local Density Approximation (LDA) can describe the atomic ground state properties to a good extent. Specifically, Hohenberg and Kohn [10] showed that the ground state energy is expressed by a functional of the electron density $E_o[n]$ that gets its minimum value when the electron density achieves its exact ground state value in a many electron system. In density functional theory (DFT), the electron density is treated as the fundamental quantity. Despite the fact that the exact functional is unknown, Kohn and Sham [11] expressed the form of the energy functional as:

$$E_o[n] = T[n] + \int_V v(\boldsymbol{r})n(\boldsymbol{r})dr^3 + \int_V \int_{V'} \frac{v(\boldsymbol{r})n\left(\boldsymbol{r}'\right)}{|\boldsymbol{r}-\boldsymbol{r}'|}dr^3dr'^3 + E_{xc}[n] \tag{2.29}$$

where $T[n]$ is the exact kinetic energy functional for the noninteracting electrons and $v(\boldsymbol{r})$ denotes the Coulomb potential due to the nucleus. The term $\int_V \int_{V'} \frac{v(\boldsymbol{r})n(\boldsymbol{r}')}{|\boldsymbol{r}-\boldsymbol{r}'|}dr^3dr'^3$ represents the classical electrostatic Coulomb interaction between the electrons. The exchange-correlation energy functional $E_{xc}[n]$ is the only unknown quantity in this equation. The exchange energy functional $E_{xc}[n]$ is described in the so-called Local Density Approximation (LDA) as:

$$E_{xc}[n] = \int n(\boldsymbol{r})\epsilon_{xc}\,[n](\boldsymbol{r})dr^3 \tag{2.30}$$

where $\epsilon_{xc}[n](\boldsymbol{r})$ is the averaged approximated exchange-correlation energy per particle. The Kohn-Sham equation is obtained by taking the derivative of the energy functional

$$[-\Delta + v(r) + v_H[n](\boldsymbol{r}) + v_{xc}[n](\boldsymbol{r})\psi_i(\boldsymbol{r}) = \epsilon_i\psi_i(\boldsymbol{r}) \tag{2.31}$$

where $v_{xc}[n](\boldsymbol{r}) = \epsilon_{xc}[n](\boldsymbol{r}) + \frac{d\epsilon_{xc}[n]}{dn}\,n(\boldsymbol{r})$.

In order to obtain the LDA orbitals and compute the electron density, we have to solve the Kohn-Sham equation. Firstly, by analysing a homogenous electron gas, using a linear combination of Slater determinants as a wavefunction of the total electron system, the correlation part of $v_{xc}[n]$ can be obtained. Then we can obtain the photoabsorption cross section in the Local Density Approximation as an independent particle model by using Fermi's golden rule with LDA orbitals.

A natural extension of the LDA is in the direction of time-dependent processes [12]. One important case involves interaction with an external oscillating electric field, where the weakness of the interaction permits the linearization of the equations. The resulting linear response problem is entirely equivalent to self-consistent first order time-dependent perturbation theory applied to the LDA ground state and termed the time-dependent local density approximation (TDLDA). The external field induces a frequency dependent perturbation in the electron density $\delta n(\boldsymbol{r}, w)$ which can be expressed as

$$\delta n(\boldsymbol{r}, w) = \int \chi(\boldsymbol{r}, \boldsymbol{r}', w)\,\varphi(\boldsymbol{r}', \omega)d\boldsymbol{r}' \tag{2.32}$$

in the linear approximation where $\varphi(\boldsymbol{r}', \omega)$ represents the external field.

Zangwill and Soven [12] give the relationship between the induced density δn and the external field via a position and frequency dependent complex susceptibility

$\chi(\boldsymbol{r}, \boldsymbol{r}', w)$. The electrons redistribute and interact with each other via the repulsive Coulomb force in the atom and produce an internal field via the induced Coulomb potential

$$\delta V_c(\boldsymbol{r}, w) = \varrho \int \frac{\delta n(\boldsymbol{r}', w)}{|\boldsymbol{r} - \boldsymbol{r}'|} dr'^3 \tag{2.33}$$

and an induced exchange-correlation potential

$$\delta V_{xc}(\boldsymbol{r}, w) = \frac{\partial V_{xc}}{\partial n}|_{n=n_0} \, \delta n(\boldsymbol{r}, w). \tag{2.34}$$

In that case, the internal field is superimposed on the external field and the new effective field variable $R(w)$ is generated. This procedure is repeated until self-consistency is achieved. By replacing the dipole operator *r* by $R(w)$ and using LDA orbitals as single particle states, the TDLDA cross section can be obtained.

Zangwill and Liberman [13,14] have written a computer code that first solves the one-electron equations within the LDA for an atom or ion in a stationary state, which, by an iterative process, determines the self-consistent charge density and potential function. The code then solves the TDLDA equations for the absorption of radiation using a relaxation procedure. The original time-dependent local density approximation (TDLDA) code 'GOLIATH' was designed for nonrelativistic, spherically symmetric, atoms. However, aiming to account for the sizeable relativistic effects occurring in the optical response of heavy atoms [15] they have generalized the TDLDA to include the relativistic case. The computer program DAVID, which is the relativistic analog of GOLIATH, is presented in ref. [13]. Both the TDLDA and RTDLDA codes were used in this thesis to calculate the absolute cross sections of Bi and Pb atoms and ions simply to compare with the overall spectral profiles of the corresponding dual laser plasma photoabsorption spectra. More details about RTDLDA code can be found in [13,14].

2.1.5 Inner-Shell Excitation and the Auger Process

Inner shell electrons are much less screened from the nuclear charge than valence electrons and their binding energies are thus relatively larger. Inner shell excitation/ionization therefore needs energetic photons in the VUV or X-ray regime or collisions with electrons having sufficient kinetic energy to excite or ionize them. After an inner shell electron is excited or ionized, an electron from a higher state E_i can fall into the created hole to refill it. The excess energy created from this process can be emitted in the form of radiation and this, for example, is the source for the discrete X-ray emission in X-ray tubes, e.g., K_α and K_β emission features. However, the energy released, $\Delta E = E_i - E_j$, where E_i is the hole state energy and E_j is the energy of the state from which the active electron originates, can also be transferred to another electron e_2 of the same atom and this electron can leave the atom if the binding energy E_B of e_2 is smaller than ΔE.

There are two distinct cases, non-resonant and resonant. In the former case a photoelectron e_{ph} is generated leaving the atom behind as a singly charged ion. The inner shell hole is then filled by an electron from a higher lying energy state. The excess energy generated results in the release of a second electron e_A with a binding energy less than the excess energy. This electron is referred to as an Auger electron [16] and the final charge state of the ion is 2^+ (i.e., it is doubly ionized). On the other hand, a high energy photon could be tuned to an inner shell resonant state which lies in the continuum, for example Ne $1s^2 2s^2 2p^6$ ($^1S_0$) + $h\nu$ -> Ne $1s 2s^2 2p^6 3p$ ($^1P_1$) -> Ne^+ $1s^2 2s^2 2p^5$ ($^2P_{1/2,3/2}$) + eA (εs, εd). This is a resonant Auger process and the final state of the atom is singly ionized. The kinetic energy of the ejected Auger electron is

$$E_{kin} = E_i - E_j - E_B \tag{2.35}$$

Measuring this energy allows the determination of the atomic state out of which it was ionized. The Auger process and the emission of X-rays are competing processes. The fraction of all de-excitation processes involving X-ray fluorescence from an initial inner-shell excited state i to all final states j is called the fluorescence yield of state i. It depends on the state i, the charge state and the nuclear charge Ze of the atom. For $Z < 30$ the Auger process is dominant, for $Z > 60$ the fluorescence yield reaches 90%, if the excitation starts from the K shell of an initially neutral atom [7].

2.2 Interaction of Light with Matter

When an atom is exposed to light with a frequency such that the photon energy coincides with the energy difference of two energy levels, i.e., $hv = E_2 - E_1$, where E_2, E_1 and h stand for the higher and lower-level energies, and Planck's constant, respectively, the atom may absorb the photon energy transferring an electron from the lower to the higher energy state. This process is called absorption.

The atom can also emit light, but by two processes. The first is that the excited atom can undergo a process called spontaneous emission; the phase of the light is randomly distributed when referenced to the initial, exciting photon. In the second process an incident photon initiates the transition, i.e., the incident photon triggers the emission of a further photon with the atom undergoing a transition from the excited state to a lower energy state, a process called stimulated emission. In this case the 'stimulated' photon has the same phase, frequency and direction as the 'triggering' photon. Hence light amplification results. This process forms the basis for laser action.

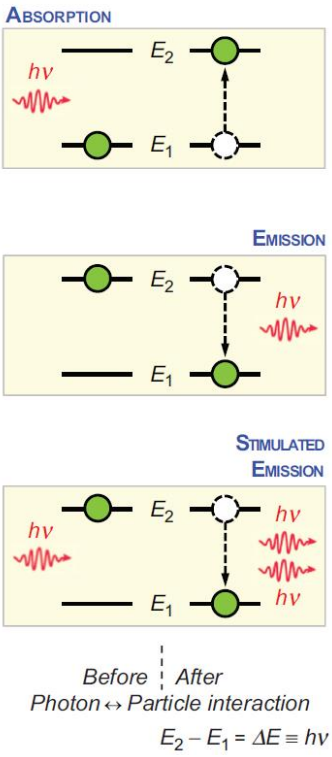

Figure 2. 1 Illustration of the three most important light–matter interactions [17].

2.2.1 Einstein Coefficients and Transition Probabilities

The absorption and emission of radiation is treated in a more quantitative manner following the steps of Einstein. We can consider an atom with only two stationary states denoted 1 and 2, while the three processes described in the previous section are represented by vertical up or down arrows, while the state energies are denoted by E_1 and E_2 (and the populations of atoms in each of the states are N_1 and N_2). The spectral energy density of a thermal radiation field was derived by Planck to be

$$\rho(v) = \frac{8\pi h v^3/c^3}{e^{hv/\kappa T} - 1} \tag{2.36}$$

where c is the speed of light and $\rho(v)$ is the spectral density of the radiation field and κ and T stand for Boltzmann's constant and the absolute temperature. The change in the population N_2 of state 2 can be due to the following three processes:

a) Induced absorption, given by the rate $\left(\frac{dN_2}{dt}\right) = N_1 B_{12} \rho(v)$

b) Induced emission, given by the rate $\left(\frac{dN_2}{dt}\right) = -N_2 B_{21} \rho(v)$

c) Spontaneous emission, given by the rate $\left(\frac{dN_2}{dt}\right) = -N_2 A_{12}$

In these rate equations, B_{21} is the Einstein coefficient for the induced $(2 \rightarrow 1)$ process and is equal to B_{12}, provided the statistical weights of states 1 and 2 are identical. Likewise, A_{21} is the Einstein coefficient for the spontaneous $(2 \rightarrow 1)$ emission process. When the populations have reached a steady state (equilibrium), one can write

$$\left(\frac{dN_2}{dt}\right) = 0 \equiv (N_1 - N_2) B_{21} \rho(v) - N_2 A_{21} \tag{2.37}$$

At thermal equilibrium, the populations are related to the Boltzmann distribution law according to

$$\left(\frac{N_2}{N_1}\right) = \left(\frac{g_2}{g_1}\right) \cdot e^{-(E_2-E_1)/kT} \equiv e^{-\Delta E/kT} \tag{2.38}$$

where it is assumed that the degeneracies are identical ($g_1 = g_2$). Introducing this $\frac{N_2}{N_1}$ ratio and the radiation density function $\rho(v)$ in the equilibrium condition, one can get

$$A_{21} = (\frac{8\pi h v^3}{c^3}) \cdot B_{21} \tag{2.39}$$

Thus, one can calculate A_{21} if $B_{21}$is known or vice versa by the equation. We can see that the spontaneous emission increases with the third power of the photon's frequency with respect to the induced emission (or absorption). The lifetime of the excited state is $\tau_{21} = 1/A_{21}$.

The transition moment is given by

$$\boldsymbol{\mu}_{21} = \int \Psi_2^* \boldsymbol{\mu} \Psi_1 dV \tag{2.40}$$

Where Ψ_1 and Ψ_1 are the wave functions of the two states, and $\boldsymbol{\mu}$ is the electric dipole moment operator with magnitude $\mu = \sum_j e\,|r_j|$, where e and r_j are the charge and position vector of the j$^{\text{th}}$ electron. The transition dipole moments are observable using a number of techniques listed in [18] including via experiments employing Autler-Townes splitting [20].

The strength of the absorption is proportional to the square of the transition dipole moment. The B_{21} coefficient is thus given by

$$B_{21} = (\frac{1}{6\varepsilon_0 \hbar^2}) \cdot |\boldsymbol{\mu}_{21}|^2 \tag{2.41}$$

where ε_0 is the vacuum permittivity. The transition probability $|\boldsymbol{\mu}_{21}|^2$ is related to the transition moment and underlines spectroscopic selection rules. If $\boldsymbol{\mu}_{21} \neq 0$, the transition is allowed; when $\boldsymbol{\mu}_{21} = 0$, the transition is forbidden.

2.2.2 The Absorption Coefficient and Cross Section

Absorption spectroscopy refers to the absorption of radiation by an atom or molecule when the absorbed photons have the energy needed to induce transitions from an initial to an excited state of the atomic or molecular system. The absorption spectrum is obtained by monitoring the absorbed intensity of the incident light after passing through the sample, as a function of its frequency or wavelength. If the transition involves the absorption of a single photon, the category of spectroscopy is called linear spectroscopy; otherwise, if several photons are absorbed, the category of spectroscopy is called nonlinear spectroscopy.

The basic equation for absorption spectroscopy is the Beer-Lambert law [20], which can be written as

$$I = I_0 \cdot \exp(-\alpha(v) \cdot l) = I_0 \cdot \exp(-\sigma(v) \cdot N \cdot l) \qquad (2.42)$$

Where I and I_0 stand for the transmitted and incident light intensities, l is the path length through the sample and $\alpha(v)$ is the so-called absorption coefficient, given by the product of $\sigma(v) \cdot N$, which includes the absorption cross section and the absorbing species concentration per unit volume. For a given transition between two energy levels, the frequency-dependent absorption cross section is given by

$$\sigma(v) = S_T g(v - v_0) \qquad (2.43)$$

Where S_T is defined as the transition intensity also known as the line strength and the function $g(v - v_0)$ describes the line shape, a function centred at v_0, which has the same analytical form for all unperturbed transitions (i.e., Lorentzian).

The observed width of a spectral line depends upon several factors like the spectral resolution of the measuring instruments, the lifetime of the excited state populated by the photon absorption, and/or the velocity distribution of the absorbing particles etc. The full width at half-maximum (FWHM) value, $\delta v_{1/2} = v_2 - v_1$, is used to characterize the spectral line profile. $I(v_2) = I(v_1) = 0.5 \times I(v_0)$ when $v_2 > v_0$ and $v_0 > v_1$.

2.2.3 Line Broadening

In general, the 'line broadening' factors are classified into two categories: homogeneous and inhomogeneous line broadening factors [17]. Homogeneous broadening refers to the case in which the contribution to the linewidth is the same for all atoms, while inhomogeneous broadening refers to the situation where that contribution is not the same for every atom or molecule.

Natural Broadening

Natural broadening is homogeneous broadening. The Heisenberg uncertainty principle can be written as $\delta E_e \cdot \tau_e \geq \hbar$, for an atom considered to have only two energy levels, the ground level E_g and an excited level E_e. In such a case the lifetime of the excited state is τ_e. If one assumes that the ground state lifetime is 'infinite' without external intervention, then its related energy uncertainty is 'zero'. Then this can be exploited to approximate the frequency uncertainty in a transition where the transition energy is $E_e - E_g = \triangle E_{eg} = hv_{eg}$ while the uncertainty is given by $\delta E_{eg} = \hbar/\tau \equiv h\delta v_{eg}$. δv_{eg} is known as the natural linewidth of the transition. The natural line width can be written as

$$\delta v_{eg} = (\frac{8\pi^2}{3\varepsilon_0 hc^3}) \cdot {v_{eg}}^3 \cdot |\mu_{eg}|^2 \tag{2.44}$$

Where μ_{eg} is the transition moment and ε_0 is the vacuum permittivity. The cubic dependence on transition frequency explains the different order of magnitude of the natural linewidth depending upon the particular spectral region under consideration. The line profile associated with natural broadening is given by the normalized Lorentzian line shape function

$$L(v - v_0) = \left(\frac{\delta v_n}{2\pi}\right) \cdot [(v - v_0)^2 + \left(\frac{\delta v_n}{2}\right)^2]^{-1} \tag{2.45}$$

with the Lorentz width at half maximum = $(2\pi \cdot \tau)^{-1}$, where τ is the intrinsic, natural lifetime of the upper energy level.

Doppler Broadening

Doppler broadening is an example of inhomogeneous broadening. Due to the Doppler effect, the observed frequency for the photon absorbed or emitted by an atom depends on the velocity of the absorbing/emitting atom or molecule relative to the detector. If the atom/molecule is moving toward or away from the detector with a speed v_z, the observed frequency of the transition is given by

$$v = v_0 \cdot (1 \pm \left(\frac{v_z}{c}\right)) \tag{2.46}$$

where v_0 is the intrinsic, quantum transition frequency and the sign + or – applies for the particle moving toward or away from the detector. The Doppler broadening parameter-based on the Maxwell velocity distribution can be written as

$$\delta v_D = (\frac{8RT \cdot ln2}{Mc^2})^{\frac{1}{2}} \cdot v_0 = 7.16 \times 10^{-7} \cdot (\frac{T}{M})^{1/2} \cdot v_0 \tag{2.47}$$

Here *R* is for the universal gas constant, *T* is the temperature (in Kelvin) and *M* is the particle (atom or molecule) mass (kg). The ensemble average over all atoms/molecules participating in this inhomogeneous broadening process gives rise to a Gaussian line shape function

$$G(v - v_0) = \left(\frac{(\pi ln2)^{\frac{1}{2}}}{\pi^2 \delta v_D}\right) \cdot \exp\left[-ln2(\frac{v - v_0}{\frac{\delta v_D}{2}})^2\right] \tag{2.48}$$

2.2.3 Laser Ionization Techniques

In laser ionization spectroscopy a single laser, tuned to a single wavelength, or two lasers, one to excite the atom or molecule to a well-defined electronic state and a second to ionize the system may be used [21]. In the case of the single laser the wavelength may or may not be in resonance with a bound electronic state of the system so that the multiphoton ionization process can be resonant [22] or non-resonant [23]. For two colour ionization, 1 + 1, 2 + 1 or other combinations of single and two (or multi) photon excitation and ionization may be employed [24].

Laser ionization spectroscopy is divided into two broad modalities, depending on whether the ions or the electrons are used for detection. The first of these, based on ion detection, is commonly known as resonance ionization spectroscopy (RIS) [25]. RIS is one of the many laser spectroscopy methods based on a resonant light-matter interaction [26]. It usually includes a multistep resonant excitation by photon absorption and the subsequent ionization of the excited atoms and molecules. Resonance ionization is highly selective because it allows only atoms of a given element to be ionized, since the intermediate excited states through which the process proceeds are unique to that element.

When electrons rather than ions are measured and analysed, this is normally done in the form of zero electron kinetic energy (ZEKE), i.e., the ionizing photon step is to energy levels (or the continuum) very close to the threshold, so that the photoelectrons have extremely low kinetic energy [27].

2.2.4 Stepwise Resonant Excitation

Resonance ionization involves stepwise excitation of an atomic or molecular system and subsequently ionizing it using laser light. In this approach, an atom in the ground state or a thermally populated metastable state is resonantly excited to a higher-lying excited state.

Fig. 2.2 describes the stepwise excitation of an atom from the initial state $|i>$ to the final state $|f>$ by the simultaneous absorption of photons. The photons may be emitted either by a single pulsed laser ($\omega_1 = \omega_2 = \omega_3$) or by two lasers (e.g., $\omega_1 \neq \omega_2 = \omega_3$) or occasionally, more sources [17]. In the non-resonant multiphoton experiments, the intermediate states are virtual.

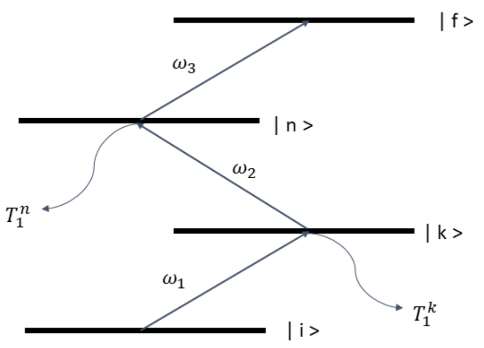

Figure 2. 2 Generic stepwise resonant excitation of an atom [28].

In order to reach the final state |f > via resonant laser excitation processes there are two conditions that must be met. The first one is that laser pulses have a duration τ such that:

$$\tau < T_1^j, \qquad (j = 1, \dots, f) \tag{2.49}$$

where T_1^j is the relaxation time of the intermediate excited levels.

The second condition is that the laser pulse fluence at frequency ω_j must exceed the saturation fluence of the corresponding transition.

$$\Phi(\omega_j) > \Phi_{sat}^j \tag{2.50}$$

The saturation fluence of the jth transition is in turn given by the inverse of its cross-section σ_j. Under very strong saturation of all the transitions, the probability of populating state |f > is maximum and the following relationship holds:

$$\frac{n_i}{g_i} = \cdots = \frac{n_k}{g_k} = \cdots = \frac{n_f}{g_f} \tag{2.51}$$

where n_k is the population density on the excited kth level and g_k is the corresponding state degeneracy. The population density of level |f > therefore is:

$$n_f = \frac{g_f}{\sum_k g_k} \tag{2.52}$$

which means that if one excites a sequence of states with increasing degeneracy the partial population of the final state is maximized.

2.2.5 Resonant Ionization

Upon resonant excitation of an atom, the excited electron may undergo several processes. After a certain time without further stimulus, it will spontaneously decay back to its ground state level or through another branch by emission of a photon. If other stimuli are present, it may be either ionized or excited to higher levels by a range of processes (Fig. 2.3).

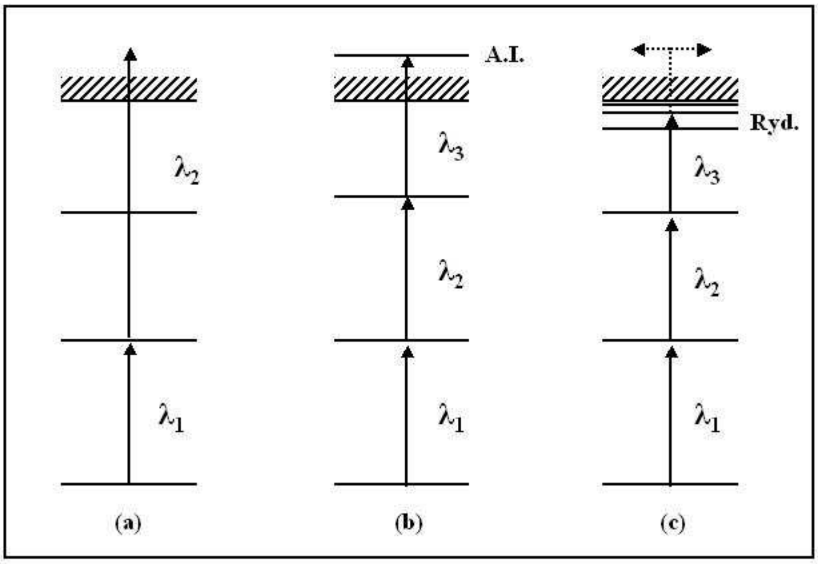

Figure 2. 3 Possible processes involved in the resonant ionization of an excited electron [29].

It may be ionized in a non-resonant way by a high-power laser (Fig. 2.3a). This process has a low efficiency as the cross section for absorption of a non-resonant photon is typically several orders of magnitude lower than that of a resonant one [30]. The ionization rate observed is directly proportional to the non-resonant laser photon flux [30]. However, it is not possible to saturate such a transition and since, at best, there is only one resonant step involved (the first one), this process has a low degree of selectivity.

Secondly, the electron may be further excited by a series of lasers to an auto-ionizing level at a higher energy (Fig. 2.3b). An auto-ionizing level is normally made up of multi electron excitations and such levels are extremely short lived since one of the electrons will couple to the continuum in a very short timescale whilst the other decays back to the (ionic) ground state. This property makes the resonance observed very broad as the lifetime and resonance width are connected by the

Heisenberg uncertainty principle. Resonance widths of several hundred GHz are not uncommon.

If, as in Fig. 2.3c, a second laser has promoted the electron to a high lying Rydberg level with an excitation energy close to the ionization potential of the atom, from this point there are two common methods of ionization. Firstly, a collision with another atom may provide enough energy for the electron to cross the ionization potential [22]. The probability of this process increases with pressure as the chance of a collision becomes more likely. Alternatively, the electron may be liberated via a high external electric field with a potential of the order of several kV.cm^{-1}, which is, depending on the principal quantum number, able to liberate the electron from the atomic potential [31].

2.3 Summary

The first part of this chapter provided an introduction to the structure of multi-electron atoms and described the angular momentum coupling and inner-shell excitation and the Auger process. The interaction of light with matter was introduced in the second part of this chapter, including Einstein coefficients, the absorption coefficient, line broadening, resonant ionization etc.

References

[1] B. H. Bransden and C. J. Joachain, Physics of atoms and molecules. 2nd Edition, Prentice Hall, Pearson (2003)

[2] E. A. Hylleraas, New calculation of the energy of helium in the ground state, as well as the deepest term of Ortho-Helium. *J. Phys.* **54**, 347 (1929)

[3] C. L. Pekeris, Ground state of two-electron atoms. *Phys. Rev.* **112**, 1649 (1958)

[4] Y. Accad, C. L. Pekeris, and B. Schiff, S and P states of the helium isoelectronic sequence up to Z=10. *Phys. Rev. A* **4**, 516 (1971)

[5] D. R. Hartree, The wave mechanics of an atom with a non-Coulomb central field. part III. term values and intensities in series in optical spectra. *Proc. Camb. Philos. Soc* **24**, 426 (1928)

[6] J. C. Slater, The theory of complex spectra. *Phys. Rev. A* **34**, 1293 (1929)

[7] W. Demtröder, Atoms, Molecules and Photons: An Introduction to Atomic-Molecular- and Quantum Physics. 2nd Edition, Springer, Heidelberg (2010)

[8] C. F. Fischer, Hartree-Fock method for atoms. A numerical approach. John Wiley and Sons, United States (1977)

[9] R. D. Cowan, The Theory of Atomic Structure and Spectra. University

of California Press (1981)

[10] P. Hohenberg and W. Kohn, Inhomogeneous electron gas. *Phys. Rev.* **136**, 864 (1964)

[11] W. Kohn and L. J. Sham, Self-Consistent equations including exchange and correlation effects. *Phys. Rev.* **140**, A1133 (1965)

[12] A. Zangwill and P. Soven, Density-functional approach to local-field effects in finite systems: Photoabsorption in the rare gases. *Phys. Rev. A* **21,** 1561 (1980)

[13] A. Zangwill and D. A. Liberman, A nonrelativistic program for optical response in atoms using a time dependent local density approximation. *Comput. Phys. Commun.* **32,** 63 (1984)

[14] D. A. Liberman and A. Zangwill, A relativistic program for optical response in atoms using a time dependent local density approximation. *Comput. Phys. Commun.* **32,** 75 (1984)

[15] W.R. Johnson, C. D. Lin, K. T. Cheng and C. M. Lee, Relativistic Random-Phase Approximation. *Phys. Scripta* **21,** 409 (1980)

[16] P. Auger, Sur les rayons β secondaires produits dans un gaz par des rayons X, *C. R. Acad. Sci.* **177** 169 (1923)

[17] H. H. Telle, Á. G. Ureña, Laser Spectroscopy and Laser Imaging: An Introduction. 1st Edition, CRC Press, Boca Raton (2018)

[18] G. Yuan, S. Jiang, Z. Wang, W. Hua, C. Yu, C. Jin and R. Lu, The role of transition dipole phase in atomic attosecond transient absorption from the multi-level model. *Struct. Dyn.* **6**, 054102 (2019)

[19] M. Piotrowicz, C. MacCormick, A. Kowalczyk, S. Bergamini, I. I. Beterov and E. A. Yakshina Measurement of the electric dipole moments for transitions to rubidium Rydberg states via Autler–Townes splitting. *New J. Phys.* **13**, 093012 (2011)

[20] A. Beer, Bestimmung der Absorption des rothen Lichts in farbigen Flüssigkeiten. *Ann. Phys.* **162**, 78 (1852)

[21] W. Demtröder, Laser Spectroscopy Vol. 1: Basic Principles, 4th edition, Springer (2008)

[22] G. Mainfray and C. Manus, Resonance effects in multiphoton ionization of atoms. *Appl. Opt.* **19**, 23 (1980)

[23] J. Morellec, D.Normand, G.Petite, Nonresonant Multiphoton Ionization of Atoms. *Adv. At. Mol. Opt. Phys.* **18**, 97 (1982)

[24] R. N. Compton and John C. Miller, Two-color multiphoton ionization of xenon. *J. Opt. Soc. Am. B* **2**, 2 (1985)

[25] G. S. Hurst, M. G. Payne, S. D. Kramer, J. P. Young, Resonance ionization spectroscopy and one-atom detection. *Rev. Mod. Phys.* **51** 767 (1979)

[26] K. N. Drabovich, Resonance interaction of short light pulses with matter, Sov. *Phys. Usp.* **11**, 4 (1968)

[27] K. Müller-Dethlefs, E. W. Schlag, High-resolution zero kinetic energy (ZEKE) photoelectron spectroscopy of molecular systems. *Annu. Rev. Phys. Chem* **42,** 109 (1991)

[28] M. Iannelli, Study on laser resonance photoionization of molybdenum atoms. Master Thesis, University of Pavia, 2017

[29] B. W. Tordoff, Development of resonance ionization techniques at the Jyväskylä IGISOL. PhD thesis, University of Manchester, 2007

[30] G. Mainfray, Atoms interacting with electromagnetic fields, multiphoton ionization. *J. Phys. Colloques* **43**, C2-367 (1982)

[31] S. H. Lin, Advances in Multi-photon Processes and Spectroscopy, Volume 4. World Scientific (1988)

Chapter 3 DLP Experimental Setup

In this chapter, the 1 m normal incidence VUV spectrometer system used for DLP photoabsorption studies is described. The operation of each component of this system and its contribution to the overall system are explained in detail.

3.1 Dual Laser Plasma Technique

The DLP technique is a highly useful experimental procedure, which is used to investigate VUV/XUV absorption spectroscopy in a wide range of atoms and ions [1]. It thus provides a flexible approach to the study of inner-shell and multiple electron excitations in atoms and ions. Solid targets are used and refractory elements can be explored by this experimental method.

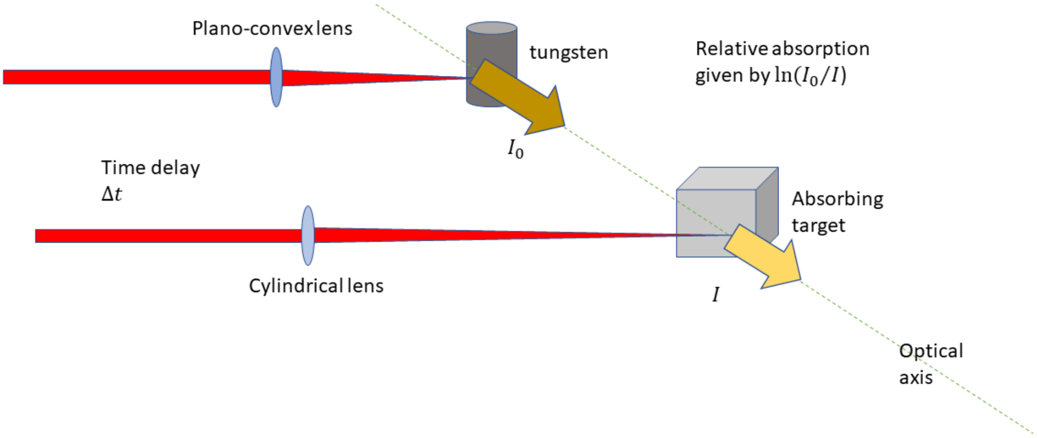

Figure 3. 1 Schematic diagram of the dual laser plasma experiment.

The typical layout of the DLP configuration is shown in Fig. 3.1. A Nd:YAG laser pulse is focused by a cylindrical lens onto the absorbing target to generate a line plasma. A second Nd:YAG laser pulse is focused onto a tungsten rod to produce the back-lighting continuum plasma at a defined time delay Δt after the first laser pulse. There are three critical parameters which dictate ion stage selectivity in any DLP photoabsorption experiment. (1) the laser conditions, (2) the time delay between the formation of absorbing and backlighting plasmas and (3) the displacement of the sample target surface with respect to the spectrometer optic axis. By changing the time delay between the two plasmas and the position of the absorbing plasma with respect to the optical axis, time and space resolved photoabsorption studies, of virtually any material, can be performed using this technique.

In the experiment, the background continuum intensity (I_0) is recorded by firing the back-lighting Nd:YAG laser alone. The transmitted intensity (I) can be obtained by firing both lasers, at a suitable time delay. The relationship between I_0 and I is described by the Beer-Lambert Law [2],

$$I = I_0 e^{(-\sigma n l)} \tag{3.1}$$

where σ is the absorption cross-section of the absorbing atomic/ionic species at a given photon energy, n (cm^{-3}) is the number density of absorbing atoms/ions in the light path and l (cm) is the length of the absorbing plasma. The product nl gives the integrated column density and its value must be ascertained in order to calculate an absolute value for the absorption cross-section. In the DLP technique the total relative photoabsorption cross-sections of numerous atomic/ionic species in ground and excited states that are populated within the plasma plume at any point in space and time are recorded. The relative total cross sections are obtained from the evaluation of the expression:

$$\sigma n l = ln(\frac{I_0}{I - I_f}) \tag{3.2}$$

Where I_f is the intensity of self-emission from the front (absorbing) plasma. I_f occurs in the early stage of the experiment and usually lasts less than 100 ns, so gating the detector to coincide with the continuum source reduces I_f (or after ~ 100ns eliminates it completely so that only *I* is recorded). The VUV/XUV self-emission from the absorbing plasma tends to be less of a problem compared to UV-Vis self-emission as the plasma temperature tends to be low (on the order one to a few eV). The quantity $ln(\frac{I_0}{I})$ yields the required absorption data. Signal averaging is employed to improve the signal-to-noise ratio for both $\mathrm{I_0}$ and I. The inter-plasma delay and laser pulse profiles are monitored by a fast photodiode on each shot to ensure reproducible conditions.

3.2 Overview of the Experimental Setup

A 1 meter normal incidence spectrometer system was developed at Dublin City University [3,4] for space and time resolved DLP photoabsorption and single plasma emission spectroscopy (Fig. 3.2 and Fig. 3.3).

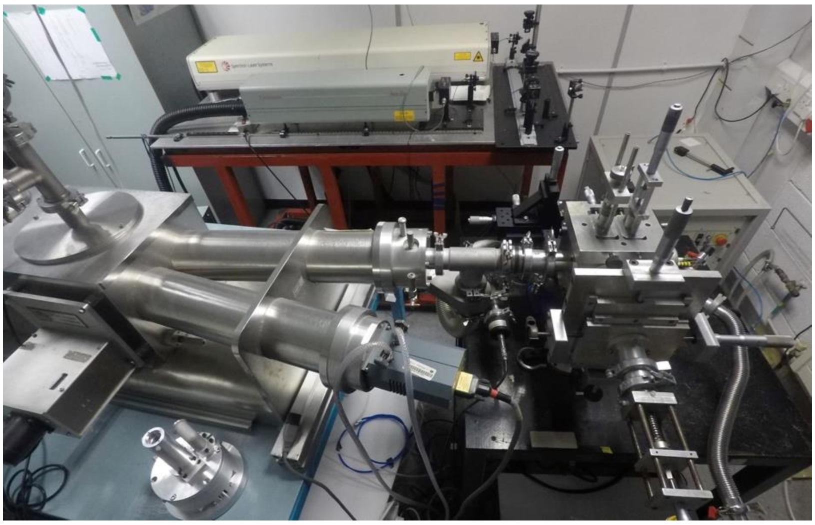

Figure 3. 2 The vacuum-UV DLP experiment at DCU (Top View).

As shown in Fig. 3.2, an Acton Research Corporation™ 1m normal incidence spectrometer, with fixed entrance and exit arms, sits at the center of the system. In the experiment the plasma radiation passes through the front fore-slit in the target chamber and subsequently is incident on the adjustable entrance slit which is fixed to the entrance arm of the 1 m normal incidence spectrometer. The radiation is dispersed with the aid of a 1200 grooves/mm Bausch & Lomb™ spherical concave holographic grating mounted within the spectrometer chamber which is operated in an off-Rowland circle type configuration [5]. In this configuration scanning of dispersed radiation across the detector plane is achieved through rotation of the grating, while focusing is maintained by linear translation of the grating. Either a Galileo™ Channel Electron Multiplier Array (CEMA) coupled to an EG&G™ linear Photo Diode Array (PDA) detector or a 2-D Andor™ back-thinned CCD (charge-coupled device) detector permit photoelectric recording of multichannel absorption and emission spectra. The latter was used exclusively in this study.

Light can be dispersed over the VUV spectral range from 30 to 325 nm with the aid of the 1200 grooves/mm spherical concave grating. The combination of the reflection efficiency of the grating and the limited spectral sensitivity of the CCD detector determines the overall system wavelength region that can be covered. The spectral region between 35 to 70 nm is largely free from second order light and the efficiency of the grating is low for wavelengths less than 35nm. The region is ideally suited to photoabsorption studies, where the first order absorption spectrum is not altered by the absorption signature of higher order light. The spherical concave diffraction grating, the entrance slit and the exit slit lie on a Rowland Circle whose diameter equals the radius of the curvature of the grating in the VM-521 spectrometer system.

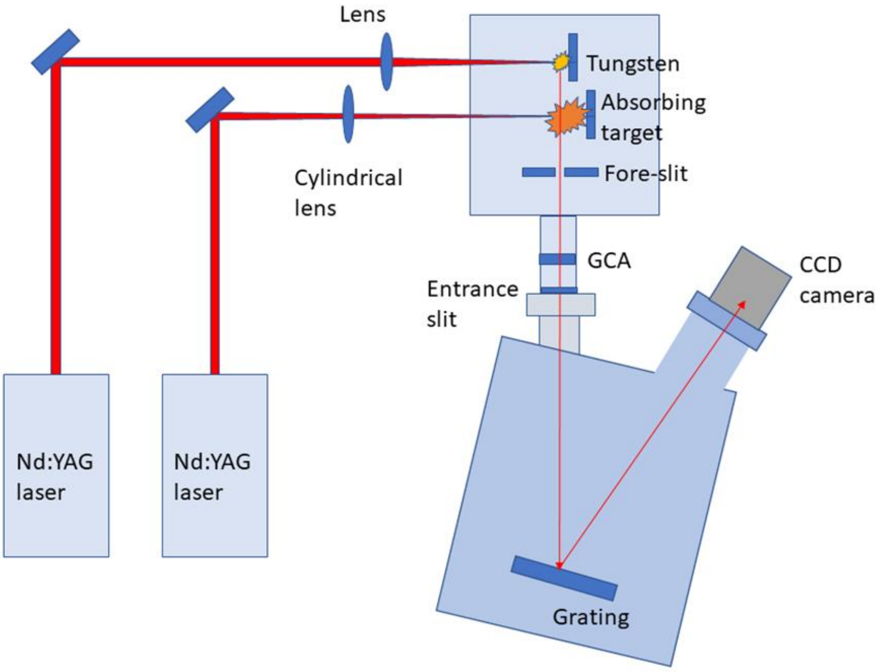

Figure 3. 3 Schematic diagram of the vacuum-UV DLP experiment at DCU.

3.3 The Concave Diffraction Grating

3.3.1 Bausch & Lomb^{TM} Diffraction Grating

The Bausch & Lomb^{TM} spherical concave diffraction grating, which is 96 mm wide and 56 mm high, is used in the spectrometer. Its iridium coated surface is holographically ruled at 1200 grooves/mm. The grating is held in a kinematic mount in the VM-521 spectrometer chamber, which can permit the removal of the grating and its subsequent return or replacement without the need for re-alignment. The radius of curvature of the spherical concave profile of the gratings front face is 995.4 mm (~1 m) and the rulings of the grating are blazed at an angle of 2.75°, which results in a maximum conversion efficiency of incident radiant flux to first order light at 80 nm [6].

3.3.2 The theory of concave gratings

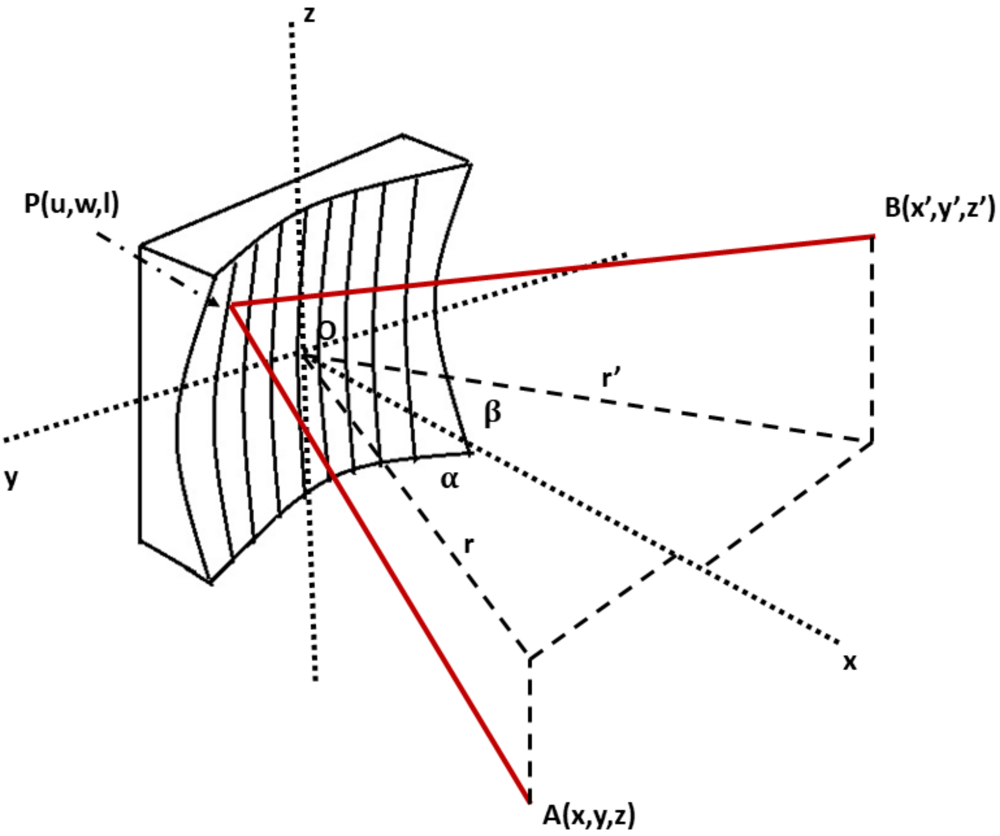

Figure 3. 4 Geometry and notation for grating theory [7].

Rowland [5] had developed the theory of the concave grating to a large degree. He showed that the rulings should be so spaced on the spherical surface as to be equidistant on the chord of a circular arc. Beutler [8] and Namioka [9,10] who used geometrical optics and Mack, Stehn, and Edlen [11], who used physical optics, contributed most for the developments of the concave grating theory in the following years.

As shown in Fig. 3.4., a Cartesian coordinate system is set up with the center of the grating rulings as the origin, x axis as the grating normal and z axis parallel to the rulings. A, B and P represent an object light source on the entrance slit, the corresponding image and a point on the grating, respectively. In order to make two rays reflected from adjacent grooves to reinforce at B, the path difference between these two rays must equal an integral number of wavelengths. The path difference is $m\lambda$, where the integer m is called the spectral order of the radiation. The path difference for two rays reflected from grooves a distance w apart is equal to $m\lambda w/d$, where d is the constant groove separation. All the rays at B from A through P must satisfy the Optical Path Function F

$$F = AP + BP + (\frac{wm\lambda}{d}) \tag{3.3}$$

where

$$(AP)^2 = (x-u)^2 + (y-w)^2 + (z-l)^2 \tag{3.4}$$

$$(BP)^2 = (x' - u)^2 + (y' - w)^2 + (z' - l)^2 \tag{3.5}$$

and u, w, l are the coordinates of point P.

The two equations (3.4 and 3.5) can be rewritten using cylindrical coordinates. So $x = rcos\alpha$, $y = rsin\alpha, x' = r'cos\beta$ and $y' = r'sin\beta$, where α and β are the angles of incidence and diffraction, respectively. Thus the path function F, $(AP)^2$ and $(BP)^2$ can be converted to cylindrical coordinates. According to Fermat's principle of least time, B is located in such a way that the path function F will be an extremum for any P. A and B are fixed while P can be any point on the surface of the grating. This leads us to the conditions that F to be extremum,

$$\frac{\partial F}{\partial l} = 0 \text{ and } \frac{\partial F}{\partial w} = 0 \tag{3.6}$$

In order to make B the point of perfect focus, these two equations must be satisfied simultaneously. However, a concave grating cannot obtain a perfect image, it will image a point source first into a vertical line and then a horizontal line. The following condition must be satisfied for B to be the best horizontal focal point.

$$\frac{cos^2\alpha}{r} - \frac{cos\alpha}{R} + \frac{cos^2\beta}{r'} - \frac{cos\beta}{R} = 0 \tag{3.7}$$

Where R is the radius of curvature of the grating. The solutions of this equation are

$$r = Rcos\alpha, r' = Rcos\beta \tag{3.8}$$

and

$$r = \infty, r' = \frac{Rcos^2\beta}{cos\alpha + cos\beta} \tag{3.9}$$

The first solution is known as the Rowland circle (condition). It shows that diffracted light of all wavelengths will be focused horizontally on the circumference of a circle of diameter R, which is equal to the radius of curvature of the grating. The entrance slit and grating must be located on the circle while the grating normal lies along a diameter. This is the normal condition for observing a well-focused spectrum. It is important that the spectrum be focused on the horizontal plane for vertical entrance slits and vertical rulings. The vertical focus is more important in the reduction or elimination of astigmatism. The locus of the vertical foci is given by

$$\frac{1}{r} - \frac{cos\alpha}{R} + \frac{1}{r'} - \frac{cos\beta}{R} = 0 \tag{3.10}$$

Two solutions of the equation are

$$r = R/cos\alpha, r' = R/cos\beta \tag{3.11}$$

and

$$r = \infty, r' = \frac{R}{cos\alpha + cos\beta} \tag{3.12}$$

The first solution (3.8) is the equation for a straight-line tangent to the Rowland circle at the normal to the grating. Thus, any point on the tangent will be focused vertically and brought to a horizontal astigmatic line on the same tangent. The two second solutions (3.9, 3.12) represent the case where the incident light is parallel. If the spectrum is viewed near the normal, then $cos\beta \sim 1$, both these equations become identical, and $r' = \frac{R}{cos\alpha + 1}$. Then the image will be stigmatic because the vertical and horizontal foci coincide in this condition, which is the situation which pertains for the Wadsworth mounting.

When the grating is illuminated close to normal, $r' = R/2$. Using Fermat's principle of least time again, it can be shown that for the central ray with path AOB,

$$\left(1+\frac{z^2}{r^2}\right)^{-\frac{1}{2}}(sin\alpha + sin\beta_0)=\frac{m\lambda}{d} \tag{3.13}$$

and

$$\frac{z}{r} = -\frac{z_0'}{r_0'} \tag{3.14}$$

The two equations represent the grating equation and the geometrical relation between object point and image point. We can obtain the same grating equation as for a plane grating by letting z tend to 0. Then ${z^2}/{r^2} \ll 1$ and can be neglected. Thus, the grating equation for a concave grating can be written as

$$\pm m\lambda = d(sin\alpha + sin\beta) \tag{3.15}$$

Where the negative sign applies when the spectrum lies between the central image $(\alpha = \beta)$ and the tangent to the grating (sometimes referred to as the 'outside order'). When the spectrum lies between the incident beam and the central image, the positive sign must be used, and the spectrum is referred to as the 'inside order'. The VM-521 spectrometer only records the spectrum on the inside order, so

$$m\lambda = d(sin\alpha - sin\beta) \tag{3.16}$$

since α and β lie on opposite sides of the grating normal and consequently have an opposite sign.

3.3.3 Dispersion

The primary purpose of a diffraction grating is to disperse light spatially by wavelength. A beam of white light incident on a grating will be separated into its component wavelengths upon diffraction from the grating, with each wavelength diffracted along a different direction. Dispersion is a measure of the separation (either angular or spatial) between diffracted light of different wavelengths. Angular dispersion expresses the spectral range per unit angle, and linear resolution expresses the spectral range per unit length.

Angular dispersion

The angular spread $\Delta\beta$ of a spectrum of order m between the wavelength λ and $\lambda + \Delta\lambda$ can be obtained by differentiating the grating equation, assuming the incidence angle α to be constant. The angular dispersion is defined as ${}^{d\beta}/_{d\lambda}$. By differentiating 3.15 we get

$$ {}^{d\beta}/_{d\lambda} = {}^{m}/_{dcos\beta} \qquad (3.17) $$

As the groove frequency ${}^{1}/_{d}$ increases, the angular dispersion increases. In other words, the angular separation between wavelengths increases for a given order m.

Linear dispersion

The dispersive power (in nm per mm) along the Rowland circle is called the plate factor and is the reciprocal of the linear dispersion ${}^{dl}/_{d\lambda}$. If we rewrite the plate factor in terms of $\Delta\beta$

$$ {}^{\Delta\lambda}/_{\Delta l} = {}^{\Delta\lambda}/_{\Delta\beta} \cdot {}^{\Delta\beta}/_{\Delta l} \qquad (3.18) $$

where $R\Delta\beta = \Delta l$, with R the radius of the concave grating. Therefore one can write that

$$ \frac{\Delta\lambda}{\Delta l} = \frac{1}{R({}^{\Delta\beta}/_{\Delta\lambda})} \qquad (3.19) $$

Replacing Δ in the limit by the differential d, the plate factor becomes

$$ {}^{d\lambda}/_{dl} = {}^{dcos\beta}/_{mR} = \frac{cos\beta}{mR(1/d)} \times 10^3 \ nm/mm. \qquad (3.20) $$

The latter holds when $(1/d)$ is the number of lines per mm and R is measured in meters. The smaller the numerical value of the plate factor, the larger the dispersion.

3.3.4 Off-Rowland Mount

The off-Rowland mounting system [6] for a concave grating operates by moving the grating on a fixed path through an angle θ to the grating normal. The angles of incidence and reflection are the same ($\theta = 0, \alpha = \beta$) without rotating the grating and the center of the Rowland circle remains on the bisector of the entrance arms. When the grating is rotated, a portion of the inside spectrum appears on the exit slit, the grating and the Rowland circle are correspondingly rotated through an angle θ and displaced by a distance x. As shown in Fig. 3.5, the entrance slit distance is increased by an amount s from the Rowland circle along the line joining the slit and the grating, and the exit slit distance is similarly decreased by an amount s'. We can see from the figure that the entrance slit lies a distance s outside the new Rowland circle, whereas the exit slit lies a distance s' inside the circle. We can thus write

$$R cos\alpha + s = R cos\beta - s' \tag{3.21}$$

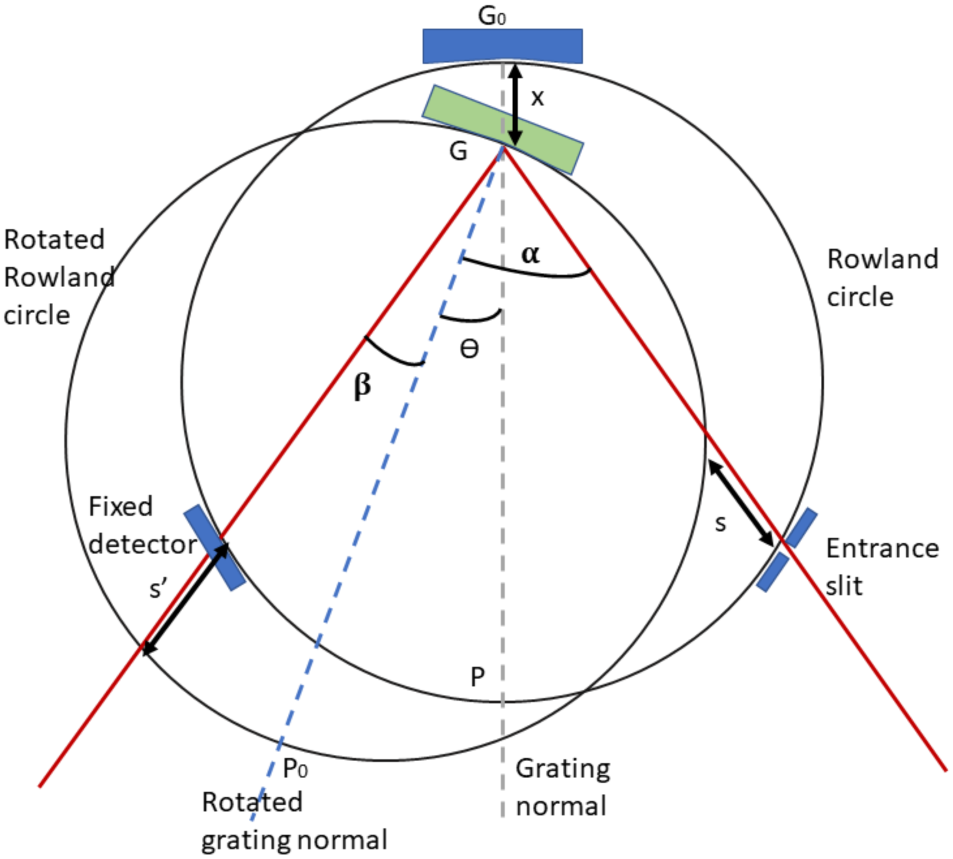

Figure 3. 5 Off-Rowland mount [4].

Let α_0 be the angle of incidence in the intial position of the grating. Then, if the change in the angle subtended by the slits at the grating is small over the spectral range scanned, i.e., for $s = s'$

$$s = Rsin\alpha_0 sin\theta \tag{3.22}$$

In order to find the linear motion x of the grating one can write that

$$s = Rcos(\alpha - \theta) - Rcos\alpha - xcos(\alpha - \theta) \tag{3.23}$$

and

$$s' = -Rcos(\alpha - \theta) + Rcos\beta + xcos(\alpha - \theta) \tag{3.24}$$

Where $R = G_0P_0 = GP$ and $R - x = GP_0$. If $s = s'$, $\theta = \frac{1}{2}(\alpha + \beta)$. We can obtain

$$x = R(1 - cos\theta) \tag{3.25}$$

The grating in the current experiment will rotate from 0° to 20° in order to scan the spectral range of 30 to 325 nm. The total linear translation of the grating along the grating normal will be from 0 to 20 mm. The spectrometer is blazed for radiation of wavelength 80nm in the first order.

3.3.5 Resolving Power

The resolving power P of a grating is a measure of its ability to separate adjacent spectral lines of average wavelength λ. It is commonly expressed as the dimensionless quantity.

$$P = \frac{\lambda}{\Delta\lambda} \tag{3.26}$$

We know that

$$\Delta\lambda = \frac{\lambda}{mN} \tag{3.27}$$

Thus, the resolving power

$$P = \frac{\lambda}{\Delta\lambda} = mN \tag{3.28}$$

Where m is the diffraction order number and N is the total number of grooves illuminated on the surface of the grating. The reciprocal linear dispersion of the grating describes the separation between two adjacent wavelengths

$$\frac{d\lambda}{dl} = \frac{d cos\left(\frac{D_v}{2}\right) cos\theta}{mR} \tag{3.29}$$

where d is the inter groove separation (8.33×10^{-7}m), ι is the distance along the Rowland circle, D_v is the angle of deviation which is the angular separation between the entrance and exit slits (15° for our spectrometer), θ is the angle of rotation of the grating, m is the spectral order and R is the radius of curvature of the grating. The reciprocal linear dispersion (plate factor) varies from 0.830nm/mm at 20nm to 0.816nm/mm at 300nm for the spectrometer. The value of θ can be calculated using the grating equation for a given wavelength. The corresponding image on the focal curve of a concave grating in a Rowland mount has a width corresponding to a wavelength interval $\Delta\lambda$ for an entrance slit of width W_s. Namioka [9] has defined $\Delta\lambda$ as

$$\Delta\lambda = \frac{W_s d}{R} \tag{3.30}$$

Where W_s is the entrance slit width. For the VM-521 spectrometer operated with an entrance slit width of 50μm, the corresponding equivalent spectral width is 0.042nm.

3.4 Nanosecond Laser Systems

3.4.1 Spectron Laser System

The background continuum plasma was formed by a Q-switched Nd:YAG laser system operated at a fundamental wavelength of 1064 nm. The laser system, manufactured by Spectron Laser Systems, is composed of a control unit and a laser head connected by a flexible umbilical. The laser head comprises the laser oscillator and all other optical components. These components are mounted on a series of invar bars which give the laser superb mechanical and thermal stability in its operation. The control unit is a free-standing cabinet which contains all the controls, power supplies, cooling systems and other accessories necessary to run the system.

A schematic diagram of this laser head is shown in Fig. 3.6. The laser cavity is defined by the 100% reflecting rear coupler (mirror) and the partially transmitting front coupler. The active lasing medium is a 103 mm long, 6.3 mm diameter crystalline yttrium aluminium garnet ($Y_2Al_{12}O_{12}$) rod doped with neodymium ions (Nd^{3+}). Population inversion in the lasing medium is achieved when sufficient light emitted during a ~200 µs flashlamp pump cycle has been absorbed by the Nd:YAG rod. The linear flashlamp and the Nd:YAG rod are sealed in the oscillator chamber. Positioned between the lamp and the rod is a special glass filter plate which absorbs the UV radiation from the lamp and therefore protects the rod from permanent damage. The intra cavity telescope is used to obtain a low beam divergence from the oscillator by discriminating against high order modes within the cavity. It also compensates for the thermal lensing of the rod and the hence collimation settings of the telescope must not be altered from optimal values. The final beam divergence, following traversal through all optical components within the laser head, lies in the region of 0.8 to 2 mrad. The inter-lens distance in the telescope is adjusted according to the laser repetition rate required in order to achieve optimum beam divergence.

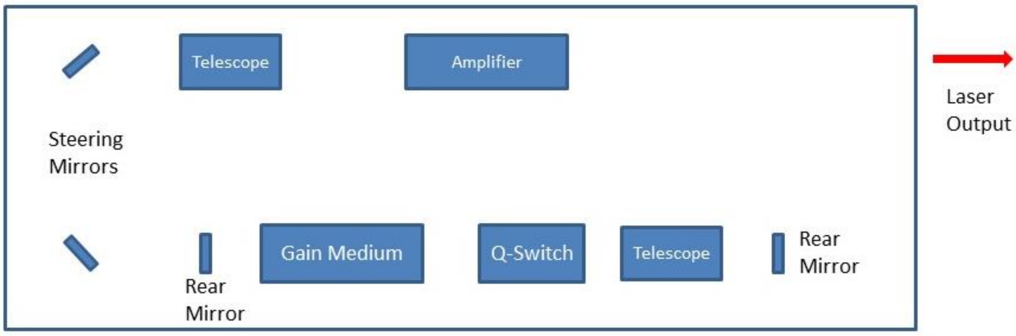

Figure 3. 6 The optical layout of the Spectron laser system [12].

The optical components of the Q-switch unit are a polariser plate (for horizontal polarisation) a temperature stabilised Pockels cell crystal and a beam path correcting prism. The Q-switch is used to release the energy stored in the laser rod in a short, very intense pulse. When the flashlamp is triggered a voltage is applied across the Pockels cell crystal. This induces birefringence in the crystal and makes it act as a quarter wave plate. The induced axes are at 45^o to the plane of polarisation of light passed by the polariser. This horizontally polarised light is resolved into two mutually perpendicular components one of which is shifted 90^o out of phase to the other upon traversal of the Pockels cell crystal to which a ¼ wave voltage has been applied. The linear horizontal polarised light is converted in circular polarization after the first passage in the Pockels cell. After reflection from the rear mirror, the light passes through the crystal for a second time and a further 90^o phase shift occurs. The circular polarization is converted to linear vertical polarization. The returning light is then vertically polarised and is rejected by the polariser. There is therefore no light feedback and hence no laser oscillation.

When the stored energy in the laser rod reaches a maximum the ¼ wave voltage is removed and there is no polarisation change and feedback occurs. A second telescope located before the flashlamp-pumped amplifier expands the beam before it traversed the Nd:YAG amplifier crystal. The final output pulse at 1064 nm has a Gaussian intensity profile, a full width at half maximum (FWHM) of 15-20 ns and a pulse energy in the region of 200 to 400 mJ. The maximum repetition rate is 10 Hz.

3.4.2 Surelite Laser System

The absorbing plasma was generated by a Continuum Surelite Q-switched laser system. The fundamental wavelength of this Surelite III-10 laser is 1064 nm and the laser pulse carries an energy of up to 800 mJ with a FWHM of 6 ns. The repetition rate of this laser is 10 Hz. The output pulse energy is varied in 5%, which makes this laser ideal for laser plasma experiments where repeatable results are highly desirable. Fig. 3.7 shows the layout of the Surelite III-10 laser.

The head is a modular design incorporating the Nd^{3+} doped YAG rod and linear flashlamps for optical pumping. The Nd^{3+} doping levels vary from 0.9 to 1.4%. The Nd:YAG rod ends have hard dielectric anti-reflection coatings and the rod length is 115 mm, measured along the optical axis. The linear flashlamps, filled with xenon with a pressure of 1-3 atmospheres, are in a close coupled configuration surrounded by a high brilliance magnesium oxide diffuser, resulting in a high pumping efficiency that minimizes thermal loading and reduces power consumption. The discharge system of the flashlamp uses a negative, critically damped pulse (-1.8kV max) with a duration of 200 µs full width half max (FWHM). All these features, taken together, can create the excellent pumping homogeneity required for producing high gain and superior quality beams. The flashlamps and laser rods are cooled with an onboard reservoir of distilled, deionized water.

In the Spectron laser described above the Q-switch is a combination of a polarizer and a Pockels cell. For the Surelite laser, the Q-switch is comprised of three components, namely a Pockels cell, a linear polarizer and a $\frac{\lambda}{4}$ plate. As before the Q-switch prevents lasing in the resonator until the laser gain reaches its peak and then opens the cavity to allow oscillation. The flashlamp discharge produces an intense, broadband light pulse that is absorbed by the Nd:YAG rod so that population inversion is achieved.

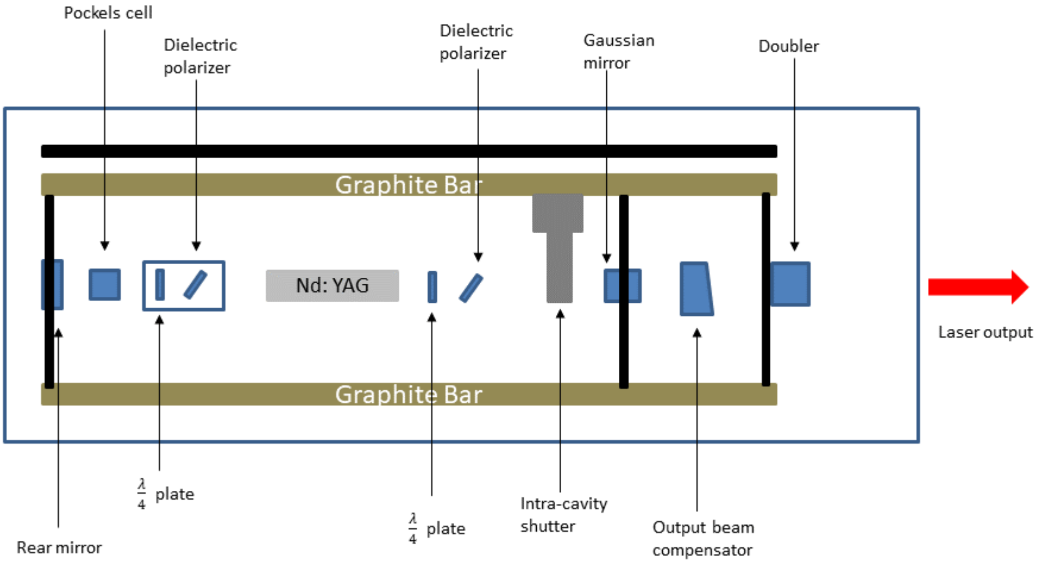

Figure 3. 7 The internal configuration of the continuum Surelite III-10 laser [13].

The light emerges from the rod unpolarised, until it reaches the dielectric polariser which is set at an angle of 57° to the optical axis of the laser. At this angle, known as Brewster's angle, 'p' polarized light is perfectly transmitted through the dielectric surface. The dielectric polarizer passes the plane polarised light to a λ/4 plate which circularly polarises the radiation. The light propagating within the oscillator cavity makes a double pass through the Pockels cell and $\frac{\lambda}{4}$ plate. With zero volts applied to the Pockels cell, it adds no rotation while a double pass through the $\frac{\lambda}{4}$ plate rotates the plane of polarisation by 90°. Hence light cannot propagate up and down the cavity (opposite to the case of the Spectron laser where the $\frac{\lambda}{4}$ voltage is applied to achieve this condition). At peak population inversion, typically 160 μs after the flashlamp trigger, the $\frac{\lambda}{4}$ voltage is applied, the Q of the cavity is restored and the Surelite laser produces a giant pulse of some hundreds of mJ with a width of a few nanoseconds.

The Surelite laser system can generate laser light at the Nd:YAG fundamental wavelength (1064 nm) or its second, third or fourth harmonic (532, 355, 266 nm). This is achieved by passing the fundamental beam through a second, a second plus third, or a second and fourth harmonic generator.

3.5 Target Chamber

As shown in Fig. 3.8, the target chamber is a 127 mm aluminium cube with 70 mm diameter holes drilled into each of its six faces. There are three vacuum compatible X-Y-Z stages mounted on the target chamber.

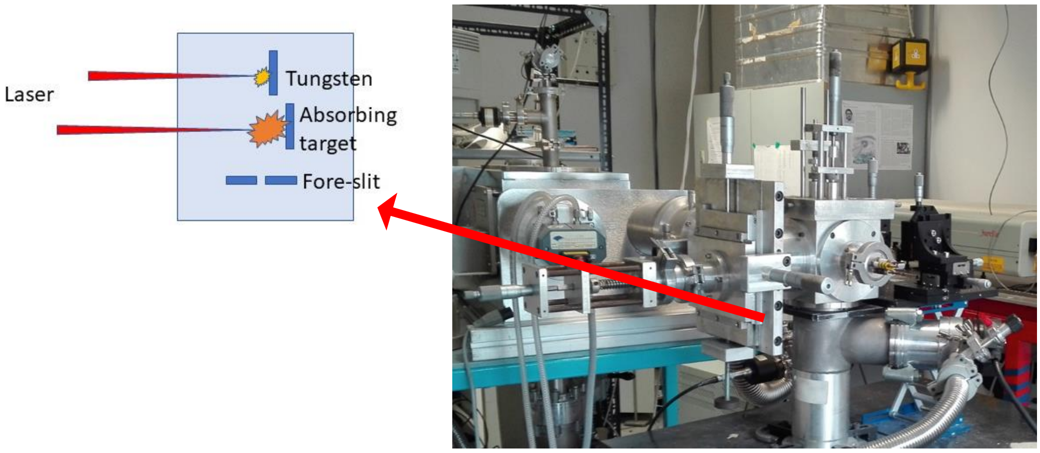

Figure 3. 8 The target chamber on the vacuum-UV DLP system.

Two of them are located on the top flange and the remaining one is mounted on the backside of the target chamber. The top mounted stage, closest to the entrance slit of the spectrometer, holds the pre-slit. The other top mounted X-Y-Z stage holds the tungsten target used to generate the VUV backlighting plasma. The third holder on the back side of the target chamber is used to hold the absorbing target material between the pre-slit and the tungsten target. There is a glass capillary array (GCA) between the target chamber and the spectrometer. The GCA is 25 mm in diameter, 3 mm thick and has a pore diameter of 50 µm. It is used to allow a pressure differences to exist between two separate parts of a vacuum system while leaving the aperture between these two areas mostly transparent to VUV and XUV radiation.

Outside the target chamber, a spherical lens of 10 cm focal length and a 10 cm focal length cylindrical lens are used to form the backlighting plasma and the absorbing plasma, respectively. A long and cooler column of absorbing species can be obtained using the cylindrical lens, which is useful for maximising neutral or low ion stage yields. With the cylindrical lens one can translate a knife edge across the beam in order to vary the length of the plasma column. The spherical lens gives rise to a higher irradiance on target and hence a hotter plasma with higher ion stages, which will emit radiation in the vacuum-UV as required for the backlighting source.

3.6 Pre-slit

Adding a pre-slit inside the target chamber is an important feature of the experiment. The pre-slit can shield any radiation coming from the absorbing target surface from the detector. Different spatial regions of the absorbing plasma can be investigated by changing the relative position between the absorbing plasma and the pre-slit. The adjustable pre-slit is fixed on the optical axis and set at a width of 50 µm, approximately 30mm away from the absorbing plasma source.

3.6 Andor CCD Camera

A back-thinned Andor Technology CCD camera is attached to the exit arm of the ARC VM521 1m spectrometer. The CCD camera consists of a two-dimensional array, 1024 pixels high × 1024 pixels wide, with a pixel size of 24 × 24 µm corresponding to an active imaging area of 24.6 × 24.6 mm^2. The centre of the CCD camera is mounted tangentially to the Rowland circle of the spectrometer.

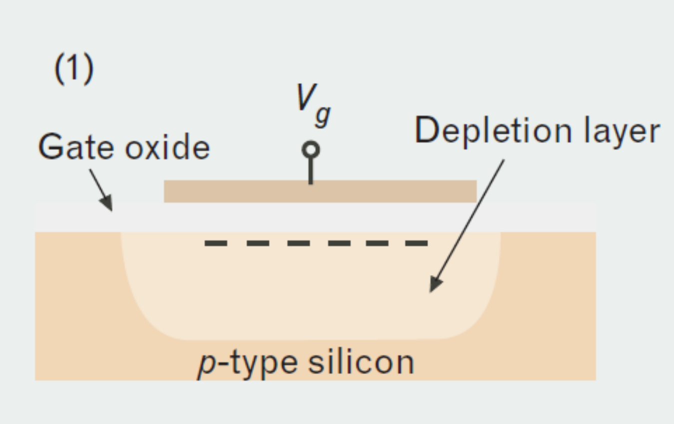

Figure 3. 9 Cross section of a metal-oxide semiconductor (MOS) capacitor consisting of a biased gate electrode, an oxide layer, and a p-type silicon substrate. With the gate biased positive, a packet of electrons can be collected and held at the silicon/oxide interface [14].

CCD cameras are based on metal oxide semiconductor (MOS) technology. The MOS capacitor is the fundamental element of a CCD, and it includes a semiconductor (silicon) substrate, an overlying oxide or other dielectric film, and a conductive gate. The oxide is usually SiO_2. When a MOS capacitor is made on p-type material and the gate is biased positive, the holes are repelled from the gate area by the resulting fields. A zone depleted of holes (termed a depletion layer) is created while the bias creates conditions favourable for the accumulation of electrons at silicon surface. Photons can only be converted into electronic charges in the depletion region. And then they are held by the electric fields which form the pixel. The charge held in the depletion layer is then transferred and measured. In order to readout the sensor, one uses the progressive Scan readout method [15]. The accumulated charge is shifted vertically row by row into the serial output register and for each row the readout register must be shifted horizontally to readout each individual pixel.

The CCD camera was used in 'full vertical binning' mode in the current experiment. Binning allows combining the charges from several pixels of one column. It can increase the readout speeds and improve the signal to noise ratio albeit at the expense of reduced spatial resolution. The full vertical binning means combining the charges from the entire vertical column of pixels.

3.7 Summary

In this chapter, details of the DLP system currently in operation at DCU has been introduced, and the essential components (Nd:YAG nanosecond laser systems, target chamber, Acton Research Corporation™ (ARC) 1 m normal incidence spectrometer and Bausch & Lomb™ diffraction grating) of this system have been described. All the data presented in chapter 5 was taken by this system.

References

[1] E. T. Kennedy, J. T. Costello, J.-P. Mosnier, P. van Kampen, VUV/EUV ionizing radiation and atoms and ions; dual laser plasma investigations. *Rad. Phys. Chem*. **70**, 291 (2004)

[2] A. Beer, Bestimmung der Absorption des rothen Lichts in farbigen Flüssigkeiten. *Ann. Phys.* **162**, 78 (1852)

[3] E. P. O'Leary, VUV Laser-Induced Plasma Spectroscopy for Low Level Sulphur Detection in Steel. PhD thesis, Dublin City University, 2007

[4] X. Jiang, Dual-Pulse Laser Induced Breakdown Spectroscopy in the Vacuum Ultraviolet with Ambient Gas: Spectroscopic Analysis and Optimization of Limit of Detection of Carbon and Sulfur in Steel. PhD thesis, Dublin City University, 2013

[5] H. A. Rowland, XXIX. On concave gratings for optical purposes. *Phil. Mag.* **16**, 197 (1883)

[6] O. E. Meighan, XUV and VUV Photoabsorption and Emission Studies in Thorium and other High-Z Laser Plasmas. PhD thesis, Dublin City University, 2000

[7] J. A. R. Samson, Techniques of Vacuum Ultraviolet Spectroscopy. Pied Publications, Lincoln, Nebraska (1967)

[8] H. G. Beutler, The Theory of the Concave Grating. *J. Opt. Soc. Am.* **35**, 311 (1945)

[9] T. Namioka, Theory of the Concave Grating. I. *J. Opt. Soc. Am.* **49**, 446 (1959)

[10] T. Namioka. Theory of the ellipsoidal concave grating. *J. Opt. Soc. Am.* **51**, 4 (1961)

[11] J. E. Mack, J. R. Stehn, and B. Edlen, *J. Opt. Soc. Am.* **22**, 245 (1932)

[12] Spectron SL800 series laser system operator manual

[13] Surelite III-10 laser system operator manual

[14] B. E. Burke, J. A. Gregory, M. Cooper, A. H. Loomis, D. J. Young, T. A. Lind, P. Doherty, P. Daniels, D. J. Landers, J. Ciampi, K. F. Johnson, and P. W. O'Brien, CCD Imager Development for Astronomy. *Linc. Lab. J.* **16**, 393 (2007)

[15] C. A. Poynton, Digital Video and Hdtv: Algorithms and Interfaces. Morgan Kaufmann (2013)

Chapter 4 Resonant Laser Ionization Experimental Setup

4.1 Background to the Experiment – The SPES Project

The experiment on laser resonance photoionization of molybdenum atoms has been carried out at Legnaro National Laboratories (LNL), which is one of the four national labs of the Italian Institute of Nuclear Physics (INFN). The mission of INFN-LNL is to perform basic research in nuclear physics and nuclear-astrophysics, together with applications of nuclear technologies.

The work reported in this thesis is a part of the SPES project [1]. SPES is the acronym for "Selective Production of Exotic Species". It represents an intermediate step toward the future generation European ISOL (Isotope Separation On-Line) facility (EURISOL) [2]. The aim of the SPES project is to provide high intensity and high-quality beams of neutron-rich nuclei to perform forefront research on nuclear structure, reaction dynamics and interdisciplinary fields like medical, biological and material sciences. SPES is a second generation ISOL (Isotope Separation On-Line) radioactive ion beam facility for the production of exotic Radioactive Ions Beams (RIBs). The SPES facility (Fig. 4.1) concentrates mainly on the production of neutron-rich radioactive nuclei having masses in the range 80-160 based on the ISOL technique. There are four phases [3] for the SPES project:

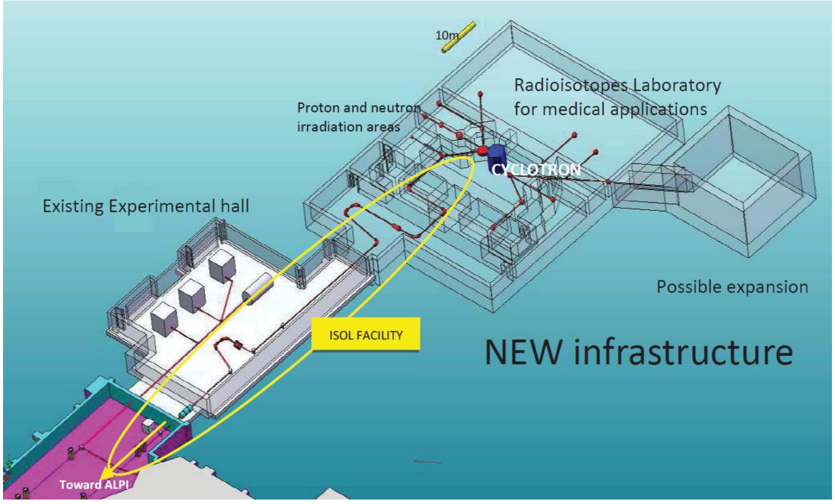

Figure 4. 1 Simplified layout of the SPES facility [1].

- **SPES-alpha**: This part of the project includes the acquisition, installation and commissioning of a high-performance cyclotron with high output current (~0.7 mA) and high energy (up to 70 MeV), together with the related infrastructure for the cyclotron and experimental stations.

Figure 4. 2 SPES commercial cyclotron during installation inside the future SPES building, which is shown on the right [3].

The commercial cyclotron in Fig. 4.2 has already been installed and is currently being tested. It has two exit ports, which will be used for basic research and technological applications. One of the two beams will be used to produce neutron-rich ions by collisions of protons onto a UCx (Uranium Carbide) target for nuclear physics; the second beam will be dedicated to applied physics.

- **SPES-beta** is about the acceleration of neutron-rich unstable nuclei. Neutron-rich species will be accelerated and collided against suitable targets to produce new, extremely neutron-rich nuclei, which are similar to those generated in stellar stages and are not present on Earth due to their short lifetime. The study of the neutron-rich nuclei produced by such systems can extend our knowledge of nuclei at extreme conditions and give basic information for the study of stellar evolution.
- **SPES-gamma** concerns the production of radionuclides of medical interest by using the SPES-alpha cyclotron. The goal is the production of innovative radiopharmaceutical (e.g. those based on Sr-82/Rb-82 and Ga-68/Ge-68) as well as the production of conventional radionuclides with new

accelerator-based approaches. The metastable state of Technetium-99 (Tc99-m) is of particular interest in this stage.

- **SPES-delta** foresees the development of a high intensity linear accelerator based on radio-frequency quadrupole (RFQ) technology. Following such a route beam currents as high as 30 mA at a fixed 5 MeV energy may be achieved. This accelerator can yield an extremely intense neutron source which may have several applications such as nuclear astrophysics, characterization of nuclear waste, or in experimental cancerous tumour treatment by means of Boron Neutron Capture Therapy (BNCT) [4].

4.2 SPES for Nuclear Medicine: MOLAS Project

^{99m}Tc is the most commonly used medical radioisotope for medical diagnostic procedures [5]. It readily emits gamma rays with a photon energy of 140keV which can be detected in human bodies by gamma cameras. Technetium-99m's half-life for gamma emission is 6 hours, which will allow the scanning procedures rapidly as to keep the total radiation exposure of the patient low.

^{99m}Tc was discovered as a product of deuteron bombardment of molybdenum at a cyclotron. At present, ^{99}Mo, whose half-life is 66 hours [6], is used to create ^{99m}Tc commercially. The process is based on spontaneous β-decay of ^{99}Mo, which occurs with 87% efficiency and decay energy 1.357 MeV:

$$^{99}\mathrm{Mo} \xrightarrow{\beta\ decay} {}^{99m}\mathrm{Tc}$$

^{99}Mo is mainly extracted from fissile products obtained by highly enriched uranium (U-235) atoms [7] or by neutron activation of natural Mo or ^{98}Mo. Both processes however require nuclear reactors, whose availability may be problematic.

New techniques, to produce ^{99}Mo rely on neutron activation of ^{98}Mo or exploit proton irradiation of ^{100}Mo using accelerators, have been investigated. A new project, MOLAS (MOlybdenum production with LASer techniques) at SPES has been introduced recently. The work on Mo reported in this thesis is directly related to this project. It belongs to a broad class of atomic vapour laser isotope separation (or AVLIS) schemes [8] in which selective laser ionization of the isotope of interest is the separation modality.

The objective of MOLAS is to produce the ^{99}Mo isotope using a commercial cyclotron with energy in the range of 10 MeV to 20 MeV. The target is a UCx (Uranium Carbide) SPES-like target [9] with Molybdenum disks or a multi Mo foil structure in place of the UCx. The target could be either a natural Molybdenum disk or an enriched target of ^{100}Mo. The former would reduce the target cost at the expense of the production rate while the latter would ensure a higher production rate, but at a much higher cost.

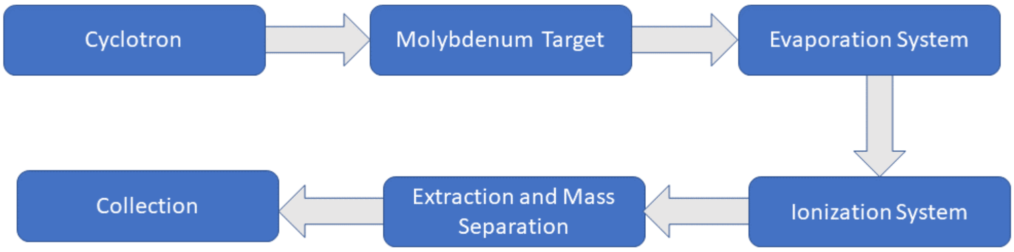

Figure 4. 3 The ^{99}Mo production line design for MOLAS [10].

In the experiment, the Molybdenum target is activated by the highly energetic protons coming from the cyclotron. Once activated, the target undergoes a laser ablation process and the evaporated atoms are then made available for a subsequent resonant laser ionization step (Fig. 4.3). ^{99}Mo ions are selected by a mass spectrometer and then collected for use.

An off-line laser laboratory experiment was built in 2013 to test the laser ablation, laser photoionization and mass separation process chain. Three dye lasers, hollow cathode lamps and a home-made time of flight mass spectrometer (ToF-MS) are located in this lab. The following sections give some details of these component parts of the experimental setup. This was the setup used to obtain the results shown in chapter 6 of this thesis.

4.3 Molybdenum – Photo Excitation Scheme

The two colour, laser resonance ionization experiment on molybdenum atoms was performed in the off-line laser laboratory at LNL. This experiment was based on a two-colour ionization scheme with two resonant excitations plus one non-resonant transition to the continuum. The scheme is shown in Fig. 4.4, where the energies of the levels involved are given in cm^{-1} [10].

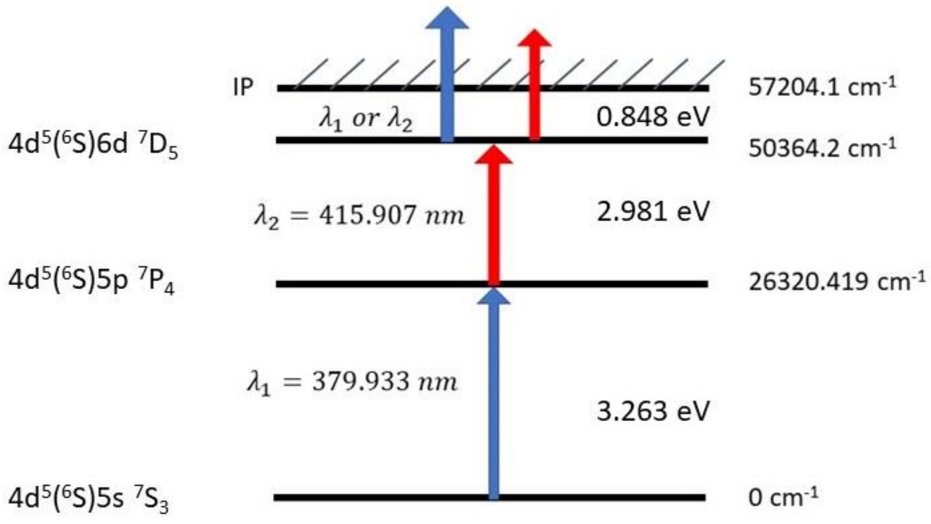

Figure 4. 4 The scheme for the two-colour laser resonance ionization (LRI) of molybdenum atoms [10].

The transition from the ground (4d^5(^{6}S)5s ^{7}S$_3$) state to the chosen excited (4d^5(^{6}S)5p ^{7}P$_4$) state requires a photon energy of ca. 3.263 eV (26320.419 cm^{-1}), corresponding to a laser wavelength λ_1 = 379.933 nm. The second step photon energy is ca. 2.981 eV (24043.824 cm^{-1}) corresponding to a laser wavelength λ_2 = 415.907 nm and leaves the Mo atom in the 4d^5(^{6}S)6d ^{7}D$_5$ state. Both wavelengths given are in vacuo values. The molybdenum atoms in the 4d^5(^{6}S)6d ^{7}D$_5$ state can then be ionized by either of the lasers operating at λ_1 or λ_2.

4.4 Experimental Set-up

The experiment is based on the three-photon excitation scheme outlined in Fig. 4.4, using two dye laser beams [11,12]. The transition from the ground state to the first excited configuration is in the UV range (ca. 379.933 nm). The TDL50 dye laser was pumped by a frequency doubled Nd:YAG laser (Quantel YG580 series) operating at 532 nm. The output of the TDL50 dye laser was frequency doubled in turn to produce the UV output with a central wavelength of 379.933 nm. The final output power was typically 0.3 mW, corresponding to 30 µJ per pulse, for a pump power of 1.5 W. The second wavelength (415.907 nm) was provided by a Lamda Physik FL2002 Dye laser also pumped by a frequency doubled Nd:YAG laser (Quantel YG980 series) operating at 532 nm. The final output power was typically 1.6 mW, corresponding to 160 µJ per pulse, for a pump power of 1.5W.

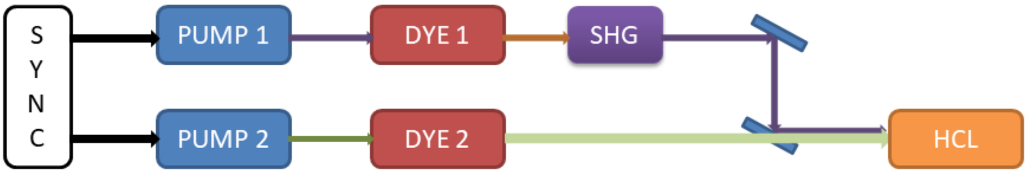

Figure 4. 5 Schematic of the optogalvanic experimental set-up [11].

The first wavelength (379.933 nm) was generated in the TDL50 dye laser by sum frequency generation (SFG) in a Potassium Dihydrogen Phosphate (KDP) crystal. SFG is a three-wave mixing process where two waves at λ_1 and λ_2 add to give rise to a wave at λ_3 in such a way that

$$\frac{1}{\lambda_1} + \frac{1}{\lambda_2} = \frac{1}{\lambda_3} \qquad (4.1)$$

Here λ_1 is the infrared fundamental wavelength of the Nd: YAG pump laser (1064 nm), λ_3 is the desired wavelength (379.933 nm). λ_2 is the output wavelength from TDL 50 dye laser (590.949 nm). The dye laser wavelength λ_2 = 590.949 nm was obtained by optically pumping the dye (Rhodamine 610 Perchlorate and Methyl Alcohol) with the second harmonic output (532 nm) of the Nd:YAG pump laser (Quantel® YG580 series). The second wavelength (λ = 415.907 nm) from FL 2002 dye laser was directly obtained by pumping the dye with the third harmonic output (355 nm) of the corresponding Nd:YAG pump laser (Quantel YG980 series). Stilbene 420 and Methanol were used to prepare the dye.

The two laser beams were focused inside a Hollow Cathode Lamp (HCL) with the final overlapping volume amounting to less than 1 mm^3. The HCL is powered by a KEPCO BHK 1000-40MG supply operated at a controlled current level of 18 mA. A

TDS540 Tektronix® oscilloscope was used to collect the optogalvanic signals that represent the changes in the level populations created by the laser excitation. A MATLAB® program-controlled data acquisition and the TDL50 and FL2002 laser wavelength scans. A Jobin-Yvon monochromator was used to check the wavelengths at a precision level 10^{-5} before starting the scan.

4.5 Dye Lasers

4.5.1 Quantel TDL50 Dye Laser

The optical layout of the TDL50 dye laser is shown in Fig. 4.6. It comprises an oscillator and two amplification stages, implemented by two optically pumped dye cells. There are two folding prisms and two lenses along the laser beam path to control the beam diameter and divergence. All the dye cells are transversely pumped by the same vertically polarized beam emitted by the Nd:YAG laser. Two beam splitters divert 5% and 10% of the pump beam toward the oscillator and the pre-amplifier cell respectively, while the remaining portion of the beam is used to pump the (main) amplifier cell. The pump beam is focused into the dye cells by adjustable cylindrical lenses, creating population inversion in a thin layer behind the entrance window along the focal line of the lens.

The laser cavity included an oscillator dye cell, a grating and two totally reflecting mirrors. Light coming from the dye cell is diffracted from the grating and directed toward the rear mirror and then is reflected back. The grating was operated in the first order and it has 2400 lines/mm. Total internal reflection off one of the cell faces then diverts the beam to the second mirror, thus closing the cavity path. Before striking the grating, the laser beam is pre-expanded by a system of prisms. The active area of the grating is further enlarged by setting it at grazing incidence (82˚), so that the largest possible number of grooves is illuminated and the spectral resolution is maximized.

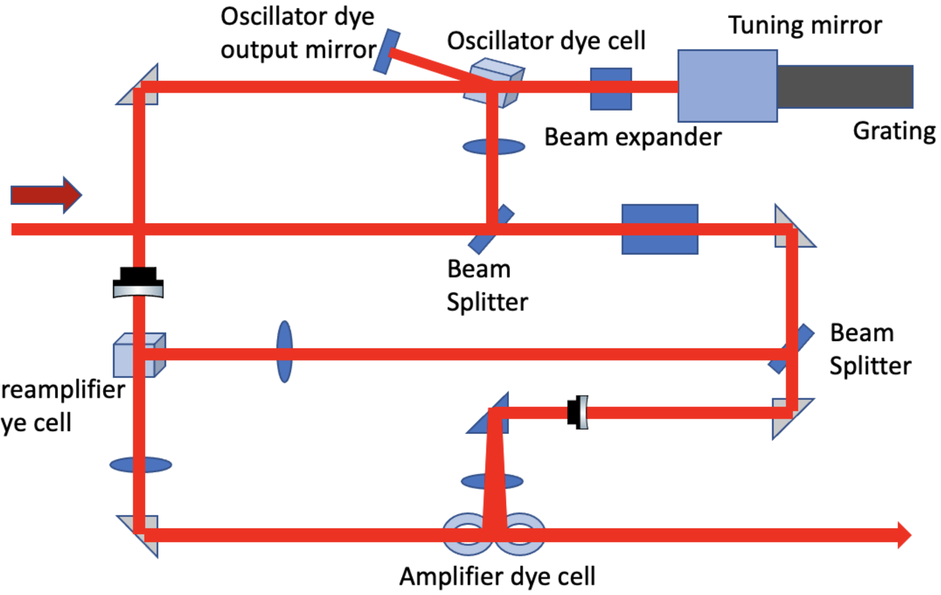

Figure 4. 6 Optical layout scheme of the Quantel TDL50 dye laser [Adapted from 13].

Moreover, the power density on the grating surface is reduced to avoid surface damage. Wavelength tuning is achieved by tilting the cavity rear mirror around a horizontal axis centred on the grating. The tuning curve is given by:

$$\lambda = \frac{d}{m}(\sin\alpha + \sin\beta) \cong \frac{d}{m}(1 + \sin\beta) \qquad (4.2)$$

where d is the groove spacing, m is the grating order, α is the grazing incidence angle and β is the angle formed by the normal to the mirror and to the grating surface. A linear wavelength variation is induced by mechanical tilting of the mirror, which is driven by a sine bar mechanism.

A mixing cell, including a KDP crystal, is placed in the beam path to exploit nonlinear processes, which allows to extend the wavelength range of tunability to the UV region. A prism is used to steer the beam from the last amplifier toward the mixing unit. Since the Nd:YAG pulses and the dye pulses must overlap in time and space to give rise to the sum frequency wave, a set of mirrors introduce a proper delay along the path of the Nd:YAG laser beam. The dye beam and the Nd:YAG fundamental beam are aligned to cross in the middle of the mixing cell. The KDP crystal, operated with the correct tilt angle, is used to fulfil the phase matching condition and achieve significant wavelength conversion efficiency.

4.5.2 Lambda Physik FL2002 Dye Laser

The optical layout of the FL2002 dye laser oscillator/pre-amplifier is shown in Fig. 4.7. The vertically polarized pump beam entering the dye laser first passes through a swing-in attenuator and is then divided by a beam splitter, where a small part is reflected toward the oscillator dye-flow cuvette.

The remaining part is reflected by a folding mirror which also raises the beam height by 30 mm before the beam bounces off another mirror. After the second folding mirror, another swing-in attenuator can intercept the beam to further attenuate the pump power for the amplification stage. A pre-amplifier beam splitter follows, where 10% of the pump beam is reflected again toward the oscillator dye-flow cuvette but at a higher height than that of the oscillator pump beam which constitutes the pre-amplifier stage. No amplifier stage was used.

The oscillator cavity comprises the dye-flow cuvette and pump optics, a beam expansion system, a Littrow grating and the cavity end mirror. The oscillator beam, reflected by the end mirror, passes through the dye-flow cell and enters a multi-prism beam expander resulting in a light ribbon that impinges on a grating perpendicular to its grooves. Only if the beam wavelength satisfies the Littrow condition is light reflected back through the beam expander to the dye cell and thence to the cavity end mirror. The Littrow condition states:

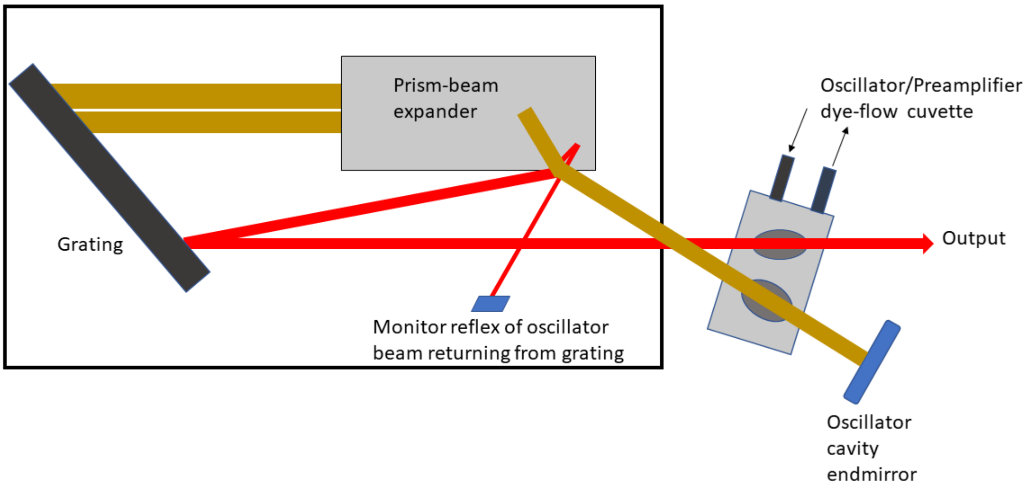

Figure 4. 7 Layout of the Lambda Physik FL2002 laser cavity [Adapted from 14].

$$\lambda = \frac{2 sin\alpha}{K} m \qquad (4.3)$$

where K is the grating constant, m is the order in which the grating is operated and α is the incidence angle. The grating can be used in the third to the eight order and tilted for wavelength linear tuning by a precision sine drive mechanism.

Enlarging the light beam incident on the grating ensures maximum spectral resolution (and corresponding minimum laser linewidth). To ensure operation of the dye laser at the desired wavelength of 415.907 nm, the grating was used in the sixth order.

4.5 Hollow-Cathode Lamps

A HCL [15] is essentially a glass (or quartz) envelope containing a hollow shaped cathode, an anode and an inert filler gas at low pressure. The cathode contains the element (metal) of interest. If the metal is stable in air and has a high melting point, the pure metal may be used (for example, Al). On the other hand, if it is brittle (for example, Mn and W), the metal powder is sintered. If it is reactive in air, or has a relatively high vapour pressure, then the metal oxide or halide is typically used (for example, Cd, Na). This powder technique is also used to produce multielement lamps where two or more metals are present.

The filler gas must be monatomic in order to avoid molecular continuum spectra and thus it must be an inert, noble gas. Hence the filler gas is usually argon or neon, with neon being the preferred choice. This is due to its higher ionization potential which produces a greater signal intensity. Argon is only used when a neon spectral line occurs in close proximity to a resonance line of the metal.

The anode is simply the electrode which provides the potential required for striking the discharge. When a discharge occurs between two electrodes via a gas at low pressure, the cathode is bombarded by the energetic, positively charged gas ions (for example, ionized filler gas atoms) which are accelerated towards its surface by the potential difference across the discharge. The energy of these ions is such that atoms of the cathode material are ejected or “sputtered” into the plasma. Here they may collide with other high energy particles which are present. These collisions result in a transfer of energy causing the metal atoms to become excited. Since this excited state is not stable, the atoms relax back to their ground state, emitting radiation at the characteristic wavelength of that element. For most elements, more than one analytically useful spectral line is generated.

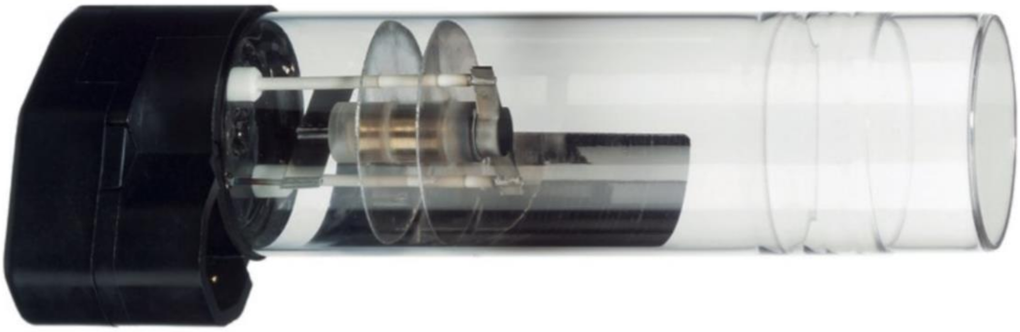

Figure 4. 8 The Heraeus Noblelight Hollow-Cathode Lamp (HCL) used in this work [15].

The molybdenum HCL used in this work was supplied by Heraeus-Noblelight [15] The lamp is shown in Fig. 4.8. It was operated at a current of 18 mA. The power supply provided a current of up to 40 mA at a voltage that could be varied from 0 – 1000V, Model BHK-MG-40 from KEPCO Inc. of the USA (Fig. 4.9).

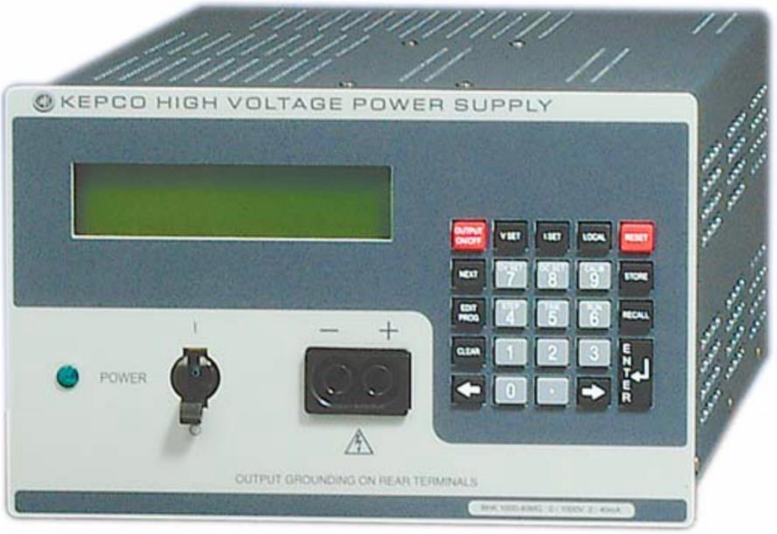

Figure 4. 9 The Kepco Inc. 40 watt power supply used in this work to drive the HCL [16].

4.6 TDS540 Tektronix® Oscilloscope

Signals were collected by a TDS540 Tektronix® oscilloscope, a portable, four-channel instrument suitable for use in a variety of test and measurement applications and systems. Key features include four input channels, each with 8-bit vertical resolution and a selectable record length of 500 to 15,000 samples. A 50,000 sample record length is available with the 1M option. All four input channels can acquire and display waveforms simultaneously. Each of the four channels can be displayed, vertically positioned, and offset, can have their bandwidth limited (100 MHz or 20 MHz) and their vertical coupling specified. Fine gain can also be adjusted.

A maximum digitizing rate of 1 Gigasamples/second with an analog bandwidth of 500MHz and extensive triggering capabilities: such as edge, logic and glitch. Full programmability and printer/plotter output. Advanced functions like continuously updated measurements and local pass/fail decision making. Specialized display modes, such as waveform averaging and variable persistence. A unique graphical user interface (GUI), an on-board help mode, and a logical front-panel layout which combine to deliver a new standard in usability.

Figure 4. 10 The Tektronix® TDS540 Oscilloscope [17].

Besides the four channels, up to three math waveforms and four reference waveform operations, such as add, are specified on any two channels. A reference waveform results when you save a live waveform in a reference memory.

4.7 Summary

In this chapter, the background of the SPES project is introduced. The main aim of the project, which is to provide high intensity and high-quality beams of neutron-rich nuclei for forefront research on nuclear structure, reaction dynamics and interdisciplinary fields like medical, biological and material sciences, is stated. The two-colour resonant laser photoionization experiment on Mo in a hollow cathode lamp (HCL) is described. The tuneable dye lasers and the hollow cathode lamp used are introduced. All the data presented in chapter 6 was taken with this system.

References

[1] G. Prete, A. Andrighetto, M.Manzolaro, S.Corradetti, D.Scarpa, M.Rossignoli, A.Monetti, M.Lollo, M.Calderolla, J.Vasquez, D.Zafiropoulos, L.Sarchiapone, D.Benini, P.Favaron, M.Rigato, R.Pegoraro, D.Maniero, L.Calabretta, M.Comunian, M.Maggiore, A.Lombardi, L.Piazza, A.M.Porcellato, C.Roncolato, G.Bisoffi, A.Pisent, A.Galatà, M.Giacchini, G.Bassato, S.Canella, F.Gramegna, J.Valiente, J.Bermudez, P.F. Mastinu, J.Esposito, J.Wyss, S.Zanella. The SPES project at the INFN- Laboratori Nazionali di Legnaro. *EPJ Web of Conferences* **66**, 11030 (2014)

[2] www.eurisol.org

[3] http://www.lnl.infn.it/index.php/it/

[4] K. Nedunchezhian, N. Aswath, M. Thiruppathy, and S. Thirugnanamurthy, Boron Neutron Capture Therapy - A Literature Review. *J Clin Diagn Res.* **10**, 12 (2016)

[5] OECD/NEA, The Supply of Medical Isotopes: An Economic Diagnosis and Possible Solutions, OECD Publishing, Paris 2019 (https://doi.org/10.1787/9b326195-en.)

[6] R. Nave. "Technetium-99m". Hyper Physics. Georgia State University.

[7] The National Research Council. *Medical Isotope Production Without Highly Enriched Uranium* (Report). (2012)

[8] P. A. Bokhan, V. V. Buchanov, N. V. Fateev, M. M. Kalugin, M. A. Kazaryan, A. M. Prokhorov, D. E. Zakrevskii, Laser Isotope Separation in Atomic Vapor. Wiley-VCH, Berlin, August 2006

[9] D. Scarpa, L. Biasetto, S. Corradetti, M. Manzolaro, A. Andrighetto, S. Carturan, G. Prete, P. Zanonato, and D.W. Stracener, Neutron-rich isotope production using the uranium carbide multi-foil SPES target prototype. *Eur. Phys. J. A* **47**, pp 32 (2011)

[10] M. Iannelli, Study on laser resonance photoionization of molybdenum atoms. Masters Degree Thesis, University of Pavia, 2017

[11] D. Scarpa, A. Barzakh, D. Fedorov, A. Andrighetto, E. Mariotti, P. Nicolosi, and A. Tomaselli, First results on Ge resonant laser photoionization in hollow cathode lamp. *Rev, Sci. Instrum.* **87**, 02B708 (2016)

[12] P. P. Sorokin and J. R. Lankard, Stimulated emission observed from an organic dye, chloro-aluminum phthalocyanine, *IBM J. Res. Dev.* **10**, 162 (1966)

[13] Quantel TDL50 dye laser operator manual

[14] Lambda Physik FL2002 dye laser operator manual

[15] https://www.heraeus.com/en/hng/home_hng/home_noblelight.html

[16] https://www.kepcopower.com/bhkmgmd.htm

[17] TDS540 Tektronix® Oscilloscope user manual (https://uk.tek.com/oscilloscope/tds540-manual/tds-520-540-digitizing-oscilloscopes-user-manual)

Chapter 5 Results of DLP Experiments

5.1 Introduction

Atomic ions are a major constituent of matter in the universe and as such they play a pivotal role in astrophysics [1]. Spectroscopic observations from the EUVE, Chandra and XMM-Newton satellites, emphasized the need for highly accurate atomic data in the extreme ultraviolet (EUV) and soft X-ray spectral range. Ions such as Pb^+ [2] and Bi^{2+} [3,4] have attracted attention for the study of stellar evolution and the investigation of the chemical composition of peculiar stars, respectively.

On Earth, tokamaks generate plasmas with very similar parameters to those of the solar corona [5]. Thus, soft X-ray emission measurements in heavy atoms including Bi and Pb have been performed in the TEXT tokamak [6]. From a different point of view, EUV emission measurements on high Z atomic ions performed in the Large Helical Device (LHD) highlighted their contribution to fusion research [7]. Development of an alternative device, the so-called Electron Beam Ion Trap (EBIT) allowed for measurements of electron-ion excitation cross sections of high Z atomic ions (e.g., [8]). Furthermore, atomic ions have attracted interest as potential active media for high harmonic generation (HHG) [9,10].

Two important techniques have been developed to probe photoabsorption in atomic ions, namely merged synchrotron-ion beams [11–13] and the dual laser plasma (DLP) method [14,15]. The former was first implemented at the Daresbury Synchrotron Radiation Source [16,17] and has the distinct advantage of being able to provide data on absolute cross sections. Despite its innovative nature, early studies at synchrotrons suffered from weak signal rates due to the low density of ions. Measurements at third generation synchrotron sources such as SOLEIL [18], ALS [19] and PETRA III [20] led the way to the partial resolution of this issue as a result of the increased brightness of the sources. The DLP technique offers a table-top alternative, with potential single shot sensitivity, that has been extensively used to perform ionic photoabsorption measurements (e.g. [21–25]). However, it provides only relative photoabsorption cross sections. In this sense the two techniques are complementary. The DLP technique is used here to perform VUV photoabsorpion measurements on Tl-like ions Pb II and Bi III.

The first absorption spectra of Pb I and Bi I were acquired almost half a century ago at the Frascati synchrotron [26]. Further studies by Connerade and co-workers [27,28] focused on the enhancement in the production of Pb^{2+} from 5d excited Pb as compared to Tl. The authors suggested an 'autoionization into the double-ionization continua' as the underlying process to explain the aforementioned observation whereas Holland and Codling [29] emphasized the significance of Auger processes. Besides these synchrotron experiments, investigations into lead and bismuth ions [30,31,32] were carried out by means of discharge spectroscopy. In addition, Banahan and co-workers [33] applied the DLP technique to measure Hg I-like Pb III and Bi VI photoabsorption spectra in the 19-41 nm spectral region, where 5d excitation plays a major role.

The photoabsorption spectra of neutral and single ionized Bi and Pb in the 37 – 121 nm region are presented in the first part of this chapter. The overall shapes of the spectra are compared with total cross sections obtained with the aid of the RTDLDA codes of Liberman and Zangwill [34,35]. And the lines have been identified by comparing with literature. In the second part of this chapter, here, we report photoabsorption measurements of Bi III in the range 37-57 nm. We discuss the measured spectrum for Bi III and the data for Pb II from the 37-70 nm spectral region in the light of calculations employing the Cowan code. To our knowledge, this part of the spectrum is rather unexplored for both species as there appears to be no spectroscopic data available up until now. Our findings suggest the presence of excited states in both ionic species. Evidence of excited states have been previously reported in the DLP absorption spectra of several ions: Si^{+} [36], Si^{2+} [37], Si^{3+} [38] and Cr^{+} [39]. In parallel, observations of excited states have been reported for merged synchrotron-ion beam experiments in Ar^{+} [40], C^{4+} [41], C^{+} [42], Al^{+} [13] and Mn^{+} [43].

5.2 Photoabsorption Spectra of Bi I, Bi II and Bi III

The ground-state configuration of atomic bismuth is $6s^26p^3$ ($^4S_{3/2}$). The spectrum of Bi was analysed by McLennea, McLay and Crowford in 1930 [44] and corrected later by Crawford and McLay [45] in 1934. Fisher and Goudsmit [46] measured the hyperfine structure of Bismuth in 1930. The available data on Bi II were compiled by Moore in 'Atomic energy levels' [47] in 1958. The absorption spectrum of bismuth in the 2300-1250 Å region was obtained by Joshi and Srivastava [48] using the flash pyrolysis technique in 1978. Their analysis was based on series converging on $6p^2$ $^3P_{0,1,2}$ limits of Bi II and the determination of the first ionization limit was improved by 25 cm^{-1} to 58 765 cm^{-1}. But there were still many lines which could not be assigned to any known transitions. Suzer et al. [49] studied the photoelectron spectra of Bi I and Bi II and reported that the relativistic effects have no influence on the relative photoionization cross sections of $^3P_{0,1,2}$ limits. Young et al. [50] studied the bismuth spectrum using three-photon hybrid resonance techniques and reported three even parity series based on a $^3P^0$ core, namely ns $^4P_{1/2}$, nd $^2D_{3/2}$ and nd $^2D_{5/2,}$ and a large number of odd parity levels. Mazzoni et al. [51] recorded the photoabsorption spectrum of bismuth in the 400-1900 Angstrom region on a 3 m normal incidence spectrograph using the flash pyrolysis technique. The relative photoionization cross sections of atomic bismuth obtained in the 1780-430 Å region were new. The measurements had been used to revise, confirm and extend earlier analyses. Two new series converging on the $6p^2$ $^1D_2$ term and four new series converging on the $6p^2$ $^3P_2$ term had been identified.

The absorption spectra of Bi I, Bi II and Bi III in the 37-121 nm region were recorded here using the DLP facility at Dublin City University. The output of a pulsed Nd: YAG laser was focused onto a tungsten rod to produce the back-lighting plasma source of continuum radiation. A second laser was fired onto our target bismuth to generate the absorbing plasma, which was situated on the optical axis between the back-lighting plasma and the entrance slit of the ARC VM521 spectrometer. In the current experiment we chose specific experimental parameters, namely laser power density, time delay between absorbing plasma ignition and backlighting plasma ignition, along with the distance between the target and the optical axis, which in turn allowed us to isolate atomic Bi, Bi^{+} and Bi^{2+} ions. This was ensured by recording the photo-absorption spectra of these ions at longer wavelengths, where the spectra are already known and can be compared with the dual laser plasma (DLP) results.

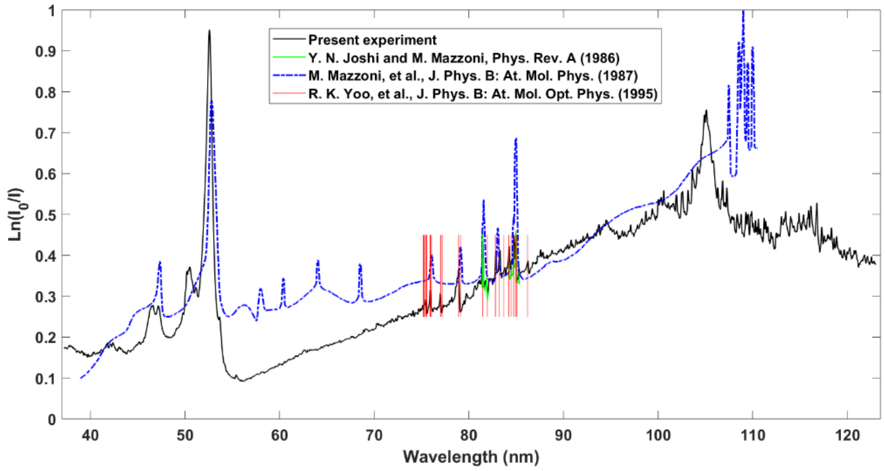

Figure 5. 1 The absorption spectrum of atomic Bi measured in the present experiment (black curve) at a time delay of 1000 ns and a distance of 0.8 mm away from optical axis. These parameters were found empirically to optimise the atomic Bi fraction in the absorbing plasma. The present data are compared with the literature [51, 52, 53].

In Fig. 5.1, the black curve represents the current experimental data obtained from the DLP experiment. The blue dashed curve is the photoabsorption spectrum presented in the paper of Mazzoni et al. [51] which they obtained in a flash pyrolysis experiment that used a spark discharge as the VUV backlighting source. The red sticks represent the wavelengths of Bi I lines measured by Yoo et al. [52]. The green spectrum is taken from Fig 1. of Joshi and Mazzoni [53] and exhibits two strong Bi II lines at 81.5 nm and 85.3 nm while the other lines are mainly due to absorption by atomic bismuth. Looking at the spectrum taken from reference [51] there appears to be a wavelength shift in the region of 110 nm for which there is no explanation at present. Also, the discrete features in the 55 – 70 nm region are not observed in the present experiment. The reason could be a lack of spectral resolution in the present DLP experiment. Finally, large resonances, due to 5d to 6p transitions were observed in the 52 – 55 nm spectral range [51] and are also seen in the DLP results on Fig. 5.1.

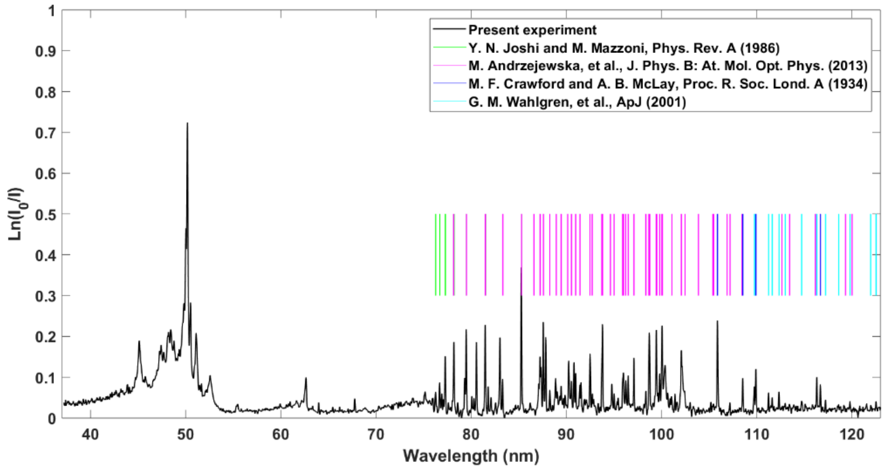

Figure 5. 2 The absorption spectrum of Bi II, recorded at a time delay of 1000 ns and a distance of 8.7 mm from optical axis (black curve – present experiment). These parameters were found empirically to optimise the Bi^+ ion fraction in the absorbing plasma. For comparison the wavelengths of Bi II lines, taken from a series of papers [45, 53, 54, 55], are shown as coloured sticks [blue, green, magenta, cyan respectively].

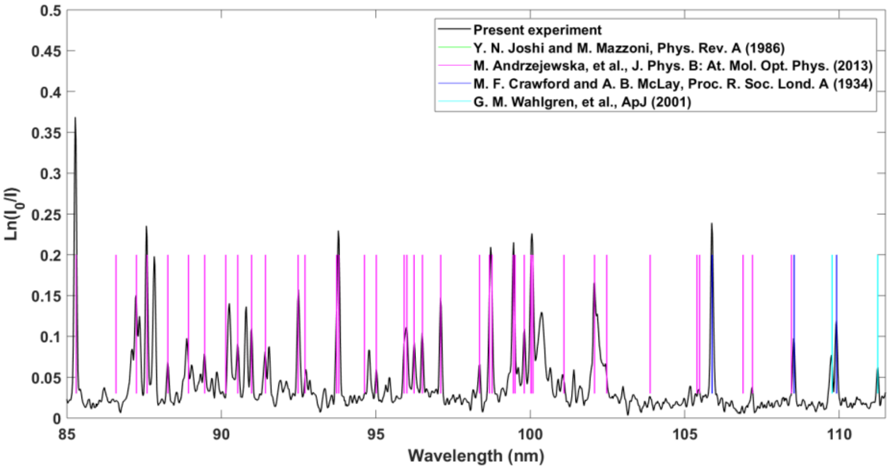

Figure 5. 3 Same as Fig. 5.2 but restricted to the 85 - 110 nm wavelength region where a finer comparison with the Bi II lines taken from references [45, 53, 54, 55] can be made.

Fig. 5.2 shows the photoabsorption spectrum of Bi^+. The coloured sticks (lines) are from references 45, 53, 54 and 55. The green lines are taken from the absorption spectrum of Bi II obtained by Joshi et al. [53] while the magenta lines correspond to the wavelengths measured by Andrzejewska et al. [54]. The cyan lines represent Bi II lines recorded by Wahlgren et al. [55] while the blue sticks represent Bi II wavelengths measured by Crawford and McLay [45]. Fig. 5.3 provides a closer look at the 85 – 110 nm wavelength region of Fig. 5.2.

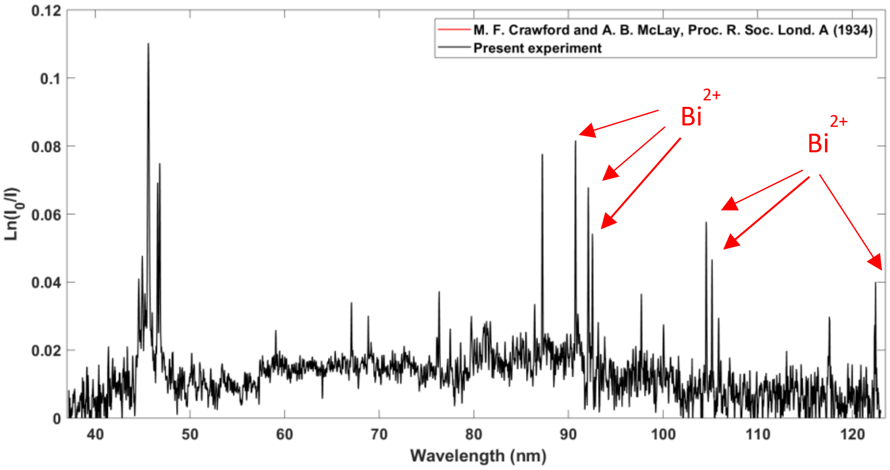

Figure 5. 4 The absorption spectrum of Bi III at a time delay of 200 ns and a distance of 0.8 mm away from optical axis. These parameters were found empirically to optimise the Bi^{2+} ion fraction in the absorbing plasma. Comparison is made with the Bi III lines taken from [45].

Fig. 5.4 shows the photoabsorption spectrum of Bi III recorded at a time delay of 200 ns and full laser pulse energy (460 mJ). The Bi target was located at 0.8 mm away from the optical axis. The Bi^{2+} ion was thus isolated, and its spectrum recorded under these conditions. Some Bi III lines in 88-123 nm wavelength region are highlighted in Fig. 5.4 using identifications from reference [45].

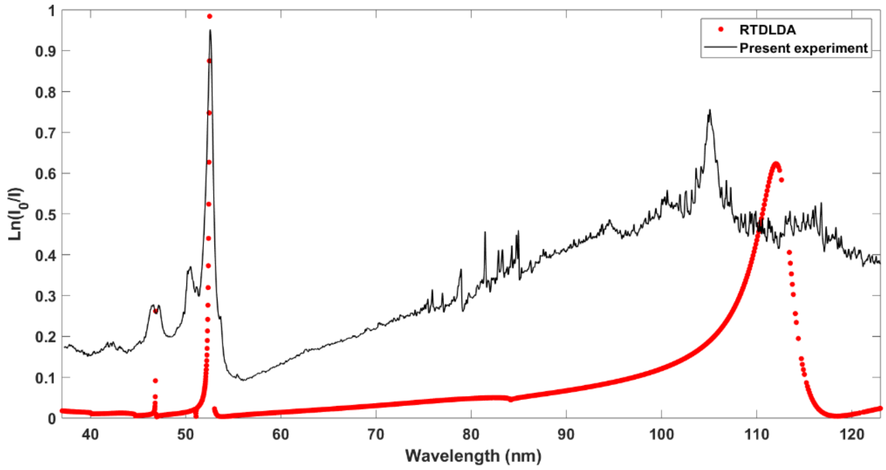

Figure 5. 5 Comparison of experiment (black curve from Fig. 5.1) with a RTDLDA calculation (red dotted curve) for atomic Bi. The experimental data are unscaled and represent relative absorption. The RTDLDA cross section data have been scaled to lie within the same range of 0 to 1.

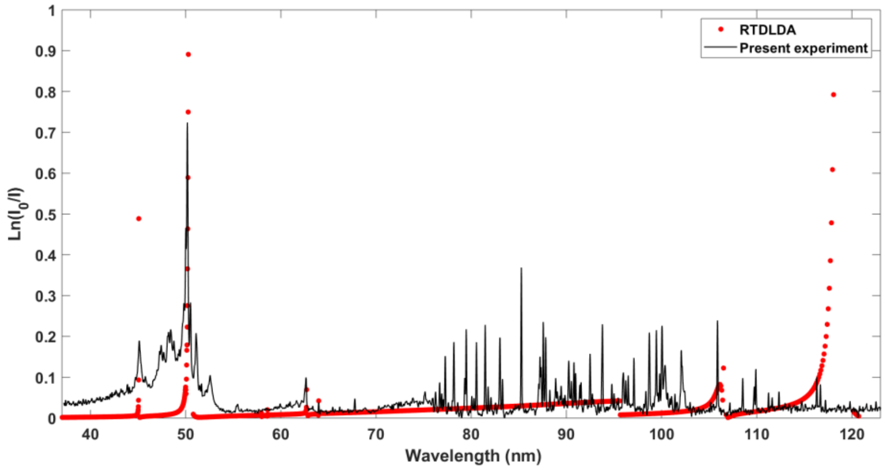

Figure 5. 6 Comparison of experiment (black curve from Fig. 5.2) with a RTDLDA calculation (red dotted curve) for singly ionized Bi. The experimental data are unscaled and represent relative absorption. The RTDLDA cross section data have been scaled to lie within the same range of 0 to 1.

The RTDLDA code has been used to calculate the absolute cross sections of Bi and Bi^{+}. Fig. 5.5 shows the comparison of the current experimental data with the RTDLDA results. The black curve is the photoabsorption spectrum of neutral Bi and the red dots show the RTDLDA computed cross section. The calculation matches the broad feature of the current experiment and it also shows the 5d to 6p transitions at 52.6 nm. Fig. 5.6 is the comparison of experiment data and the RTDLDA results for Bi^{+}. The RTDLDA calculation does not really reproduce the discrete features of the spectrum, except for perhaps the very strongest features, albeit shifted to lower photon energies. For this reason, the Cowan suite of atomic structure codes will be used to reproduce better the discrete features of the spectrum later in the chapter.

In summary, the Bi, Bi^{+} and Bi^{2+} ions have been isolated and their VUV photoabsorption spectra measured in a dual laser plasma (DLP) experiment. The present spectra have been compared with previously reported measurements form a range of different experiments, both emission and absorption [45, 51-55]. The DLP spectra are in reasonable agreement with those already published, albeit some wavelength shifts are present. That stated, the comparisons give confidence in the assignment of the ion stages for Fig. 5.1 (B I), Fig. 5.2 (Bi II) and Fig. 5.4 (Bi III). The total photoionization cross sections have been calculated with the aid of the RTDLDA code [35]. The computed cross sections display overall good agreement with the broad spectral distributions for atomic bismuth and its lowly charged ions, albeit they do not reproduce the fine spectral details. For these, detailed atomic structure calculations are needed [e.g., 12].

5.3 Photoabsorption Spectra of Pb I and Pb II

The Pb I absorption spectrum plays an important role in the study of excitation of the d-subshells of atoms. In 1966, Garton & Wilson [56] investigated the Pb I absorption spectrum, and they found several long series converging on the ground levels of singly ionized Pb and classified them as resulting from the excitation of a single 6p electron. Brown, Tilford & Ginter [57] re-investigated the Schumann region absorption spectrum of lead vapour between 135 and 204 nm using a 6.6-m normal incidence spectrograph operated in third and fourth order so that they achieved higher dispersion, and hence spectral resolution, than previous work by others. They observed many new spectral features, including five electric quadrupole transitions and 31 nuclear spin induced transitions from the ^{207}Pb isotope. Connerade et al. [27] obtained the 32-107 nm range absorption spectrum of lead vapour. They found inter-channel interactions and more than 60 transitions due to excitation of either a 5d or 6s electron. The present absorption spectra of lead atoms and ions were obtained using the DLP facility at Dublin City University. Using tungsten as the back-lighting continuum plasma, the photoabsorption spectra of atomic (Pb I) and singly ionized (Pb II) lead have been obtained by changing the laser pulse irradiation conditions, the time delay between the formation of the front and backlighting plasmas and the position of the absorbing plasma with respect to the optic axis of the spectrometer. The Pb II spectrum was recorded at a time delay of 150 ns while the surface of the Pb target was set at a displacement of 0.85 mm from the optic axis of the spectrometer. This contrasts with parameters for recording the VUV spectrum of atomic Pb, where the time delay was significantly increased to 750 ns, while the target surface was moved closer to the optic axis, namely to 0.55 mm. For the shorter time delay one can expect that region of interest in the Pb plasma plume to be hot enough to produce ions. In practice it was found that a time delay of 150 ns led to the optimisation of Pb^+ ion fraction there. As time proceeds, the ions move away from the target surface and the neutral atoms remain so that the atomic photoabsorption spectrum can be recorded. In this case, the atomic Pb fraction was found to be optimal around a time delay of 750 ns.

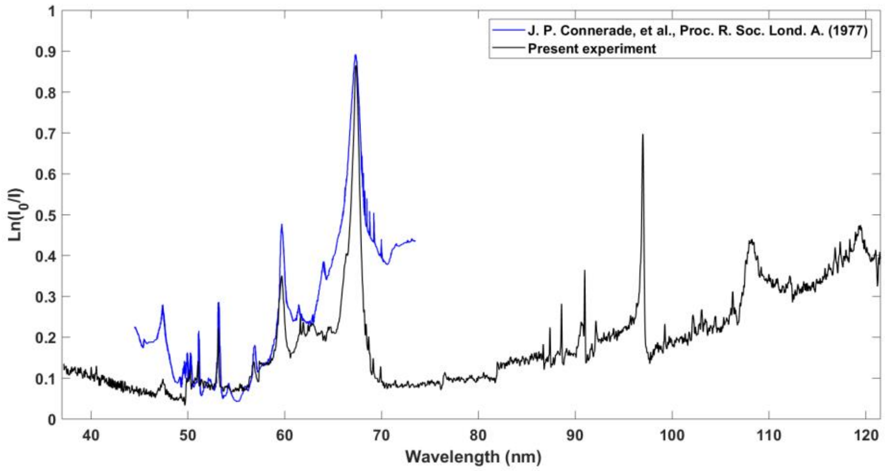

Figure 5. 7 The absorption spectrum of atomic Pb at 750 ns. The Pb target was set 0.55 mm away from the optical axis (black curve). The measured spectrum is compared with the Pb I spectrum taken from Connerade et al. [27] – blue curve.

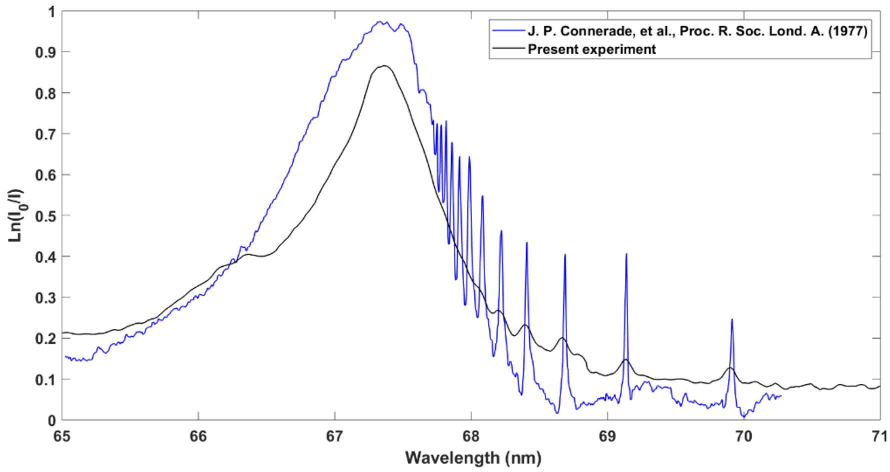

Figure 5. 8 A closer look at the 65- 72 nm wavelength region from the preceding figure.

The black curve in Fig. 5.7 is a plot of present experimental data. This spectrum was obtained at a time delay of 750 ns with 0.45 J laser pulse energy on the lead surface. The blue curve shows the spectrum from Connerade et al. [27] and was scaled by making the heights of the sharp features around 53 nm equal to each other. Fig. 5.8 is a closer look at the 65 – 71 nm range of the preceding figure. In this case the scanned data from reference [27] were scaled so that the smooth region around 66 nm matched reasonably with the present experimental data. Quite good agreement between the two Pb I spectra is observed, albeit the resolution for the present data (ca. 0.05 nm) is lower than in [27], and so the lines are broadened and damped.

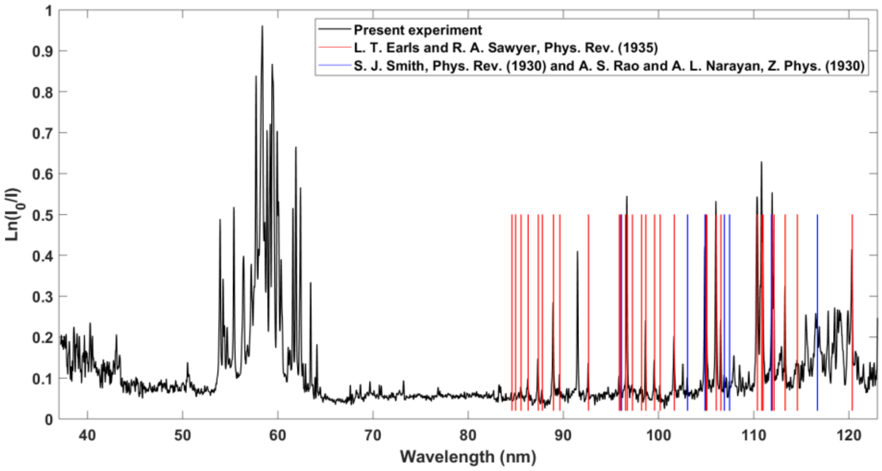

Figure 5. 9 The absorption spectrum of Pb$^+$ at a time delay of 150 ns. The Pb target surface was set 0.85 mm away from the optical axis of the spectrometer. The vertical sticks represent the positions of known Pb II (red) and Pb II (blue) lines taken from references [58, 59, 60].

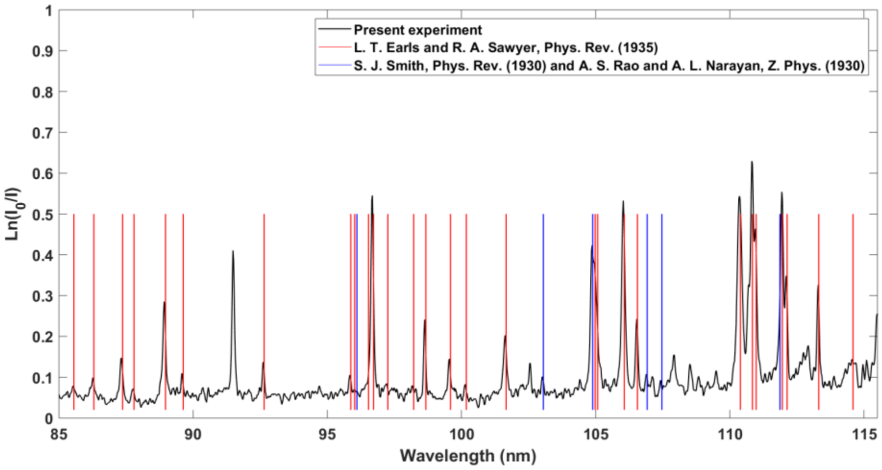

Figure 5. 10 A closer look at the 85 - 115 nm wavelength region and comparison with Pb II [58] (red) and Pb III (blue) lines from [59, 60]. It is clear that the spectrum is dominated by the Pb$^+$ ion fraction.

As shown in Fig. 5.9, the photoabsorption spectra of singly ionized and doubly ionized lead have been partly identified. The red lines correspond to the Pb II spectrum [58] while the blue lines correspond to the Pb III spectrum [59,60]. We have good matches between these lines and our spectra in the 85-120 nm wavelength region. For Pb II, the lines at 87.37 nm, 88.97 nm, 89.63 nm, 92.64 nm, 96.72 nm, 98.64 nm, 101.7 nm, 106.1 nm, 106.6 nm, 110.4 nm, 110.8 nm, 112.0 nm, 112.1 nm, 113.1 nm and 120.4 nm have been obtained using the DLP technique. The strong absorption line at 91.48 nm is as yet unidentified but does correspond to any Pb ion feature reported in the literature or available on any atomic lines database. Fig. 5.10 is a closer look at the 85 – 115 nm wavelength region of Fig. 5.9 where it can be clearly seen that the spectrum is dominated by the Pb^+ ion fraction with only weak absorption features coming from Pb^{2+} ions.

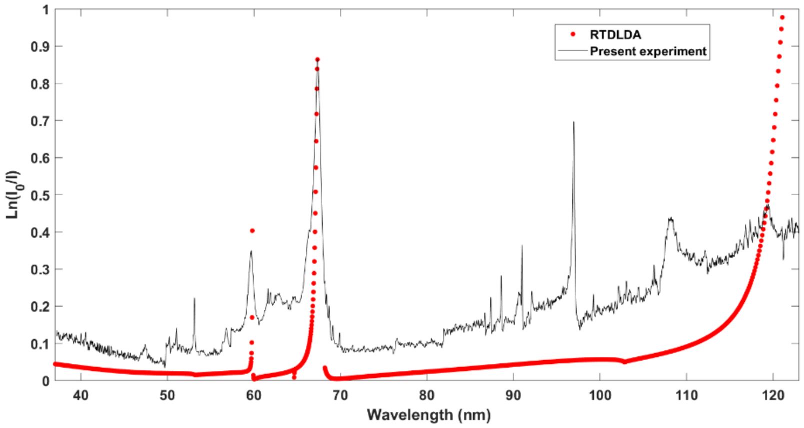

Figure 5. 11 Comparison of the present experiment (750 ns time delay, 0.55 mm away from optical axis) with a RTDLDA calculation for neutral Pb. The experimental data are unscaled and represent relative absorption. The RTDLDA cross section data have been scaled by matching the experimental and computed peaks at ca. 67.4 nm.

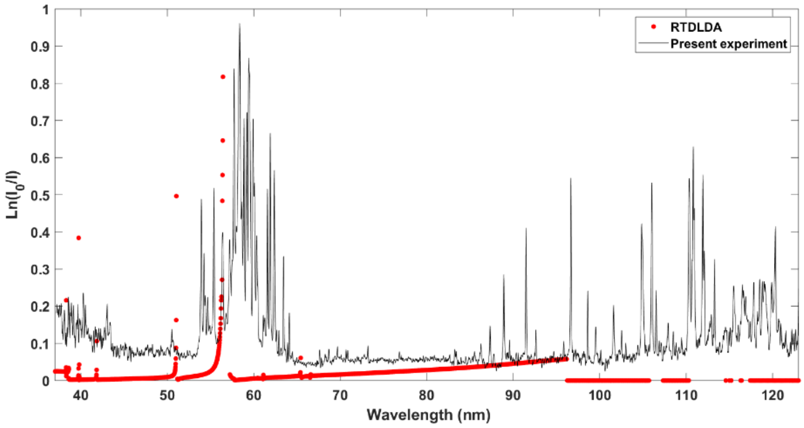

Figure 5. 12 Comparison of the present experiment (150 ns time delay, 0.85 mm away from optical axis) with the result of RTDLDA calculations for Pb II. The experimental data are unscaled and represent relative absorption. The RTDLDA cross section data have been scaled by matching the experimental and computed peaks at ca. 56.4 nm.

Fig. 5.11 and Fig. 5.12 show the comparison of the current experiment data with the RTDLDA computed cross sections for Pb and Pb II, respectively. The black curves are the present experimental data and the red ones are the RTDLDA calculation results. For Pb I, the calculation matches the experiment for the broad feature at approximately 67 nm. For Pb II, the Cowan package of codes has been used to compute the discrete features (see below).

So, in summary so far, the photoabsorption spectra of bismuth and lead have been recorded using the dual laser plasma (DLP) technique in the 37-121 nm wavelength range. The lines of Bi I and Pb I have been isolated and some lines of Bi II, Bi III and Pb II have been identified. They are in quite good agreement with those already reported in the literature. Whilst sufficient data was present in the literature to identify, and optimize, different ion stages a significant number of lines remain unidentified. Absolute VUV cross sections of lead and bismuth have been computed with the well-known (R)TDLDA codes of Zangwill [34,35], and the results of Pb I and Bi I show agreement with the current experimental data for the broadest features. The remaining unidentified lines have been computed with Cowan's suite of atomic structure codes [61] and are discussed in the following section.

5.4 The 5d-6p photoabsorption spectra of Bi II, Bi III and Pb II: evidence of excited states

In this section, the photoabsorption spectra of Bi II, Bi III and Pb II from the 5d subshell excitations in the spectral region between 37 and 70 nm are presented. With the aid of the Cowan suite of atomic structure codes, synthetic spectra have been generated and compared with experimental results. 5d → 6p transitions from the ground state ($5d^{10}6s^{2}6p^{2}$) and excited states ($5d^{10}6s^{2}6p6d$, $5d^{10}6s^{2}6p7s$, $5d^{10}6s^{1}6p^{3}$, $5d^{10}6s^{2}6p7p$) to higher energy states are recorded for Bi II. For Bi III and Pb II, 5d → 6p transitions from the ground state ($5d^{10}6s^{2}6p$) and excited states ($5d^{10}6s^{2}6d$, $5d^{10}6s^{2}7s$, $5d^{10}6s6p^{2}$, $5d^{10}6s^{2}7p$) to higher energy states are reported. In addition, evidence of excited states of Bi II, Bi III and Pb II is provided.

The Bi II photoabsorption spectrum in the 37 – 60 nm region

The absorption spectrum of Bi II in the spectral region ranging from 37 to 60 nm is shown in Fig. 5.13. It was acquired at an inter-laser delay of 1000 ns and with the absorbing plasma formed a distance of 8.7 mm away from the optical axis of the system. As noted in Section 5.2, looking at valence excited lines of Bi II at longer wavelengths, it was found that the bismuth plasma was dominated by singly charged ions for these experimental conditions. The laser was tightly focused onto the Bi target via a cylindrical lens. In order to identify the observed absorption features, a series of calculations using the Cowan suite of atomic structure codes [61] was performed.

After testing a number of possible pairs of upper and lower state configurations, the final electron configurations for each of the low-lying states were finally chosen and are given in Table 1. The values of the scaling coefficients for the Slater integrals were set to the default values given with the sample RCN2 input file which comes with the code download. Specifically, the direct (F_k) and exchange (G_k) integrals were reduced by 15%, as were the configuration interaction (R_k) integrals. In addition, the spin-orbit integrals were reduced by 5%.

In Fig. 5.13(a), we show the gf values for the 5d → 6p transitions from the ground electron configuration of Bi II. The photoabsorption cross section is related to the oscillator strength, which is in turn given by the weighted oscillator strength normalized to the multiplicity of the lower state, so the gf values were used to compare with the experiment in this work. As can be seen from the figure, 5d subshell photoabsorption from the ground configuration $5d^{10}6s^26p^2$ dominated the spectrum and resulted in the strong observed photoabsorption peaks at 50.02, 50.18 and 51.08 nm. According to calculations with the Cowan suite of atomic structure codes, these three peaks are mainly due to the transitions $5d^{10}6s^26p^2$ (^1S) $^1D_2 \rightarrow 5d^96s^26p^3$ (^2D) $^1D_2$, $5d^{10}6s^26p^2$ (^1S) $^1D_2 \rightarrow 5d^96s^26p^3$ (^2D) $^1F_3$, $5d^{10}6s^26p^2$ (^1S) $^3P_2 \rightarrow 5d^96s^26p^3$ (^4S) $^3D_3$, respectively.

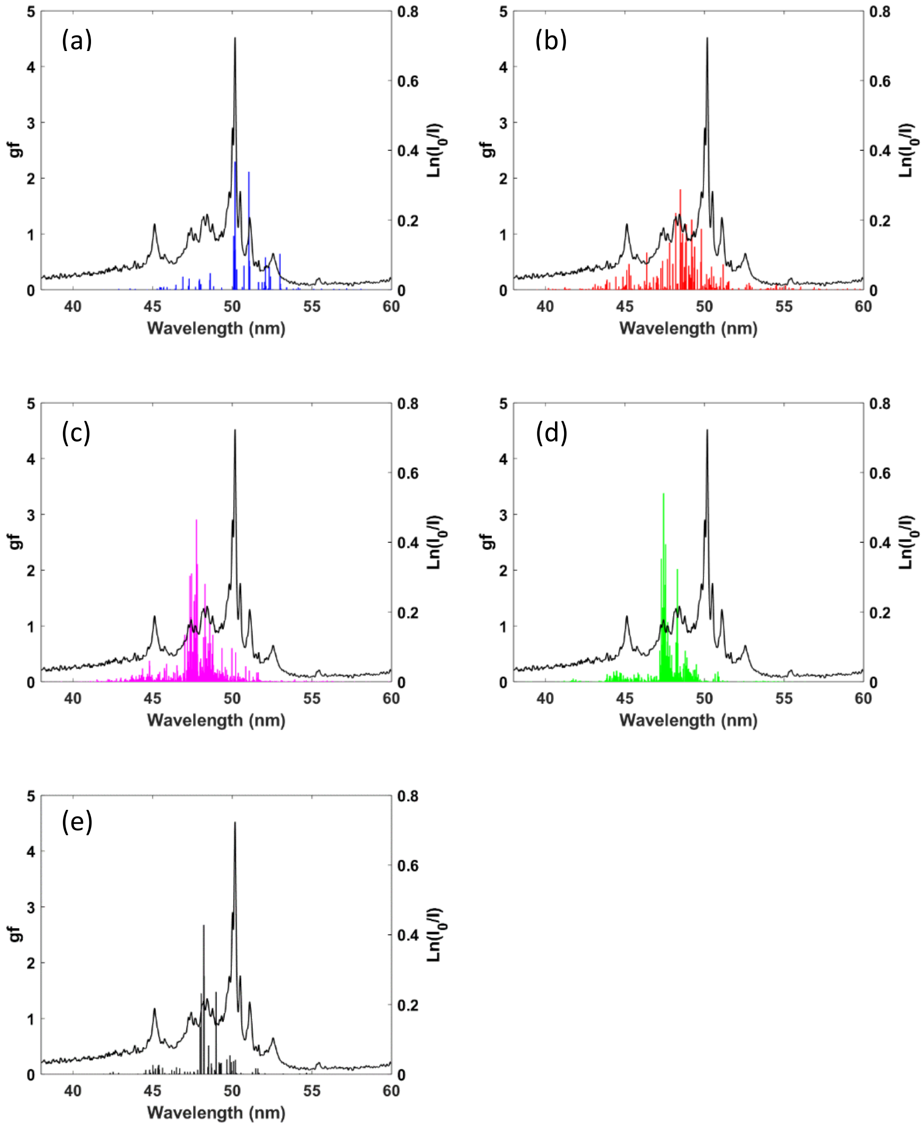

Figure 5. 13 Calculated gf values for 5d – 6p transitions arising from low-lying, excited configurations of Bi II compared to the observed spectrum. From top to bottom and from left to right: (a) $5d^{10}6s^{2}6p^{2} \rightarrow 5d^{9}6s^{2}6p^{3}$, (b) $5d^{10}6s6p^{3} \rightarrow 5d^{9}6s6p^{4}$, (c) $5d^{10}6s^{2}6p6d \rightarrow 5d^{9}6s^{2}6p^{2}6d$, (d) $5d^{10}6s^{2}6p7p \rightarrow 5d^{9}6s^{2}6p^{2}7p$ and (e) $5d^{10}6s^{2}6p7s \rightarrow 5d^{9}6s^{2}6p^{2}7s$.

In Fig. 5.13 (b,c,d,e) the contributions of 5d → 6p transitions from low-lying excited configurations of Bi II to the overall absorption spectrum, respectively, are shown. The plasma temperature was expected to be less than 2 eV for the prevailing experimental conditions, and so, since these low-lying excited states sit more than approximately 9 eV above the ground state, it can be expected that their population should be a relatively small percentage of the ground state population. As shown in Fig. 5.13, there are indeed features in the 47 - 50 nm region due to the 5d → 6p transitions from excited states of Bi II. Specifically, there are quite strong features in the 48.01–48.85 nm and 47.15 – 47.82 nm spectral regions. Some of the most intense of these transitions are listed in Table 5.1.

Table 5. 1 Transitions arising from low lying (excited) electron configurations of Bi II.

Wavelength Region (nm)	**Transitions**	**λ (nm)**	**gf values**
48.01 - 48.85	$5d^{10}6s6p^3\,(^2D)\,^3D_2 \rightarrow 5d^96s6p^4\,(^1D)\,^3F_3$	48.48	1.7998
	$5d^{10}6s6p^3\,(^2D)\,^3D_3 \rightarrow 5d^96s6p^4\,(^1D)\,^3F_4$	48.19	1.3768
	$5d^{10}6s^26p6d\,(^2P)\,^3F_3 \rightarrow 5d^96s^26p^26d\,(^3P)\,^3G_4$	48.29	1.7533
	$5d^{10}6s^26p6d\,(^2P)\,^3F_2 \rightarrow 5d^96s^26p^26d\,(^3P)\,^3G_3$	48.58	1.0639
	$5d^{10}6s^26p7p\,(^2P)\,^3D_2 \rightarrow 5d^96s^26p^27p\,(^3P)\,^3F_3$	48.29	2.0222
	$5d^{10}6s^26p7p\,(^2P)\,^3D_1 \rightarrow 5d^96s^26p^27p\,(^3P)\,^3F_2$	48.27	1.1598
	$5d^{10}6s^26p7s\,(^2P)\,^3P_2 \rightarrow 5d^96s^26p^27s\,(^3P)\,^3D_3$	48.21	2.6750
	$5d^{10}6s^26p7s\,(^2P)\,^1P_1 \rightarrow 5d^96s^26p^27s\,(^3P)\,^1D_2$	48.24	1.7633
	$5d^{10}6s^26p7s\,(^2P)\,^3P_2 \rightarrow 5d^96s^26p^27s\,(^3P)\,^3P_2$	48.05	1.1502
47.15 – 47.82	$5d^{10}6s^26p6d\,(^2P)\,^3F_4 \rightarrow 5d^96s^26p^26d\,(^3P)\,^3G_5$	47.75	2.9095
	$5d^{10}6s^26p6d\,(^2P)\,^1F_3 \rightarrow 5d^96s^26p^26d\,(^3P)\,^1G_4$	47.80	2.1086
	$5d^{10}6s^26p6d\,(^2P)\,^3F_4 \rightarrow 5d^96s^26p^26d\,(^3P)\,^3F_4$	47.45	1.9398
	$5d^{10}6s^26p6d\,(^2P)\,^3P_2 \rightarrow 5d^96s^26p^26d\,(^1D)\,^3D_3$	47.34	1.9009
	$5d^{10}6s^26p7p\,(^2P)\,^3D_3 \rightarrow 5d^96s^26p^27p\,(^3P)\,^3F_4$	47.43	3.3784
	$5d^{10}6s^26p7p\,(^2P)\,^3D_3 \rightarrow 5d^96s^26p^27p\,(^3P)\,^3D_3$	47.28	2.2064
	$5d^{10}6s^26p7p\,(^2P)\,^1D_2 \rightarrow 5d^96s^26p^27p\,(^3P)\,^1F_3$	47.55	2.4676

Table 5.1 includes some of the strongest predicted transitions arising from low-lying (excited) electron configurations of Bi II. The contributions from the excited states were particularly complex as many transitions were possible. For $5d^{10}6s^26p^2 \rightarrow 5d^96s^26p^3$, there were 97 transitions in the calculation, 61 of them with a gf value greater than 0.01. For $5d^{10}6s6p^3 \rightarrow 5d^96s6p^4$, there were 353 transitions in the calculation, 180 of them with a gf value greater than 0.01. For $5d^{10}6s^26p6d \rightarrow 5d^96s^26p^26d$, there were 1506 transitions in the calculation, 591 of them with a gf value greater than 0.01. For $5d^{10}6s^26p7p \rightarrow 5d^96s^26p^27p$, there were 860 transitions in the calculation, 297 of them with a gf value greater than 0.01. For $5d^{10}6s^26p7s \rightarrow 5d^96s^26p^27s$, there were 123 transitions in the calculation, 69 of them with a gf value greater than 0.01.

In Fig. 5.14, we show the measured photoabsorption spectrum of Bi II compared with synthetic spectra built from the convolution of the gf values with a Gaussian function (0.045 nm FWHM), chosen to represent the spectrometer instrument function. In Fig. 5.14(a), the simulation included photoabsorption from the ground electron configuration only. The resulting synthetic spectrum exhibited reasonable agreement with the experimental data. The relative heights and positions of the overall spectrum and some discrete features were reproduced by the calculation, specifically, the discrete photoabsorption features at 50.02 nm ($5d^{10}6s^{2}6p^{2}$ (^{1}S) $^{1}D_{2} \rightarrow 5d^{9}6s^{2}6p^{3}$ (^{2}D) $^{1}D_{2}$), 50.18 nm ($5d^{10}6s^{2}6p^{2}$ (^{1}S) $^{1}D_{2} \rightarrow 5d^{9}6s^{2}6p^{3}$ (^{2}D) $^{1}F_{3}$) and 51.08 nm ($5d^{10}6s^{2}6p^{2}$ (^{1}S) $^{3}P_{2} \rightarrow 5d^{9}6s^{2}6p^{3}$ (^{4}S) $^{3}D_{3}$). In Fig. 5.14(b), we added contributions due to photoabsorption from these low-lying excited states to Fig. 5.14(a). The gf values for the associated transitions were multiplied by a small factor (5%) before including them in this synthetic spectrum.

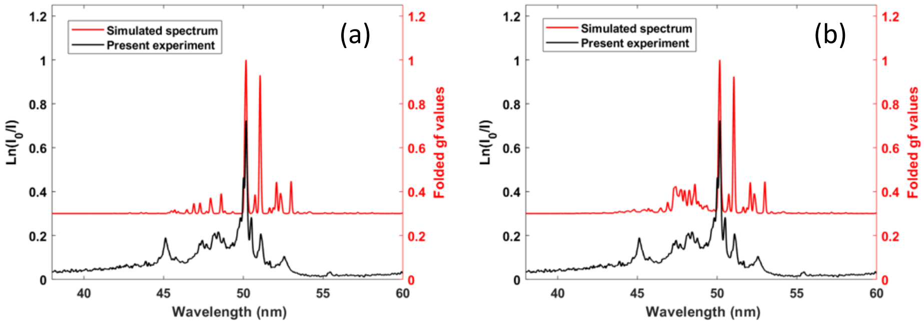

Figure 5. 14 A comparison between the synthetic spectra and experimental data. (a) Simulated spectrum including photoabsorption from the ground electron configuration of Bi^{+} only. (b) Simulated spectrum including photoabsorption both from the ground and from low-lying excited states of Bi II. The simulated spectra have been shifted upwards by a value of 0.3.

This is in line with the low plasma temperature alluded to the above. It is clear that the transitions did indeed make a small but finite contribution to the overall spectral distribution.

In summary the quite unexplored spectral region (37–60 nm) of the Bi II spectrum was investigated. The 5d → 6p transitions, arising from levels associated with the ground state electron configuration, were identified as the dominant contributors to the observed spectrum. The experimental findings were complemented by theoretical calculations performed with the aid of the Cowan suite of atomic structure codes. Using the computed data, the synthetic spectrum of Bi II was constructed in the spectral region of interest and reproduced the overall shapes and some of the discrete features of the experimental spectrum quite well. Importantly, 5d → 6p transitions from low-lying excited states are believed to make a small but finite contribution to the Bi II spectrum for the present experimental conditions, mostly in the 47–50 nm spectral range.

The Bi III photoabsorption spectrum in the 40 – 50 nm region: Evidence for excited state absorption

In Fig. 5.15 we present the photoabsorption spectrum of Bi III in the region between 40 and 50 nm, acquired at an inter-laser time delay of ≈ 200 ns and a distance of 0.8 mm away from the target surface. The gf values shown in Fig. 5.15 were calculated using the Cowan suite of atomic structure codes [61] to help identify the absorption features. In order to optimize the calculations, the Slater-Condon parameters were reduced as follows, the F_k integrals between equivalent electrons were reduced by 15% and F_k integrals between non-equivalent electrons also were reduced by 15%. The exchange interaction integrals (G_k) were reduced by 15% and the configuration interaction integrals (R_k) were also reduced by 15 percent. In addition, the spin-orbit parameters were reduced by 5%.

Significant photoabsorption from 5d → 6p transitions for several states of the doubly charged bismuth ion is expected in this region of the spectrum. As the Cowan code calculations indicate (see Fig. 5.15), 5d subshell photoabsorption from the ground configuration $5d^{10}6s^{2}6p$ and the excited configurations $5d^{10}6s^{2}6d$, $5d^{10}6s^{2}7s$, $5d^{10}6s^{2}7p$ and $5d^{10}6s6p^{2}$ dominate the spectrum.

In Fig. 5.15, we show the contribution of each configuration to the overall absorption spectrum in five separate panels. We have observed that transitions from the ground state $5d^{10}6s^{2}6p$ make a big contribution to the photoabsorption peaks at 46.58 nm and 46.80 nm. Similarly, $5d^{10}6s6p^{2} \rightarrow 5d^{9}6s6p^{3}$, $5d^{10}6s^{2}7s \rightarrow 5d^{9}6s^{2}6p7s$ and $5d^{10}6s^{2}7p \rightarrow 5d^{9}6s^{2}6p7p$ transitions contribute to the main photoabsorption structure around 45.60 nm while transitions from states of the ground electronic configuration contribute to the overall photoabsorption spectrum. So it can be concluded that there is evidence for photoabsortion from low lying excited state absorption in figure 5.15. Some of the most intense of these transitions are listed in Table 5.2.

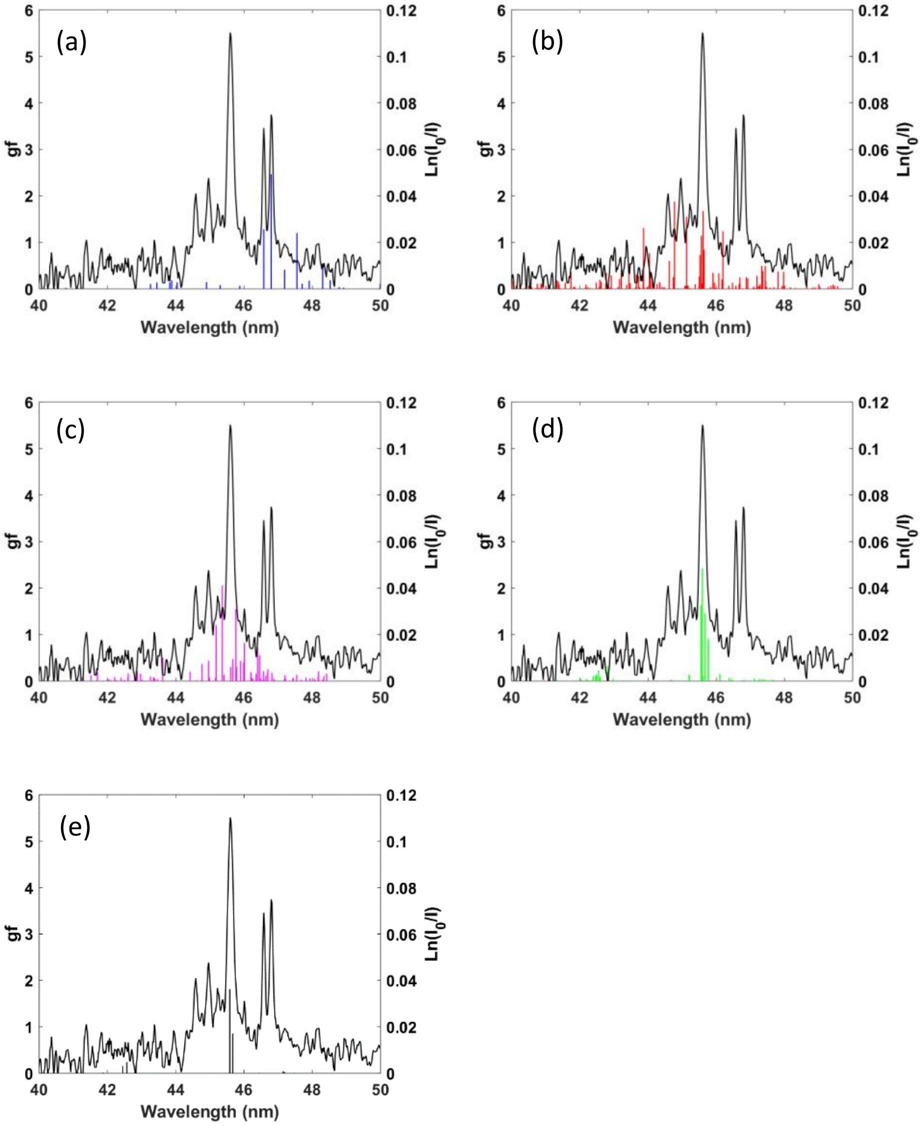

Figure 5. 15 Calculated gf values for Bi III transitions in the spectral region of interest. From top to bottom and from left to right: (a) $5d^{10}6s^26p \rightarrow 5d^96s^26p^2$, (b) $5d^{10}6s6p^2 \rightarrow 5d^96s6p^3$, (c) $5d^{10}6s^26d \rightarrow 5d^96s^26p6d$, (d) $5d^{10}6s^27p \rightarrow 5d^96s^26p7p$ and (e) $5d^{10}6s^27s \rightarrow 5d^96s^26p7s$ transitions. A comparison with the experimental spectrum (black line) reveals the contribution of each transition array.

In Fig. 5.16 we show the synthetic spectrum of Bi III which comprises the convolution of the computed gf values with a Gaussian function (0.045 nm FWHM), chosen to represent the spectrometer instrument function. As shown in Fig. 5.16, good agreement between the synthetic spectrum and the experimental data is achieved and the relative heights and positions of the peaks are well reproduced. It thus confirms that the measured spectrum contains evidence of excited states, along with photoabsorption from ions in the ground state.

Table 5. 2 Transitions corresponding to the most prominent features observed in the Bi III spectrum.

Transition $5d^{10}6s^26p \rightarrow 5d^96s^26p^2$	λ_{obs} (nm)	λ_{calc} (nm)	gf values
$^2P_{3/2} \rightarrow {}^2D_{5/2}$	46.80	46.79	2.47
$^2P_{3/2} \rightarrow {}^2P_{3/2}$	46.60	46.57	1.28
Transition $5d^{10}6s^27s \rightarrow 5d^96s^26p7s$	λ_{obs} (nm)	λ_{calc} (nm)	gf values
$^2S_{1/2} \rightarrow {}^2P_{3/2}$	45.62	45.58	1.82
$^2S_{1/2} \rightarrow {}^2P_{1/2}$	45.62	45.67	0.85
Transition $5d^{10}6s^26d \rightarrow 5d^96s^26p6d$	λ_{obs} (nm)	λ_{calc} (nm)	gf values
$^2D_{5/2} \rightarrow {}^2F_{7/2}$	45.25	45.36	2.06
$^2D_{5/2} \rightarrow {}^2P_{5/2}$	45.25	45.18	1.20
$^2D_{3/2} \rightarrow {}^2P_{5/2}$	45.62	45.76	1.55
Transition $5d^{10}6s6p^2 \rightarrow 5d^96s6p^3$	λ_{obs} (nm)	λ_{calc} (nm)	gf values
$^4P_{3/2} \rightarrow {}^4P_{5/2}$	44.96	45.13	1.55
$^4P_{3/2} \rightarrow {}^2D_{3/2}$	45.62	45.61	0.62
$^4P_{1/2} \rightarrow {}^2D_{3/2}$	44.60	44.63	0.61

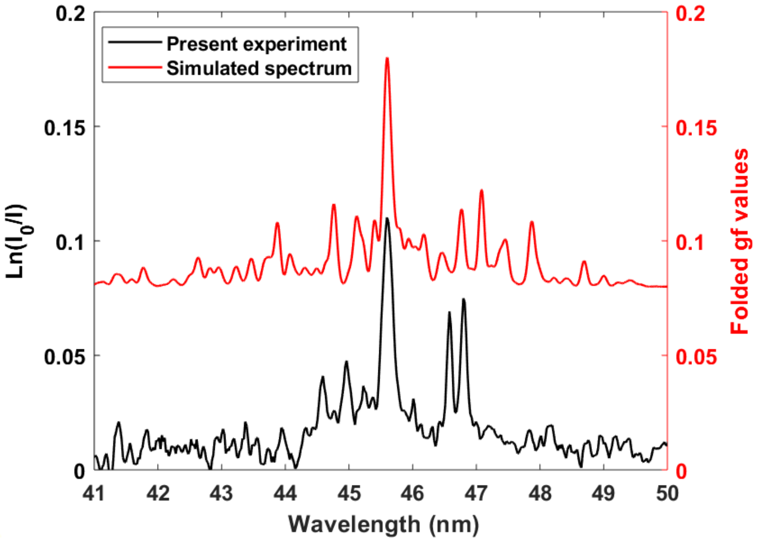

Figure 5. 16 A comparison between the synthetic spectrum (including $5d^{10}6s6p^2 \rightarrow 5d^96s6p^3$, $5d^{10}6s^26d \rightarrow 5d^96s^26p6d$, $5d^{10}6s^26p \rightarrow 5d^96s^26p^2$, $5d^{10}6s^27s \rightarrow 5d^96s^26p7s$ and $5d^{10}6s^27p \rightarrow 5d^96s^26p7p$ transitions) and the experimental spectrum of Bi III. The synthetic spectrum has been shifted upwards by a value of 0.08.

The experimental spectrum is a mixed contribution of transitions from both the ground state and low-lying excited states of Bi III. Specifically, the lines at 43.94 nm and 48.17 nm are exclusively due to transitions from low-lying excited states while the lines at 46.58 nm and 46.80 nm represent a blend of overlapping contributions from the ground and low-lying excited states. However, the dominant contributor to the observed spectrum comes from excited state photoabsorption.

In summary the VUV photoabsorption spectrum of Bi^{2+} has been measured in the 40 – 50 nm spectral range. Absorption from both the ground state and some low-lying excited states has been observed in the dual laser plasma experiment carried out. The VUV spectrum of Bi^{2+} showing absorption from the ground state only has been observed by Ryabstev et al. [62]. Comparing with the spectra observed here, it clear that the dual laser plasma setup favours strong excited state absorption.

The Pb II photoabsorption spectrum in the 45 – 70 nm region

Let us now turn our attention to the Pb II spectrum. In Fig. 5.17 we show the absorption spectrum of Pb II at an inter-laser delay of 150 ns and a distance of 0.55 mm away from the surface of the Pb target, in the spectral region ranging from 46 to 70 nm. As for Bi III, the same five electron configurations ($5d^{10}6s6p^2$, $5d^{10}6s^26d$, $5d^{10}6s^26p$, $5d^{10}6s^27s$ and $5d^{10}6s^27p$) were included in the Hartree Fock calculations. Furthermore, the Slater parameters were reduced by the same amount as for the Bi III case, i.e., the F_k integrals between equivalent and non-equivalent electrons, the exchange interaction integrals (G_k) and the configuration interaction integrals (R_k) were all reduced by 15%, while the spin-orbit parameters were reduced by 5%.

As can be seen in Fig. 5.17, the transitions originating from different ground and/or excited states result in broad features in the overall spectrum. The most intense of these transitions, by leading percentage are tabulated in Table 5.3. A number of transitions associated with the $5d^{10}6s^27s$ to $5d^96s^26p7s$ transition array contribute to the strong feature at 58.36 nm while transitions from the ground configuration $5d^{10}6s^26p$ to states associated with the excited $5d^96s^26p^2$ configuration add significant strength to the peaks at 59.46 nm and 59.90 nm. In addition, transitions from $5d^{10}6s^26d$ to $5d^96s^26p6d$ make a contribution across the spectral region under investigation, especially in the wavelength range extending from 58.7 to 59.7 nm.

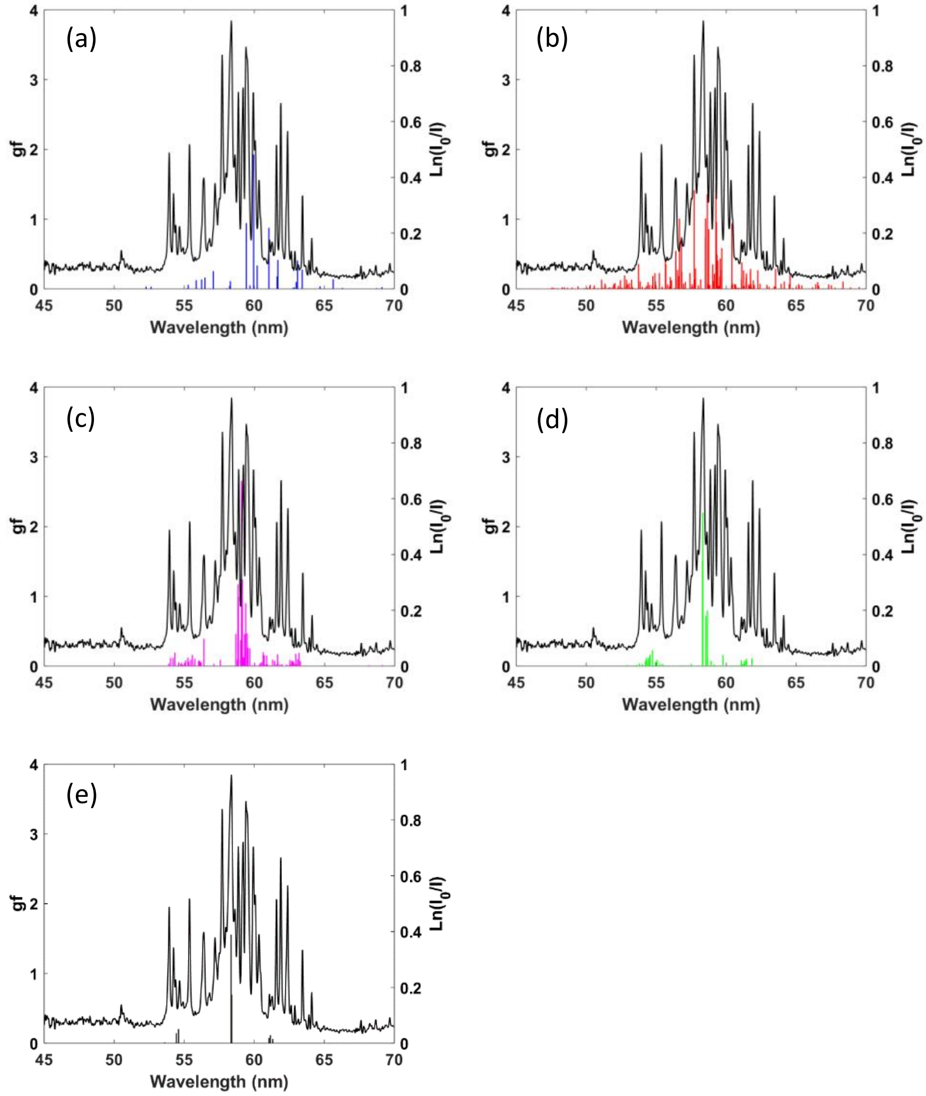

Figure 5. 17 Calculated gf values for each Pb II configuration involved in the current experiment. From top to bottom: (a) $5d^{10}6s^26p \rightarrow 5d^96s^26p^2$, (b) $5d^{10}6s6p^2 \rightarrow 5d^96s6p^3$, (c) $5d^{10}6s^26d \rightarrow 5d^96s^26p6d$, (d) $5d^{10}6s^27p \rightarrow 5d^96s^26p7p$ and (e) $5d^{10}6s^27s \rightarrow 5d^96s^26p7s$ transitions. A comparison with the experimental spectrum (black line) reveals the contribution of each transition array.

Using the computed gf values, stick diagrams of gf vs wavelength could be constructed and convolved with the spectrometer instrument function. The resulting synthetic spectrum, which is shown in Fig. 5.18, exhibited reasonable agreement with the experimental data. The spectrum is significantly more complex than for the Bi III case, thus the agreement between the calculation and the experiment in Fig. 5.18 is not as good as for Bi III. Similar to Bi III, there is strong evidence for the presence of excited states in the Pb II spectrum.

Table 5. 3 Transitions corresponding to the most prominent features observed in Pb II spectrum.

Transition $5d^{10}6s^26p \rightarrow 5d^96s^26p^2$	λ_{obs} (nm)	λ_{calc} (nm)	gf values
$^2P_{3/2} \rightarrow {}^2D_{5/2}$	59.93	59.94	1.93
$^2P_{3/2} \rightarrow {}^2P_{3/2}$	59.43	59.42	0.94
Transition $5d^{10}6s^27s \rightarrow 5d^96s^26p7s$	λ_{obs} (nm)	λ_{calc} (nm)	gf values
$^2S_{1/2} \rightarrow {}^2P_{3/2}$	58.36	58.35	1.56
Transition $5d^{10}6s^26d \rightarrow 5d^96s^26p6d$	λ_{obs} (nm)	λ_{calc} (nm)	gf values
$^2D_{5/2} \rightarrow {}^2F_{7/2}$	59.20	59.10	2.65
$^2D_{3/2} \rightarrow {}^2F_{5/2}$	59.20	59.16	1.24
$^2D_{1/2} \rightarrow {}^2D_{3/2}$	59.40	59.39	0.90
$^2D_{3/2} \rightarrow {}^2D_{3/2}$	58.89	58.88	0.99
$^2D_{5/2} \rightarrow {}^2D_{5/2}$	58.89	58.84	1.17
Transition $5d^{10}6s6p^2 \rightarrow 5d^96s6p^3$	λ_{obs} (nm)	λ_{calc} (nm)	gf values
$^2P_{3/2} \rightarrow {}^2D_{5/2}$	57.71	57.70	1.42
$^4P_{5/2} \rightarrow {}^4D_{7/2}$	59.20	59.27	1.50
$^2D_{3/2} \rightarrow {}^4G_{5/2}$	60.35	60.41	0.94
$^4P_{3/2} \rightarrow {}^4P_{5/2}$	58.65	58.63	1.36

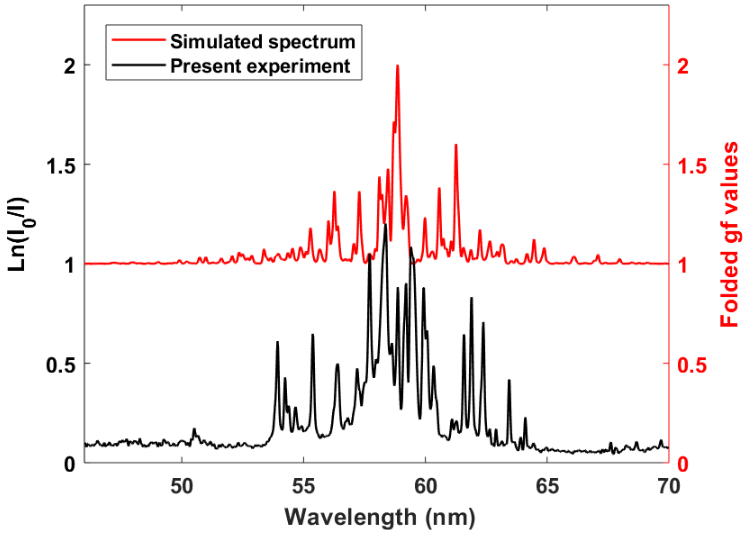

Figure 5. 18 A comparison between the synthetic spectrum (shifted by 1.0, including $5d^{10}6s6p^2 \rightarrow 5d^96s6p^3$, $5d^{10}6s^26d \rightarrow 5d^96s^26p6d$, $5d^{10}6s^26p \rightarrow 5d^96s^26p^2$, $5d^{10}6s^27s \rightarrow 5d^96s^26p7s$ and $5d^{10}6s^27p \rightarrow 5d^96s^26p7p$) and the experimental spectrum of Pb II.

5.5 Summary

The VUV photoabsorption spectra of laser-induced bismuth and lead plasmas have been obtained using the dual laser plasma photoabsorption technique. The Bi II, Bi III and Pb II spectra were explored in the 37-70 nm wavelength region, where the 5d→6p transitions are predominant. Evidence of the presence of low-lying excited states was provided with the aid of the Cowan suite of atomic structure codes for them. The synthesized spectra for Bi II, Bi III and Pb II reproduced the overall shapes and some of the discrete features of the experimental spectra.

References

[1] M. Larsson, W. D. Geppert and G. Nyman, Ion chemistry in space. *Rep. Prog. Phys.* **75,** 066901 (2012)

[2] J. A. Cardelli, S. R. Federman, D. L. Lambert and C. E. Theodosiou, Ultraviolet transitions of low condensation temperature heavy elements and new data for interstellar arsenic, selenium, tellurium, and lead. *Astrophys. J.* **416,** L41 (1993)

[3] D. S. Leckrone, S. G. Johansson, G. M. Wahlgren, T. Brage and C. R. Proffitt, Atomic data requirements for the analysis of chemically peculiar spectra. *Highlights Astron.* **11,** 650 (1998)

[4] G. M. Wahlgren, T. Brage, J. C. Brandt, J. Fleming, S. Johansson, D. S. Leckrone, C. R. Proffitt, J. Reader and C. J. Sansonetti, The bismuth abundance in the HgMn stars chi Lupi and HR 7775 and improved atomic data for selected transitions of BiI, BiII, and BiIII. *Astrophys. J.* **551,** 520 (2001)

[5] F. P. Keenan and S. J. Rose, Spectroscopy of astrophysical plasmas in the laboratory, *Astron. Geophys.* **45,** 6.18 (2004)

[6] M. Finkenthal, S. Lippmann, L. K. Huang, A. Zwicker, H. W. Moos, W. H. Goldstein and A. L. Osterheld, O-shell emission of heavy atoms in an optically thin tokamak plasma. *Phys. Rev. A* **45,** 5846 (1992)

[7] C. Suzuki, F. Koike F, I. Murakami, N. Tamura, S. Sudo, H. A. Sakaue, N. Nakamura, S. Morita, M. Goto, D. Kato, T. Nakano, T. Higashiguchi, C. S. Harte and G. O'Sullivan, EUV spectroscopy of highly charged high Z ions in the Large Helical Device plasmas. *Phys. Scr.* **89,** 114009 (2014)

[8] P. Beiersdorfer, Laboratory X-Ray Astrophysics. *Annu. Rev. Astron. Astrophys.* **41,** 343 (2003)

[9] S. Haessler, V. Strelkov, L. B. Elouga Bom, M. Khokhlova, O. Gobert, J-F. Hergott, F. Lepetit, M. Perdrix, T. Ozaki and P. Salières, Phase distortions of attosecond pulses produced by resonance-enhanced high harmonic generation. *New J. Phys* **15**, 013051 (2013)

[10] R. A. Ganeev, L. B. Elouga Bom, and T. Ozaki, Time-resolved spectroscopy of plasma plumes: A versatile approach for optimization of high-order harmonic generation in laser plasma. *Phys. Plasmas* **18**, 083101 (2011)

[11] A. Müller, Precision studies of deep-inner-shell photoabsorption by atomic ions. *Phys. Scr.* **90**, 054004 (2015)

[12] A. Müller, S. Schippers, J. Hellhund, A. L. D. Kilcoyne, R. A. Phaneuf and B. M. McLaughlin, Photoionization of tungsten ions: experiment and theory for W^{4+}. *J. Phys. B: At. Mol. Opt. Phys.* **50**, 085007 (2017)

[13] J. B. West, Photoionization of atomic ions. *J. Phys. B At. Mol. Opt. Phys.* **34** R45 (2001)

[14] J. T. Costello, J.-P. Mosnier, E. T. Kennedy, P. K. Carroll, G. O'Sullivan, XUV absorption spectroscopy with laser-produced plasmas: a review. *Phys. Scr.* **34**, 77 (1991)

[15] R. D'Arcy, J. T. Costello, C. McGuinness and G. O'Sullivan, Discrete structure in the 4d photoabsorption spectrum of antimony and its ions. *J. Phys. B At. Mol. Opt. Phys.* **32,** 4859 (1999)

[16] I. C. Lyon, B. Peart, J. B. West and K. Dolder, Measurements of absolute cross sections for the photoionisation of Ba^+ ions. *J. Phys. B At. Mol. Phys.* **19,** 4137 (1986)

[17] I. C. Lyon, B. Peart, K. Dolder and J. B. West, Measurements of absolute photoionisation cross sections of Ca^+ ions. *J. Phys. B At. Mol. Phys.* **20** 1471 (1987)

[18] M. F. Gharaibeh, J. M. Bizau, D. Cubaynes, S. Guilbaud, N. El Hassan, M. M. Al Shorman, C. Miron, C. Nicolas, E. Robert, C. Blancard and B. M. McLaughlin, K-shell photoionization of singly ionized atomic nitrogen: experiment and theory. *J. Phys. B At. Mol. Opt. Phys.* **44,** 175208 (2011)

[19] A. M. Covington, A. Aguilar, I. R. Covington, M. F. Gharaibeh, G. Hinojosa, C. A. Shirley, R. A. Phaneuf, I. Álvarez, C. Cisneros, I. Dominguez-Lopez, M. M. Sant'Anna, A. S. Schlachter, B. M. McLaughlin, and A. Dalgarno, Photoionization of Ne^+ using synchrotron radiation. *Phys. Rev. A* **66,** 062710 (2002)

[20] S. Schippers, S. Ricz, T. Buhr, J. Hellhund, A. Müller, S. Klumpp, M. Martins, R. Flesch, E. Rühl, J. Lower, T. Jahnke, D. Metz, L. Ph H. Schmidt, R. Dörner, J. Ullrich and A. Wolf, Photon-ion spectrometer PIPE at the Variable Polarization XUV Beamline of PETRA III. *J. Phys. Conf. Ser.* **388,** 142016 (2011)

[21] H. S. Chakraborty, A. Gray, J. T. Costello, P. C. Deshmukh, G. N. Haque, E. T. Kennedy, S. T. Manson and J-P. Mosnier, Anomalous Behavior of the Near-Threshold Photoionization Cross Section of the Neon Isoelectronic Sequence: A Combined Experimental and Theoretical Study. *Phys. Rev. Lett.* **83,** 2151 (1999)

[22] P. van Kampen, G. O'Sullivan, V. K. Ivanov, A. N. Ipatov, J. T. Costello, and E. T. Kennedy, Dramatic Changes in the 3s Autoionization Process at the Beginning of the Ar I Sequence. *Phys. Rev. Lett.* **78,** 3082 (1997)

[23] E. Jannitti, P. Nicolosi, G. Tondello, Absorption spectra from 1s inner-shell electron of ionized and neutral carbon. *Phys. Scr.* **41**, 458 (1990)

[24] P. Nicolosi and P. Villoresi, Experimental measurement of the CII L-shell photoabsorption spectrum. *Phys. Rev. A* **58**, 4985 (1998)

[25] P. Recanatini, P. Nicolosi, P. Villoresi, ^2P and ^4P CII photoabsorption spectra. *Phys. Rev. A* **64**, 012509 (2001)

[26] P. Jaegle, G. Missoni, and P. Dhez, Study of the Absorption of Ultrasoft X Rays by Bismuth and Lead Using the Orbit Radiation of the Frascati Synchrotron. *Phys. Rev. Lett.* **19,** 57 (1967)

[27] J. P. Connerade, W. R. S. Garton, M. W. D. Mansfield and M. A. P. Martin, Interchannel interactions and series quenching in the 5d and 6s spectra of Pb I. *Proc. Roy. Soc. London Ser. A* **357**, 499 (1977)

[28] J. P. Connerade and M. A. Baig, On the sp2 configuration in the Ga I, In I, and Tl I isoelectronic sequences. *J. Phys. B At. Mol. Phys.* **14,** L141 (1981)

[29] D. M. P. Holland and K. Codling, The double ionisation of barium between 20 and 25 eV. *J. Phys. B At. Mol. Phys.* **13,** L745 (1980)

[30] R. Assous, Autoionized Lines in Arc Spectra of Lead and Bismuth. *J. Opt. Soc. Am.* **62,** 544 (1972)

[31] M. F. Crawford, A. B. McLay and A. M. Crooker, The spectrum of trebly-ionized lead, Pb IV. *Proc. R. Soc. London. Ser. A - Math. Phys. Sci.* **158,** 455 (1937)

[32] G. K. Schoepfle, The Spectra of Lead IV and Bismuth V. *Phys. Rev.* **47,** 232 (1935)

[33] C. Banahan, C. McGuinness, J. T. Costello, D. Kilbane, J-P. Mosnier, E. T. Kennedy, G. O'Sullivan and P. van Kampen, The 5d photoabsorption spectra of Pb III and Bi IV. *J. Phys. B At. Mol. Opt. Phys.* **41,** 2005001 (2008)

[34] A. Zangwill and D. A. Liberman, A nonrelativistic program for optical response in atoms using a time dependent local density approximation. *Comput. Phys. Commun.* **32,** 63 (1984)

[35] D. A. Liberman and A. Zangwill, A relativistic program for optical response in atoms using a time dependent local density approximation. *Comput. Phys. Commun.* **32,** 75 (1984)

[36] J. T. Costello, E. T. Kennedy, J-P Mosnier, M. H. Sayyad and C. McGuiness, Extreme-UV photoabsorption spectrum of a laser-produced silicon plasma: evidence for metastable Si^+ ions*. J. Phys. B: At. Mol. Opt. Phys.* **31**, L547 (1998)

[37] J. P. Mosnier, J. T. Costello, E. T. Kennedy, L. Kiernan and M. H. Sayyad, Even-parity autoionizing states in the extreme-ultraviolet photoabsorption spectra of Mg, Al^+, and Si^{2+}. *Phys. Rev. A* **49,** 755 (1994)

[38] J. Brilly, E. T. Kennedy and J. P. Mosnier, 2p photoabsorption spectra of valence excited configurations in Al^{2+} and Si^{3+} observed in a dual laser produced plasma experiment. *Phys. Scr.* **41,** 30 (1990)

[39] C. McGuinness, M. Martins, P. Wernet, B. F. Sonntag, P. Van Kampen, J. P. Mosnier, E. T. Kennedy and J. T. Costello, Metastable state contributions to the

measured 3p photoabsorption spectrum of Cr^+ ions in a laser-produced plasma. *J. Phys. B At. Mol. Opt. Phys.* **32,** L583 (1999)

[40] A. M. Covington, A. Aguilar, I. R. Covington, G. Hinojosa, C. A. Shirley, R. A. Phaneuf, I. Álvarez, C. Cisneros, I. Dominguez-Lopez, M. M. Sant'Anna, A. S. Schlachter, C. P. Ballance and B. M. McLaughlin, Valence-shell photoionization of the Cℓ-like ion Ar^+: Experiment and theory. *Phys. Rev. A* **84,** 013413 (2011)

[41] A. Müller, E. Lindroth, S. Bari, A. Borovik Jr., P.-M. Hillenbrand, K. Holste, P. Indelicato, A. L. D. Kilcoyne, S. Klumpp, M. Martins, J. Viefhaus, P. Wilhelm, S. Schippers, Photoionization of metastable heliumlike C4+(1s 2s 3S1) ions: Precision study of intermediate doubly excited states. *Phys. Rev. A* **98,** 033416 (2018)

[42] H. Kjeldsen, J. E. Hansen, F. Folkmann, H. Knudsen, J. B. West and T. Andersen, The absolute cross section for L-shell photoionization of C^+ ions from threshold to 105 eV. *Astrophys. J. Suppl. Ser.* **524,** L143 (2001)

[43] H. Kjeldsen, F. Folkmann, B. Kristensen, J. B. West and J. E. Hansen, Absolute cross section for photoionization of Mn+ in the 3p region. *J. Phys. B At. Mol. Opt. Phys.* **37,** 1321 (2004)

[44] J. C. McLennan, A. B. McLay and M. F. Crawford, Spark spectra of bismuth, Bi II and Bi III. Evidence of hyperfine structure. *Proc. R. Soc. Lond. A* **129,** 579 (1930)

[45] M. F. Crawford and A. B. McLay, Spark spectra of bismuth, Bi III and Bi II. *Proc. R. Soc. Lond. A* **143,** 540 (1934)

[46] R. A. Fisher and S. Goudsmit, Hyperfine structure in ionized Bi. *Phys. Rev.* **37,** 1057 (1931)

[47] C. Moore, Atomic Energy Levels vol III (Washington, DC: National Bureau of Standards) 1958

[48] Y. N. Joshi and R. P. Srivastava, Absorption spectrum of bismuth in the region 2300–1250 Å, using the flash pyrolysis technique. *Can. J. Phys.* **56,** 1157 (1978)

[49] S. Suzer, S. T. Lee and D. A. Shirley, 304 Å photoelectron spectra of atomic Hg, Tl, and Pb 5d levels; interaction of open shells. *J. Chem. Phys.* **65,** 411 (1976)

[50] W. A. Young, M. Y. Mriza and W. W. Duley, Three-photon excitation of Rydberg series in lead and bismuth. *J. Phys. B: At. Mol. Phys.* **13,** 3175 (1980)

[51] M. Mazzoni, Y. N. Joshi, A. Nencioni, T. Grisendi and W. H. Parkinson, Photoabsorption spectrum of atomic bismuth in the vacuum ultraviolet region. *J. Phys. B: At. Mol. Phys.* **20,** 2193 (1987)

[52] R. K. Yoo, B. Ruscic and J. Berkowitz, Photoionization of atomic bismuth. *J. Phys. B: At. Mol. Opt. Phys.* **28,** 1743 (1995)

[53] Y. N. Joshi and M. Mazzoni, The $6s^26p^2\ ^3P_0$-$6S^26pnd\ ^3D_1$, series in photoabsorption of BI II. *Phys. Rev. A* **118,** 237 (1986)

[54] M. Andrzejewska, F. G. Meijer and E. Stachowska, On the level system of Bi II. *J. Phys. B: At. Mol. Opt. Phys.* **46**, 205003 (2013)

[55] G. M. Wahlgren, T. Brage, J. C. Brandt, J. Fleming, S. Johansson, D. S. Leckrone, C. R. Proffitt, J. Reader and C. J. Sansonetti, The bismuth abundance in the Hg Mn stars χ Lupi and HR 7775 and improved atomic data for selected transitions of Bi I, Bi II, and Bi III*. *ApJ,* **551**, 520 (2001)

[56] W. R. S. Garton and M. Wilson, Schumann region absorption spectrum of lead vapour. *Proc. Phys. Soc.* **87**, 841 (1966)

[57] C. M. Brown, S. G. Tilford and M. L. Ginter, Absorption spectrum of Pb I between 1350 and 2041 Å. *J. Opt. Soc. Am.* **67**, 1240 (1977)

[58] L. T. Earls and R. A. Sawyer, The classification of the first spark spectrum of lead: Pb II. *Phys. Rev.* **47**, 115 (1935)

[59] S. J. Smith, A note on the spectra of doubly and trebly ionized lead. *Phys. Rev.* **36**, 1 (1930)

[60] A. S. Rao and A. L. Narayan, Über das Zweite Funkenspektrum des Bleies. *Z. Phys.* **59**, 687 (1930)

[61] R. D. Cowan R D, The Theory of Atomic Structure and Spectra. University of California Press (1982)

[62] A. N. Ryabtsev, S. S. Churilov, and Y. N. Joshi, Analysis of Transitions from Autoionization States of the Bi III, Bi IV, and Bi V Ions. *Opt. Spectrosc*. **88,** 316 (2000)

Chapter 6 Two Colour Resonant Laser Photoionization of Mo in a Hollow Cathode Lamp

6.1 Introduction

The intensity and physical composition of the radioactive ion beams produced is strongly dependent on the type of source used to ionize the atoms of interest [1,2]. Due to the high selectivity of the resonant ionization laser ion source (RILIS) technique, a category of AVLIS [3], many different ISOL facilities adopted and implemented laser ion sources based on resonant excitation of atomic transitions by tunable lasers. In fact, resonant laser ionization is a universal method, applicable to many elements in the periodic table for isotope selective ion production. In principle, RILIS can be used for ionization of almost all elements and an important aspect of its future development is the extension of its range of element applicability by the addition of new ionization (two or multi-colour) schemes. Ions of a chosen element/isotope are ionized via stepwise atomic resonant excitations using, typically, two or three laser beams tuned to specific transition energies of the element of interest [5]. In this way the resonant photo-ionization process can provide very high isotopic selectivity [6].

In terms of ionization efficiency, several off-line laboratories are working to develop the best stepwise resonant ionization paths for specific species, taking into account the available wavelengths from tunable Ti-Sapphire or dye lasers. Recently a new laser laboratory, aiming to study laser resonant ionization techniques, was established in Legnaro [1,2]. As noted in chapter 4, the laboratory has two dye lasers, pumped by two Nd:YAG lasers, operated at a pulse repetition rate of 10 Hz. As a spectroscopic tool to investigate ionization paths, hollow cathode lamps, loaded with the element of interest, are used. They offer two diagnostic indicators, optogalvanic slow and fast signals [7] to check, respectively, laser wavelength tuning and resonant ionization. This technique can be exploited to check already known transition wavelengths, or it can be used to find new absorption lines or even auto-ionizing levels. In this work, we used a molybdenum hollow cathode lamp. The element was chosen due to its increasing interest for the RIB scientific community.

6.2 Optogalvanic Signals

The optogalvanic effect (OGE) arises from the interaction of resonant radiation with atoms in a discharge. This interaction produces changes in the electrical properties of the discharge, which can be in turn observed as a variation in the gas discharge conductivity. Green, Keller, Luther et al. [8] used this effect for the first time in spectroscopic applications in 1976. Lawler [9] found that the OGE can be considered proportional to the number of photons absorbed because the observed perturbation in the discharge properties (e.g., impedance) due to the laser resonant radiation is small. Hence the OGE technique is considered to be a good alternative to traditional emission or absorption optical spectroscopy, particularly for the detection of weak transitions. Highly refractive elements, like molybdenum, can also be investigated using this method in hollow cathode discharges in which the materials are vaporized layer by layer by the ion sputtering process.

There are two mechanisms giving rise to the OGE in a hollow cathode discharge.

First mechanism: the absorption of laser radiation in the discharge leads to a change in the steady-state population of bound atomic or molecular levels. Since different levels will have different ionization cross-sections or ionization probabilities, a perturbation of the steady-state population distribution results in a net change in the discharge current (or an equivalent change in the discharge impedance). The electric signal detected is designated the slow signal: it is usually a negative going voltage and has a duration of a few microseconds. The results for slow optogalvanic signals will be discussed in section 6.3.

Second mechanism: direct ionization during laser pulse. This effect produces a fast electrical signal. It was found that this fast signal follows the laser pulse temporal behaviour and so it exists on the nanosecond timescale.

The fast and the slow OGE signals are used to monitor and tune the appropriate wavelengths of the laser system for the excitation steps in the resonant photoionization scheme. The results for fast optogalvanic signals will be discussed in section 6.4.

After aligning the dye laser output beams with the Heraues-Noblelight Hollow-Cathode Lamp (50 mm diameter, Model No. 5QNMO), slow and fast optogalvanic signals were successfully observed and characterized. The signals were displayed on a digital oscilloscope (Tektronix Model No. TDS540) and maximized in amplitude by adjusting laser and lamp parameters. Then, the laser wavelengths were varied to verify the frequency tunability of the optogalvanic signals, which are related to the excitation of resonant transitions and to subsequent ionization of the sputtered Molybdenum atoms. Subsequently, several automatic scans were performed to identify the wavelength values corresponding to the maximum detected signals. Finally, scanning again the wavelengths around the identified central values, the linewidths of the chosen transitions were estimated.

The wavelength scans as well as the acquisition and processing of the corresponding detected optogalvanic signals were controlled by two MATLAB® programs run on one of the laboratory's personal computers. One program took care of the slow signals while the other processed the fast signals. The two programs are very similar and simply allow the user to manage both slow signal and fast signal characterization respectively. In particular, the programs can scan the wavelength of one laser at a time while keeping the wavelength of the other laser at a fixed value. They also allow one to set the central laser wavelength and half window width, in nanometers, for the scan. After the scan is finished, the grating in the scanning laser is brought back to the position corresponding to the central wavelength of the scan in the program.

The scan can be performed either with or without signal acquisition. The digital oscilloscope is triggered by the output pulses from the TDL50 pump laser using a signal that is provided by a monitor photodiode in the laser cavity. The oscilloscope is initialized to work in the fast frame mode while acquiring data. After the laser trigger signal, the oscilloscope acquires 250 frames and saves them into its memory. While acquiring the next 250 frames, the previously saved ones are transferred to the PC via a dedicated serial port. The oscilloscope continues working in this mode until the scan has ended. The 250 frame sequences are then organized by the program into a proper data structure for subsequent processing and graphical presentation.

The detected minimum of the slow optogalvanic (ion) signal or the detected maximum of the fast (electron) signal are plotted versus the scanned laser wavelength. The data are fitted to a 21 adjacent points average curve from which the estimated full width at half maximum (FWHM) and the centre wavelength, corresponding to the curve peak, are extracted. Each OGS program also creates a new directory on the PC and saves the processed data and graphs.

6.3 Slow Optogalvanic Signal

To obtain the slow optogalvanic signal, the laser beam from the TDL50 dye laser was used to excite the molybdenum vapour in the hollow cathode lamp while the FL2002 laser was off. The laser beam was focused by a lens and converged to an area of ca. 1mm^2 in the HCL. While moving the spot position on the cathode by tilting the final mirror along the beam path and by controlling the translation stage on which the lamp was mounted, a waveform resembling the slow optogalvanic signal was observed on the oscilloscope display. The first check was to manually scan the wavelength in increments of ca. 0.1 nm around the 379.933 nm central laser wavelength to see if the signal depended on the laser tuning, or not. An important point in this regard is to be sure that the UV power remains constant during the wavelength scan. If this is the case, it means in fact that the signal decreases in amplitude because the laser beam is detuned and not because the efficiency of the SFG process producing the UV laser pulse has dropped.

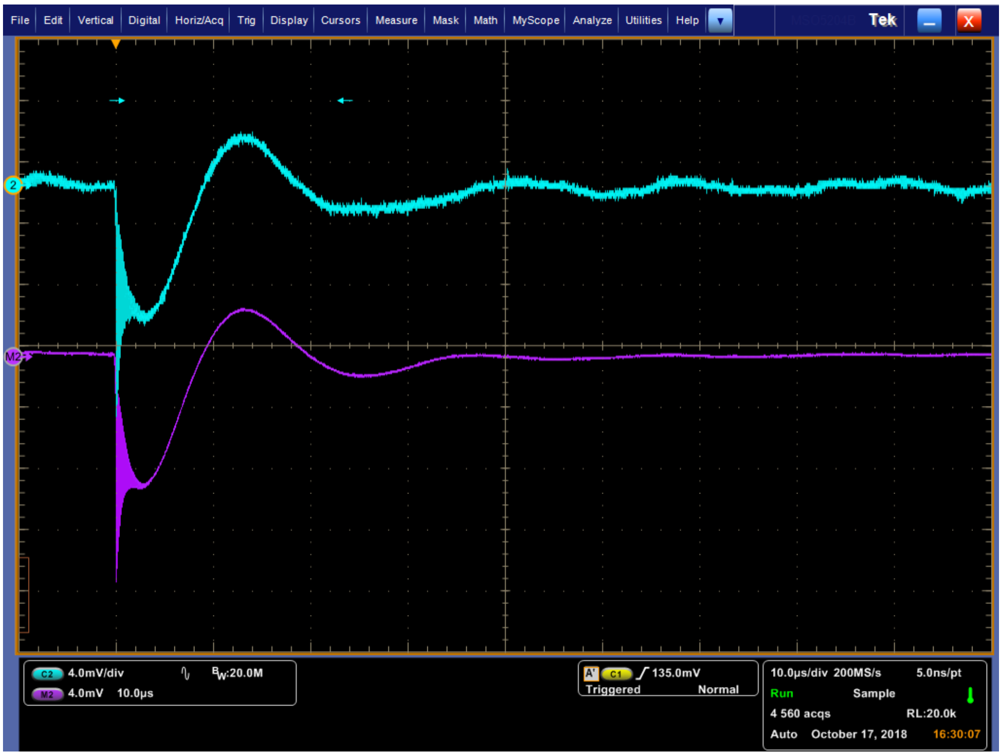

C2 4.0mV/div BW:20.0M
M2 4.0mV 10.0µs
C1 135.0mV
10.0µs/div 200MS/s 5.0ns/pt
4 560 acqs RL:20.0k
Auto October 17, 2018 16:30:07

Figure 6. 1 Slow optogalvanic signal obtained by scanning the TDL50 dye laser. The dip shows the voltage in the hollow cathode lamp. The second dye laser (FL2002) was off. The signal in green is the real-time signal, whereas the signal in purple is the average of 250 single shot frames.

After the tunability of the signal has been checked, the position of the focal spot and the emission wavelength of the dye laser were optimized to maximize the signal amplitude. A pinhole was also added in front of the lens to regulate the laser power and spot size so that the average laser power, measured in front of the lamp entrance, was reduced to 30 µW or 3 µJ per pulse at 379.933 nm. Another parameter that can be varied is the lamp supply current, which was gradually increased to 18 mA. It was found that the higher the supply current the larger the amplitude and the faster the relaxation time of the detected signal.

Figure 6.1 shows the slow optogalvanic signal on the oscilloscope screen. The signal in green is the real-time signal, whereas the signal in purple is its averaged version, obtained by computing the mean of 250 single frames. The time scale is 10 µs per division and the vertical scales are 4 mV/div. It can be noticed that the signal is largely extinguished after 30-35 µs, which we take as the characteristic relaxation time of slow optogalvanic signals.

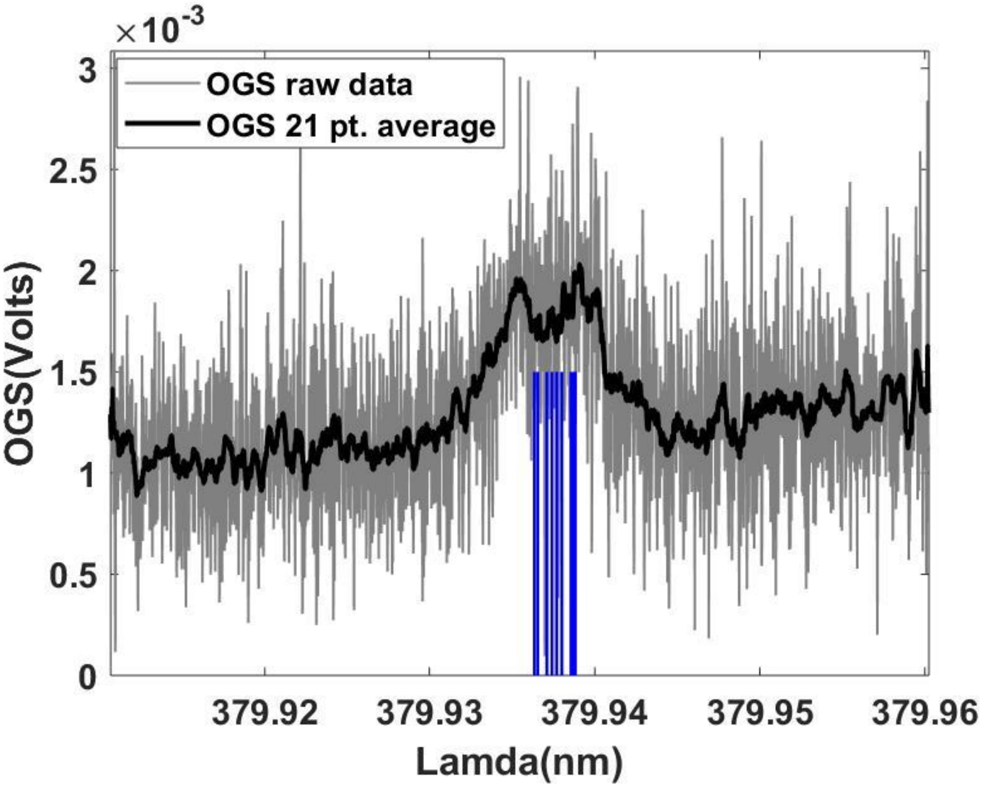

Figure 6. 2 The change of voltage versus the laser wavelength. This OGE trace was obtained by tuning the TDL50 dye laser only. The second laser (FL2002) was off. The plot is fitted to a 21 adjacent points average. The OGE curve peaks at 379.938 nm.

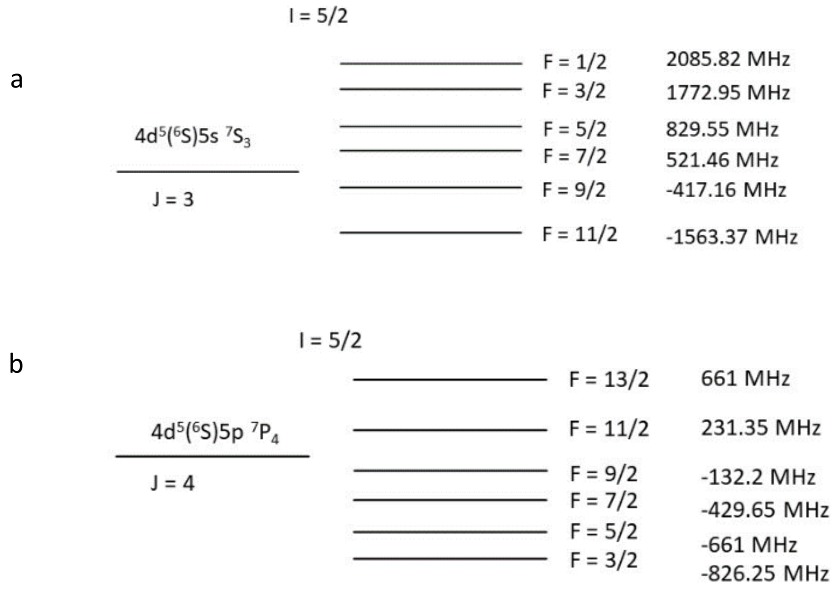

Figure 6. 3 (a) Hyperfine structure of the ground state (4d^5(^{6}S)5s ^{7}S$_3$) of Mo. (b) Hyperfine structure of the exited state (4d^5(^{6}S)5p ^{7}P$_4$) of Mo.

The next step was to run the MATLAB® program to automatically scan the wavelength of the TDL50 dye laser while acquiring data from the oscilloscope. The scanning window was set to 0.05 nm around the central wavelength of 379.933 nm. The resulting spectral scan is shown in Fig. 6.2. The vertical axis shows the minimum amplitude in volts of the signal acquired during the wavelength scan, while the horizontal axis shows the corresponding wavelength in nanometers. For each wavelength point the voltage chosen corresponds to the detected minimum of the slow optogalvanic signal. The wavelength scale is obtained from the initial and final wavelengths of the scan and from the scanning step. The wavelength reading is provided by the dye laser control electronics and converted by the MATLAB® program to the wavelength generated after the sum frequency generation (SFG) process used to generate the UV output. By inspection, the full width at half maximum (FWHM) of the resonance in Fig. 6.2, which has been smoothed by a 21 adjacent point average, is ~0.01 nm and the laser wavelength corresponding to the profile peak is 379.938 nm. This wavelength, given by the dye laser programme, is uncalibrated. After each such scan the centre wavelength was remeasured using a wavemeter after the experiment to be 379.933 nm. The hyperfine structure of the ground ($4d^5(^6S)5s\ ^7S_3$) and excited ($4d^5(^6S)5p\ ^7P_4$) states of Mo [10, 11] are shown in Fig. 6.3 and the splittings of the associated hyperfine levels are given. The blue sticks in Fig. 6.2 represent the corresponding wavelengths for transitions between these ground and excited hyperfine states of atomic Mo. The small features on the curve are believed to arise from such transitions, albeit the signal is too noisy to make any direct comparisons.

The signal is clearly very weak with a voltage difference of only ca. 1 mV between the peak value of the optogalvanic signal and the baseline voltage. As the excited state created lies only about 3.26 eV above the ground state, it is quite far from the ionization threshold, about 3.8 eV or so. Hence ionization will rely heavily on collisions between Mo atoms in excited states. However, one single collision between a pair of Mo atoms, each in the $4d^5(^6S)5p\ ^7P_4$ state, would not suffice to ionize a Mo atom and hence more than a single binary collision is needed per Mo ionization event. The slow signal was generated a few microseconds after the laser was fired and the timescale of multi-photon absorption should be in a few nanoseconds, so the slow signal is mainly due to the collisions between the excited states of Mo atoms. It should be noted that although multiphoton ionization is possible here, and is a key driver of fast optogalvanic signals, it is not a main contributor to the slow signals.

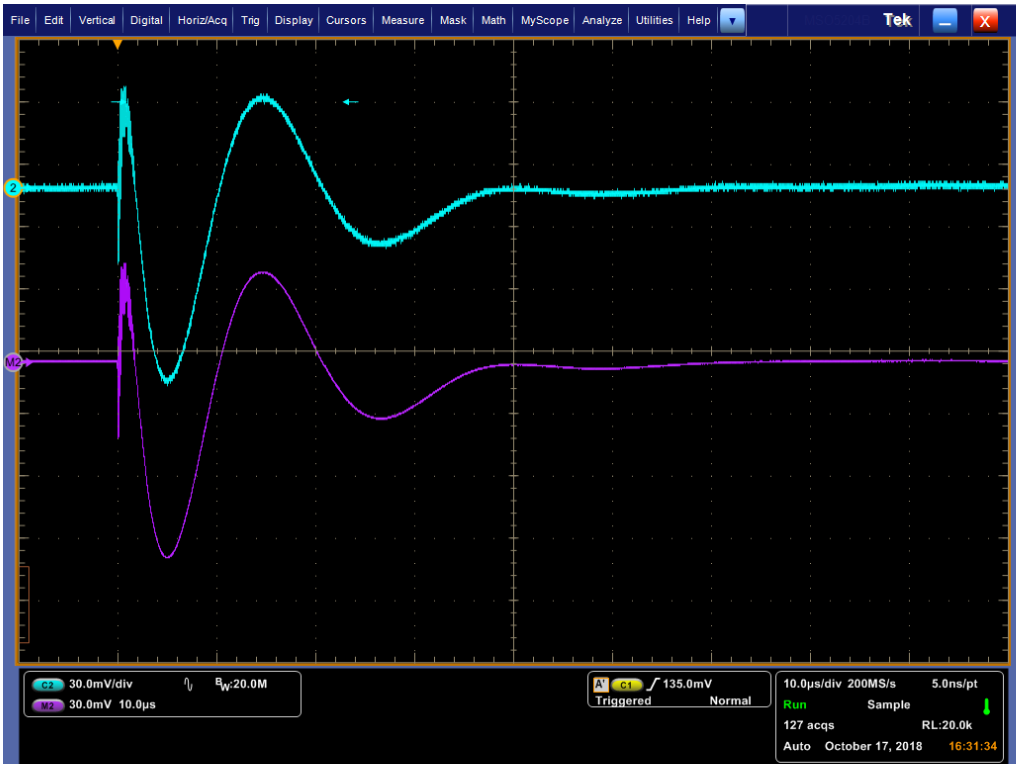

C2 30.0mV/div BW:20.0M
M2 30.0mV 10.0μs
135.0mV
Triggered Normal
10.0μs/div 200MS/s 5.0ns/pt
Run Sample
127 acqs RL:20.0k
Auto October 17, 2018 16:31:34

Figure 6. 4 Slow optogalvanic signal with both TDL50 and FL2002 lasers on. The green trace is the real-time slow signal while the signal in purple is its averaged version.

Fig. 6.4 shows the slow optogalvanic signal with both the TDL50 laser and FL2002 laser on. The green trace is the real-time slow signal while the signal in purple is its averaged version. The time scale is 10 μs per division and the vertical scales are 30 mV/div for both. One can see from the picture that the signal is much stronger than that obtained with the TDL50 laser only.

Fig. 6.5 was obtained by running the MATLAB® program to automatically scan the wavelength of the TDL50 dye laser while keeping the FL2002 laser wavelength fixed at 415.90 nm. Hence, in this case, the laser is scanned across the first excited state ($4d^5(^6S)5p\ ^7P_4$) while the second laser is kept resonant with the second step excited state ($4d^5(^6S)6d\ ^7D_5$) of Mo atoms. The scanning window was ca. 0.05 nm around the (uncalibrated) central wavelength of 378.846 nm. By inspection, the

FWHM of the main peak, following a 21 adjacent point averaging procedure to improve the signal to noise ratio, was ~0.01 nm. It is clear that the optogalvanic signal is up to 100 times larger in this case than in Fig. 6.2. The two-step resonant ionization process is therefore significantly more efficient at selectively ionizing an isotope of interest, one of the key goals of the SPES project. The result exhibits two important features of this particular colour AVLIS technique, ionization selectivity and efficiency.

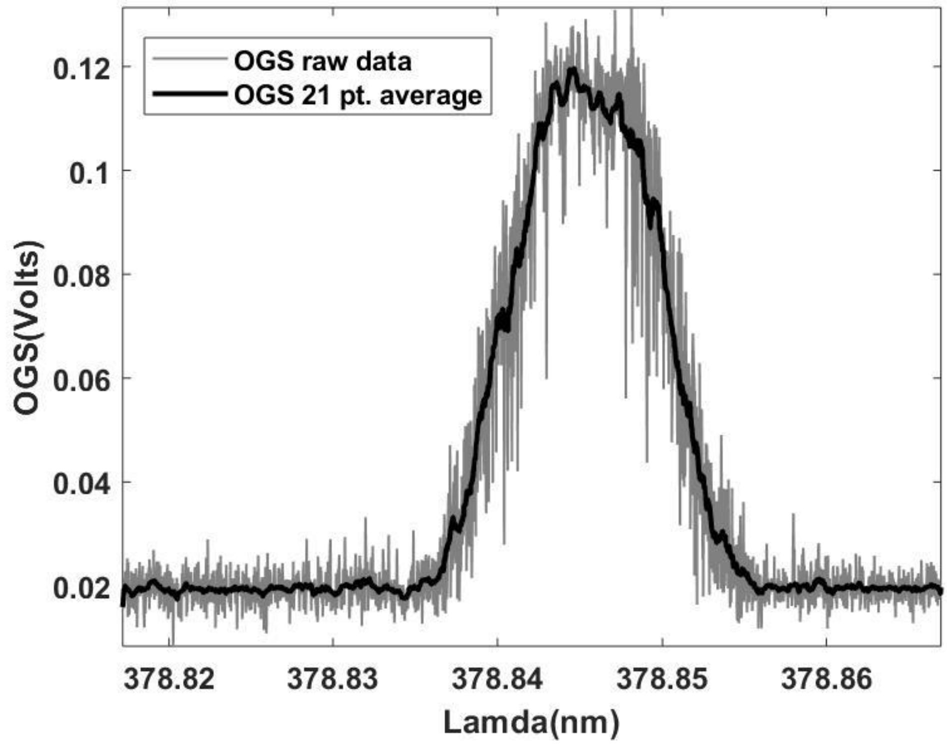

Figure 6. 5 Slow optogalvanic signal with both dye lasers on – scanning the TDL50 laser. The FL2002 laser wavelength fixed at 415.90 nm.

For Fig. 6.6, the TDL50 laser wavelength was fixed at 379.933 nm, resonant with the first step (4d^5(^{6}S)5p $^7P_4$) state while scanning the FL2002 laser over a window of ca. 0.14 nm at a central wavelength of 415.90 nm, i.e., scanning across the 4d^5(^{6}S)6d $^7D_5$ state. The uncalibrated central wavelength returned by the dye laser programme was 415.79 nm. By inspection, the FWHM of the main peak, following a 21 adjacent point averaging procedure to improve the signal to noise ratio, was ~0.02 nm, or approximately twice the width of the first step transition. The optogalvanic signal is comparable in height with that shown in Fig. 6.5, indicating comparable ionization efficiency. Also, since the second step resonance is twice the width of the first step resonance, it is also less sensitive to laser wavelength jitter, which might be an advantage in practice.

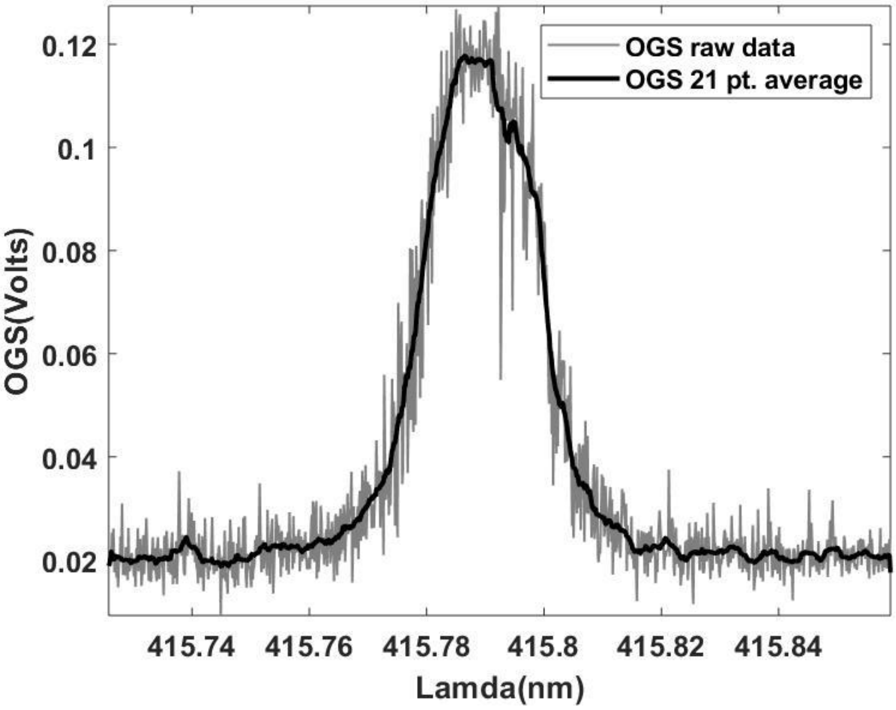

Figure 6. 6 Slow optogalvanic signal with both dye lasers on – scanning the FL2002 laser. The TDL50 laser wavelength was fixed at 379.933 nm.

6.5 Fast Optogalvanic Signal

For the fast signal measurements both dye lasers were once again directed into the hollow cathode lamp (HCL). The output beam of the FL2002 dye laser passed through the lens on its righthand side and was focused close to the lamp cathode. Since a good position of the laser beam on the hollow cathode had already been found with the other dye laser, a first order alignment of the FL2002 laser beam was obtained by simply superposing its focal spot to that of the TDL50 laser.

For this purpose, a prism was mounted in front of the lamp entrance to deflect the beams toward a reference screen. The screen distance to the prism was the same as the distance between the cathode and the prism so that if the spots were superimposed on the screen, then they were also overlapping on the lamp cathode. In this way, it was sufficient to adjust the lower mirror of the periscope to move the observed spot of the FL2002 laser onto the spot of the other laser.

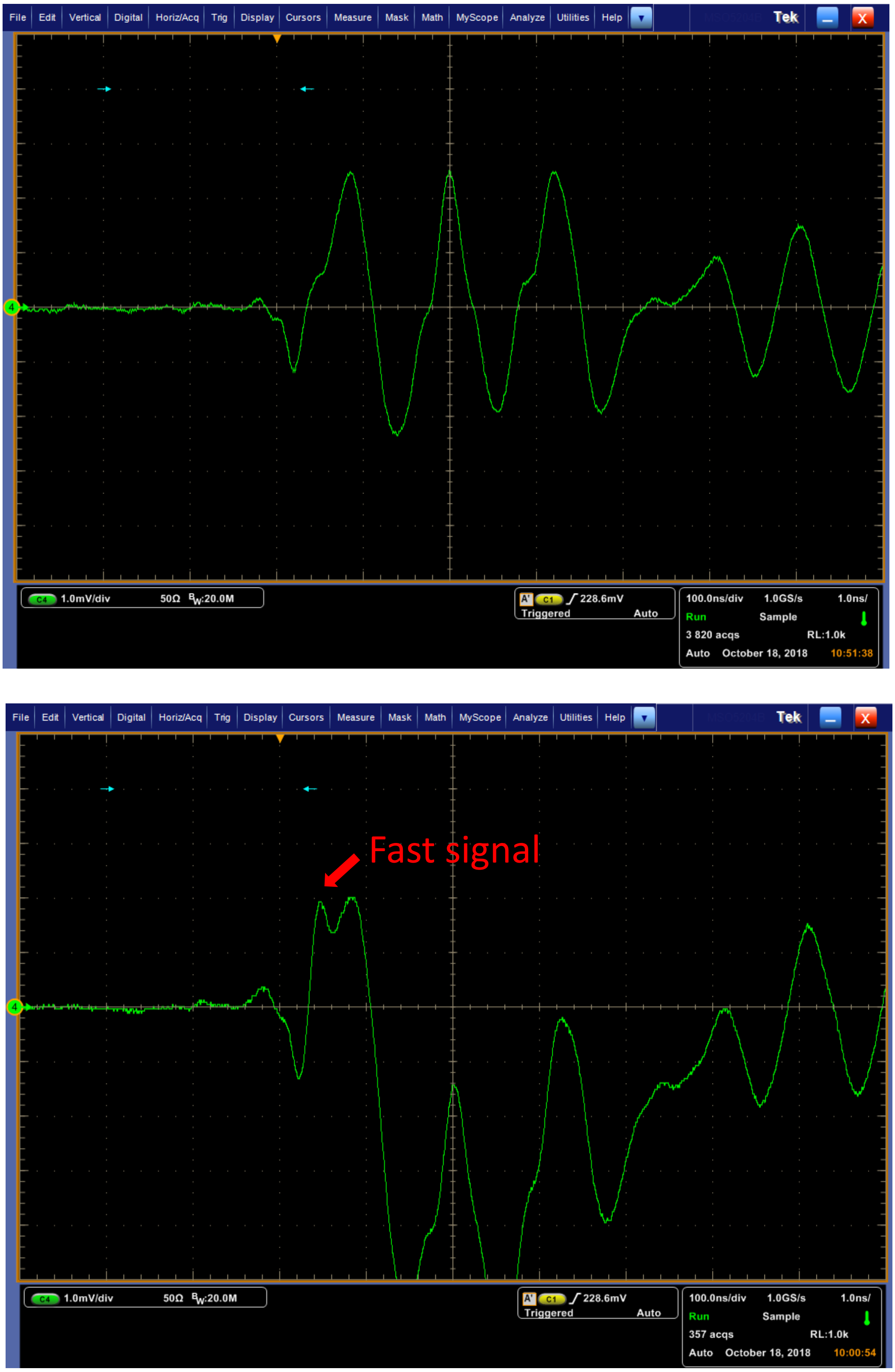

C4 1.0mV/div 50Ω B_W:20.0M

A' C1 ∕ 228.6mV
Triggered Auto

100.0ns/div 1.0GS/s 1.0ns/
Run Sample
3 820 acqs RL:1.0k
Auto October 18, 2018 10:51:38

C4 1.0mV/div 50Ω B_W:20.0M

A' C1 ∕ 228.6mV
Triggered Auto

100.0ns/div 1.0GS/s 1.0ns/
Run Sample
357 acqs RL:1.0k
Auto October 18, 2018 10:00:54

Figure 6. 7 Fast optogalvanic signal collected by the oscilloscope with both lasers on (the top panel is background while the bottom panel shows the fast signal).

Once a measurable signal was observed, further adjustments on the position of the laser beam were performed looking at the oscilloscope display. A very first check was then to verify that the signal, associated in principle with the ionization of the sputtered molybdenum atoms, was actually produced by the combination of the two dye lasers. Indeed, the signal appeared only with both lasers in the lamp. The frequency tunability was then tested by manually scanning the output wavelength of the two dye lasers, as in the case of the slow optogalvanic signal. Automatic scans of the two laser wavelengths, driven by the dedicated MATLAB® programs, were performed in order to set them to the values corresponding to the maximum detected signal. The output average power of the FL 2002 dye laser was set to a value of 1.6 mW, 160 μJ/pulse, measured in front of the lamp.

The last parameter to be optimized was the delay between the output pulses of the two dye lasers. The delay was varied within 2-3 ns until the fast signal amplitude increased to a maximum. The hollow cathode lamp was operated once again at a supply current of 18 mA.

Fig. 6.7 (top panel) shows the signal on the oscilloscope in the case where the FL 2002 dye laser is on and TDL50 laser is switched off. In this case resonance photoionization of sputtered molybdenum atoms cannot occur, as the first resonant transition is not excited. However, when both dye lasers are on, as shown on Fig. 6.7 (bottom panel), a new positive peak (denoted as the fast signal, indicated by a red arrow and labelled with red text), appears. In practice the trace in the upper panel of Fig 6.7 (the background) is subtracted from the trace in the lower panel to obtain the net fast optogalvanic signal. This peak value of this signal is then used to construct the scans shown in Figs. 6.8 and 6.9 below. The time base on the oscilloscope is 100 ns per division in this case, to be contrasted with 10 μsec/div for the slow optogalvanic signals.

Subsequently, automatic scanning of the two dye lasers wavelengths was performed in order to study the wavelength dependence of the fast optogalvanic signal. Fig. 6.8 is the result of scanning the wavelength of the TDL50 dye laser while keeping the second (FL2002) laser at a fixed wavelength of 415.90 nm corresponding to the second step 4d^5(^{6}S)5p $^7P_4$ - 4d^5(^{6}S)6d $^7D_5$ transition. Again, the scanning window was set to 0.05 nm. The computed maxima of the acquired signal are plotted versus the laser output wavelength. The 21 adjacent point average plot exhibits a FWHM of ~0.01 nm at a peak wavelength of 379.955 nm, in good agreement with the linewidth obtained by scanning the TDL50 wavelength in the case of the slow optogalvanic signal. What is most striking is that the peak of the electron signal in this case is only ca. 15 mV or some five times lower than in the slow signal case. One can only conclude that the collection efficiency of electrons is lower than for ions since the dominant charge state is expected to be singly ionized Mo and so the ion and electron densities due to photoionization should be comparable. One would not expect the Ne ion and electron densities to be significantly affected by laser ionization as the ionization potential for Ne is so high and the lasers are not resonant with any Ne or Ne ion states.

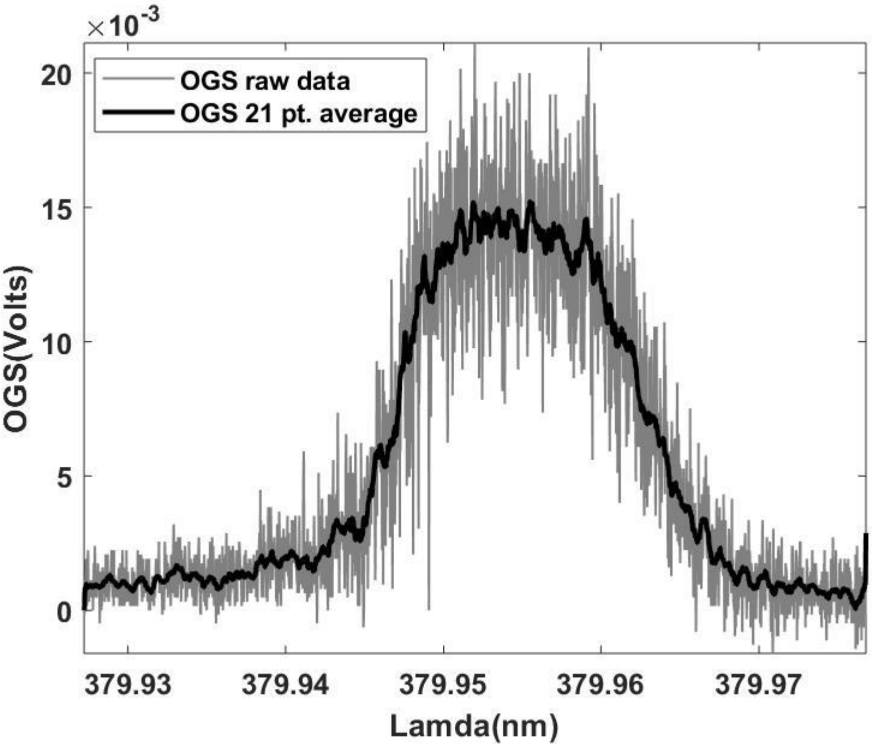

Figure 6. 8 Fast optogalvanic signal with both dye lasers on – scanning the TDL50 laser. The second dye laser (FL2002) was set to a wavelength of 415.90 nm.

Fig. 6.9 shows the wavelength dependence of the maximum amplitude of the fast optogalvanic signal acquired while scanning the FL2002 dye laser wavelength. The scanning window was set to 0.12 nm. In this case, the wavelength values that are provided by the laser control electronics and subsequently used to build the horizontal scale of the plot are first corrected by the program to a value that considers the actual grating order. The FWHM from a 21 adjacent point average plot is ca. 0.023 nm and the peak wavelength is 415.912 nm, the latter being given by the laser software is not accurate. The true wavelength measured with a wavemeter is 415.90 nm. Once again, the collected electron signal is lower than the ion signal, and in this case, the peak value is ca. 6 mV and hence lower by a factor of >2 compared to Fig. 6.8. As the corresponding ion signals for both cases are comparable, it is concluded that in this case that it is the electron collection efficiency is lower and likely not the electron density. The exact mechanism for the differences observed in the electron signals remains to be elucidated.

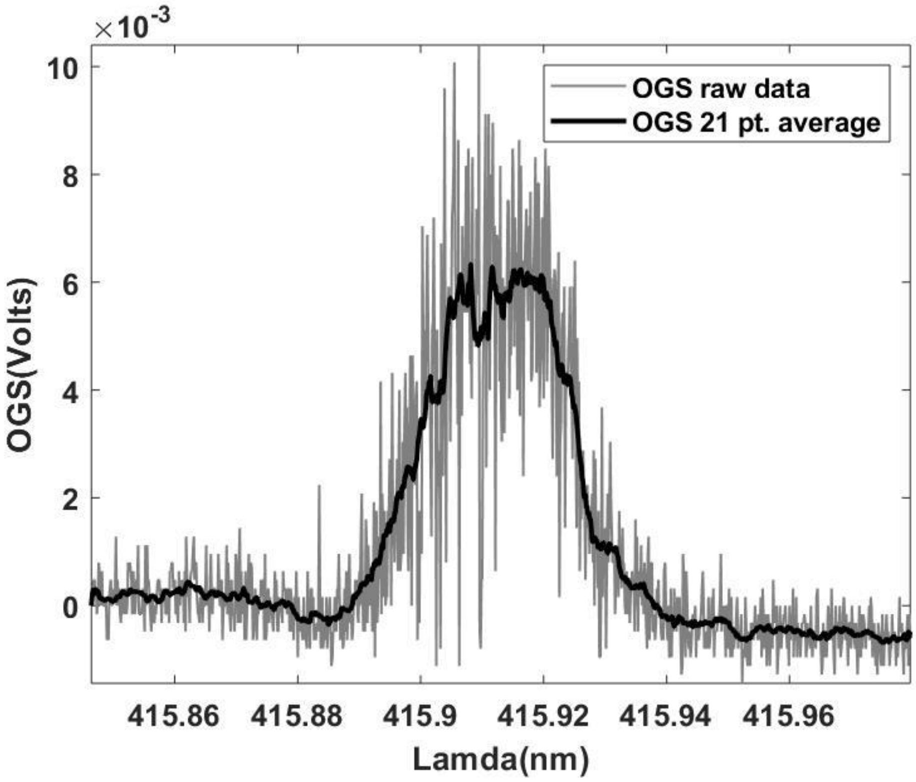

Figure 6. 9 Fast optogalvanic signal with both dye lasers on – scanning the FL2002 laser. The first dye laser (TDL50) was set to a wavelength of 379.933 nm.

6.6 Conclusions

This work presents first results on molybdenum laser resonant ionization studied by means of a hollow cathode lamp and optogalvanic signals in the SPES laser laboratory in Laboratori Nazionali di Legnaro. The SPES project, once online, will make extensive use of the resonant laser ionization process as the ionization technique for ion beam production in order to provide isotope selected ion beams of high selectivity and ideally high current. Thus, offline studies, like the one reported here, are key to the project development and success.

Results in this work confirm the possible use of HCL as a cheap spectroscopic investigation tool. In particular its use in the optogalvanic mode of operation allows the user to precisely, easily and reliably tune the wavelength of one or more lasers to resonances of interest for experiments in the general domain of atomic vapour laser isotope selection (AVLIS). In particular resonant ionization laser isotope selection (RILIS) will be facilitated at SPES.

Secondly, it allows for the exploration of the resonant excitation-ionization scheme that is most efficient in RILIS for particular atomic isotopes. This is done by monitoring the slow optogalvanic signal and its dependence on the transitions chosen for each excitation (or ionization) step to obtain the highest possible ion signal collected. The first step transition selected for this work, $4d^5(^6S)5s\,^7S_3$ - $4d^5(^6S)5p\ ^7P_4$ at 379.933 nm was chosen as the NIST Atomic Lines database gives it as the strongest transition on the UV-Vis spectrum of Mo. However, data for transitions ending on excited states are not as plentiful. The second step transition was determined by first having to use the excited $4d^5(^6S)5p\ ^7P_4$ at state as the lower state and therefore the $4d^5(^6S)5p\ ^7P_4$ - $4d^5(^6S)6d\ ^7D_5$ transition was chosen as the second step. The second step is stated to be some 300 times weaker than the first step in the NIST database. However, these line strengths are often not measured and therefore both atomic structure calculations and further experiments like the one reported here are of value.

References

[1] M. Iannelli, Study on laser resonance photoionization of molybdenum atoms. Masters Thesis, University of Pavia, 2017

[2] D. Scarpa, A. Barzakh, D. Fedorov, A. Andrighetto, E. Mariotti, P. Nicolosi, and A. Tomaselli, First results on Ge resonant laser photoionization in hollow cathode lamp. *Rev. Sci. instrum.* **87**, 02B708 (2016)

[3] P. A. Bokhan, V. V. Buchanov, N. V. Fateev, M. M. Kalugin, M. A. Kazaryan, A. M. Prokhorov, D. E. Zakrevskii, *Laser Isotope Separation in Atomic Vapor*. Wiley-VCH, Berlin, August 2006

[4] D. Scarpa, D. Fedorov, A. Andrighetto, E. Mariotti, P. Nicolosi, L. Sottili, A. Tomaselli, R. Cecchi and L. Stiaccini, ToF diagnostic of Tin resonant laser photoionization in SPES laser offline laboratory. IOP Publishing Ltd and Sissa Medialab srl. 2016

[5] B. W. Tordoff, Development of Resonance Ionization Techniques at the Jyväskylä IGISOL. PhD thesis, University of Manchester, 2007

[6] G. S. Hurst, M. G. Payne, S. D. Kramer, J. P. Young, Resonance ionization spectroscopy and one-atom detection. *Rev. Mod. Phys*. **51**,767 (1979)

[7] M. Broglia, F. Catoni and P. Zampetti, Temporal behaviour of the optogalvanic signal in a hollow cathode lamp. *J. Phys. Colloq.* **44,** C7-479 (1983)

[8] R. B. Green, R. A. Keller, G. G. Luther, P. K. Schenck, and J. C. Travis, Galvanic detection of optical absorptions in a gas discharge. *Appl. Phys. Lett.* **29**, 727 (1976)

[9] J. E. Lawler, Experimental and theoretical investigation of the optogalvanic effect in the helium positive column. *Phys. Rev. A* **22**, 1025 (1980)

[10] J. M. Pendlebury and D. B. Ring, Ground state hyperfine structures and nuclear quadrupole moments of ^{95}Mo and ^{97}Mo. *J. Phys. B: Atom. Mol. Phys.* **5,** 386 (1972)

[11] G. Olsson, T. Olsson, L. Robertsson and A. Rosén, Laser and radiofrequency spectroscopy of the hyperfine structure in the $4d^45s^2\ ^5D_{3,4}$ and $4d^55p^7\ P_{2,3,4}$ States in Mo I. *Phys. Scr.* **29,** 61 (1984)

Chapter 7 Conclusions and Future Work

7.1 Summary of the Work

The main aim of this work was to investigate the photoionization of metal atoms in UV and VUV regions. Two different experiments were performed to study the photoabsorption of Pb and Bi and laser resonant ionization of Mo, respectively. The dual laser plasma technique was successfully employed to measure the photoabsorption spectra of neutral and lowly charged ions of lead and bismuth. The spectra were recorded on a 1 metre normal incidence vacuum ultraviolet (VUV) spectrometer system built at DCU [1]. In order to record almost pure spectra of the species of interest and distinguish the absorption features observed, the experimental conditions were established to maximise the population of a particular ion stage, as a function of time and space. The photoabsorption spectra of Pb I, Pb II, Bi I, Bi II and Bi III in the 37-121 nm wavelength region were presented in the first part of chapter 5. Calculations with a relativistic time dependent local density approximation (RTDLDA) code [2] were carried out to reproduce the overall spectral shapes of the neutral photoabsorption spectra of Pb and Bi. Some lines of Pb II, Bi II and Bi III photoabsorption spectra were also identified by comparing the current experimental data with a series of papers [3-12].

In the second part of chapter 5, the photoabsorption measurements of Pb II, Bi II and Bi III in the 37-70 nm spectral region are reported. Prior to the present work, there were no spectroscopic data for this wavelength region available on excited state photoabsorption by Pb^{+}, Bi^{+} and Bi^{2+}, to the best of the author's knowledge. The Cowan suite of atomic structure codes was used to help identify the absorption features here. The findings suggest that 5d subshell photoabsorption from a number of states belonging the ground electronic configuration and some low-lying excited configurations dominate the spectrum in this wavelength region. The synthetic spectra of Pb II, Bi II and Bi III, which were constructed by a convolution of the gf values with a Gaussian function representing the instrumental broadening, were compared with the experimental spectra. The transitions corresponding to the most prominent features observed in the absorption spectra were listed in tables. Evidence of the presence of low-lying excited levels was provided with the aid of the Cowan suite of atomic structure codes [13].

The second experiment on two colour resonant laser photoionization of Mo in a hollow cathode lamp was carried out in the SPES laser laboratory at Laboratori Nazionali di Legnaro. For the first step, the transition ($4d^5(^6S)5s\ ^7S_3$ - $4d^5(^6S)5p\ ^7P_4$) of Mo was selected as it is the strongest Mo transition in the near UV to visible spectral range. For the second step transition, $4d^5(^6S)5p\ ^7P_4$ - $4d^5(^6S)6d\ ^7D_5$, was chosen as it connected well with the first step transition and was within the wavelength range of the second dye laser. Slow and fast optogalvanic signals were measured in the molybdenum hollow cathode lamp by scanning the wavelength of one of the two dye lasers while the wavelength of the other dye laser was fixed. The work confirms that HCLs can be used as an easy to use and economic spectroscopic tool to tune the wavelength of one or more lasers to resonances of interest and also to investigate the resonant excitation-ionization schemes for resonant ionization laser isotope selection (RILIS) [14].

7.2 Future Work

With the development of third generation synchrotron sources such as SOLEIL [15], ALS [16] and PETRA III [17], new data on absolute cross sections have been produced with spectral resolution approaching the sub meV level, much better than the dual laser plasma (DLP) technique. However, the significant advantage of the DLP technique is that it can quickly provide vacuum-UV and extreme-UV photoabsorption spectra of atoms and ions over wide spectral ranges with just a few laser shots. Thus the DLP technique can guide merged-beam experiments that can in turn provide absolute cross sections with high spectral resolution.

Clearly experiments on Pb II, Bi II and Bi III photoabsorption spectra can be extended to more highly charged ions to study the effect of increasing ionization on the degree of localisation on the atomic orbitals and the effect on the oscillator strength distributions (isonuclear sequences). It would be interesting to measure the photoabsorption spectra of other elements in the same row of the periodic table to study the contributions of excited states and also to look at isoelectronic sequences and the trends in the spectral redistribution of oscillator strengths along such sequences.

For the resonant laser photoionization experiment of Mo, further experiments can be carried out to investigate the effects of varying the dye laser power and the choice of transitions for both first and second step excitations. The former allows to test for line broadening due to saturation [18]. The latter is currently dependent on the use of the NIST database where many of the transition strengths given are not accurate since they come from different light sources, spectrometer systems and detectors, from photographic plates to CCD cameras. Hence, a much more extensive search and study of the literature, combined with Cowan code calculations (benchmarked against critically evaluated spectra), should allow for the selection of other possible transitions to optimise RILIS of Mo.

The second step transition (5p – 6d) at 415.80 nm (in air) is likely not the optimal one but was chosen due to available laser wavelengths and time constraints. The most recent data online strengths in Mo [19] shows that 5p – 5d at 536.05 nm (in air) is almost a factor of five stronger and should be investigated in the next set of experiments at the SPES laboratory.

References

[1] E. P. O'Leary, VUV Laser-Induced Plasma Spectroscopy for Low Level Sulphur Detection in Steel. PhD thesis, Dublin City University, 2007

[2] D. A. Liberman and A. Zangwill, A relativistic program for optical response in atoms using a time dependent local density approximation. *Comput. Phys. Commun.* **32,** 75 (1984)

[3] J. P. Connerade, W. R. S. Garton, M. W. D. Mansfield and M. A. P. Martin, Interchannel interactions and series quenching in the 5d and 6s spectra of Pb I. *Proc R Soc London Ser A* **357**, 499 (1977)

[4] M. F. Crawford and A. B. McLay, Spark spectra of bismuth, Bi III and Bi II. *Proc. R. Soc. Lond. A* **143,** 540 (1934)

[5] M. Mazzoni, Y. N. Joshi, A. Nencioni, T. Grisendi and W. H. Parkinson, Photoabsorption spectrum of atomic bismuth in the vacuum ultraviolet region. *J. Phys. B: At. Mol. Phys.* **20,** 2193 (1987)

[6] R. K. Yoo, B. Ruscic and J. Berkowitz, Photoionization of atomic bismuth. *J. Phys. B: At. Mol. Opt. Phys.* **28,** 1743 (1995)

[7] Y. N. Joshi and M. Mazzoni, The $6s^26p^2$ $^3P_0$-$6S^26pnd$ $^3D_1$, series in photoabsorption of BI II. *Phys. Rev. A* **118**, 237 (1986)

[8] M. Andrzejewska, F. G. Meijer and E. Stachowska, On the level system of Bi II. *J. Phys. B: At. Mol. Opt. Phys.* **46**, 205003 (2013)

[9] G. M. Wahlgren, T. Brage, J. C. Brandt, J. Fleming, S. Johansson, D. S. Leckrone, C. R. Proffitt, J. Reader and C. J. Sansonetti, The bismuth abundance in the HgMn stars χ Lupi and HR 7775 and improved atomic data for selected transitions of Bi I, Bi II, and Bi III*. *ApJ,* **551**, 520 (2001)

[10] L. T. Earls and R. A. Sawyer, The classification of the first spark spectrum of lead: Pb II. *Phys. Rev.* **47**, 115 (1935)

[11] S. J. Smith, A note on the spectra of doubly and trebly ionized lead. *Phys. Rev.* **36**, 1 (1930)

[12] A. S. Rao and A. L. Narayan, Über das Zweite Funkenspektrum des Bleies. *Z. Phys.* **59**, 687 (1930)

[13] Cowan R D 1982 The Theory of Atomic Structure and Spectra. (University of California Press)

[14] P. A. Bokhan, V. V. Buchanov, N. V. Fateev, M. M. Kalugin, M. A. Kazaryan, A. M. Prokhorov, D. E. Zakrevskii, Laser Isotope Separation in Atomic Vapor. Wiley-VCH, Berlin, August 2006

[15] M. F. Gharaibeh, J. M. Bizau, D. Cubaynes, S. Guilbaud, N. El Hassan, M. M. Al Shorman, C. Miron, C. Nicolas, E. Robert, C. Blancard and B. M. McLaughlin, K-shell

photoionization of singly ionized atomic nitrogen: experiment and theory. *J. Phys. B At. Mol. Opt. Phys.* **44,** 175208 (2011)

[16] A. M. Covington, A. Aguilar, I. R. Covington, M. F. Gharaibeh, G. Hinojosa, C. A. Shirley, R. A. Phaneuf, I. Álvarez, C. Cisneros, I. Dominguez-Lopez, M. M. Sant'Anna, A. S. Schlachter, B. M. McLaughlin, and A. Dalgarno, Photoionization of Ne^+ using synchrotron radiation. *Phys. Rev. A* **66,** 062710 (2002)

[17] S. Schippers, S. Ricz, T. Buhr, J. Hellhund, A. Müller, S. Klumpp, M. Martins, R. Flesch, E. Rühl, J. Lower, T. Jahnke, D. Metz, L. Ph H. Schmidt, R. Dörner, J. Ullrich and A. Wolf, Photon-ion spectrometer PIPE at the Variable Polarization XUV Beamline of PETRA III. *J. Phys. Conf. Ser.* **388,** 142016 (2011)

[18] D. Scarpa, A. Barzakh, D. Fedorov, A. Andrighetto, E. Mariotti, P. Nicolosi, and A. Tomaselli, First results on Ge resonant laser photoionization in hollow cathode lamp. *Rev. Sci. instrum.* **87**, 02B708 (2016)

[19] W. Whaling and J. W. Brault, Comprehensive Transition Probabilities in Mo I. *Phys. Scr.* **38**, 707 (1988)

Appendix A: Cowan's Suite of Atomic Structure Codes

Cowan's suite of atomic structure codes [1] is one of the mostly widely utilised and available numerical computer codes for atomic structure calculations. The suite comprises a number of FORTRAN programs created at Los Alamos by Robert Cowan in 1968. The code uses the Hartree-Fock method to obtain approximate solutions to the Schrödinger equation for either single or multi-electron configurations in any atom or ion. The code structure is shown in Fig. 1.

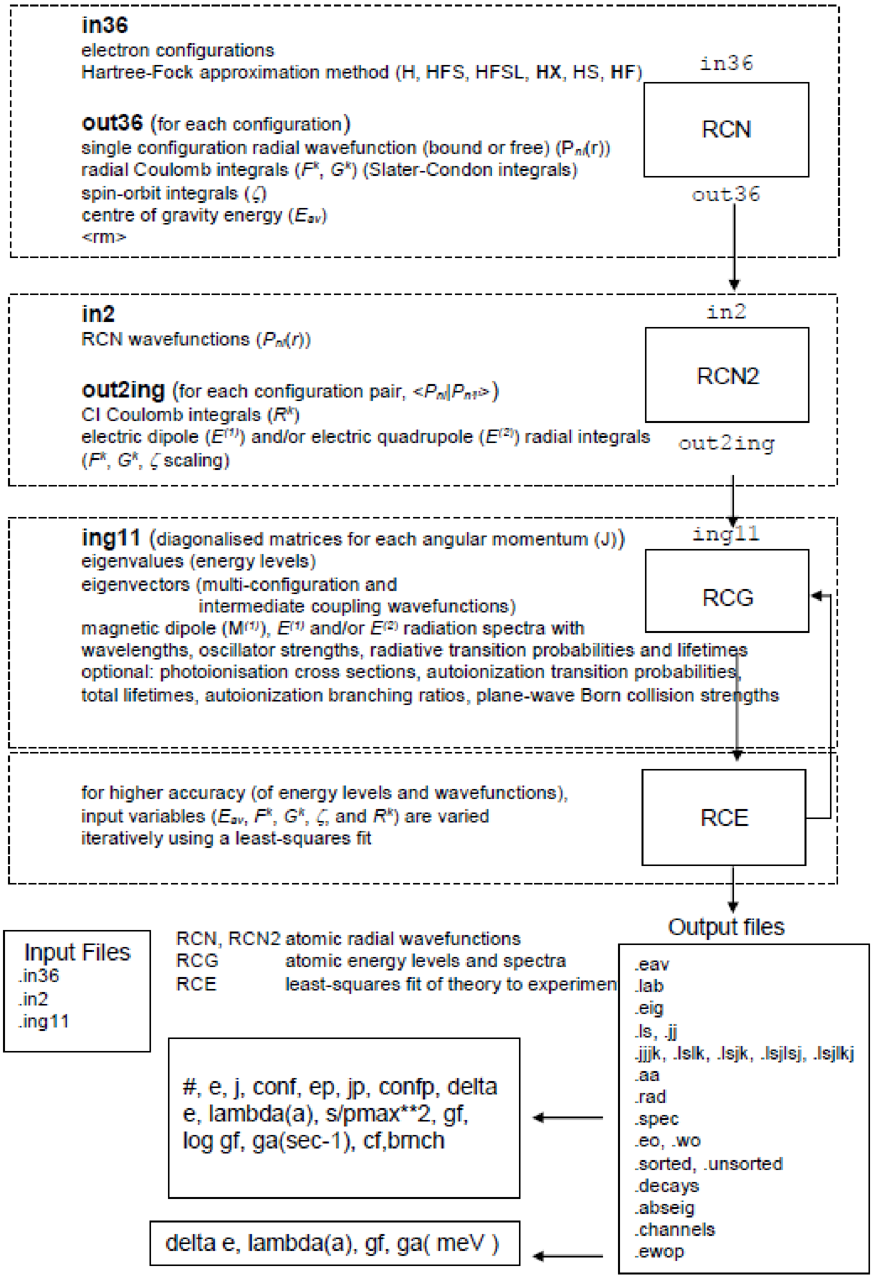

Figure 1. Diagram for the Cowan code [2].

The Cowan code contains four sub-codes: RCN, RCN2, RCG and RCE [3].

The RCN Code

The RCN code uses Hartree-Fock methods to calculate one-electron radial wavefunctions (bound or free) for each of any number of specified electron configurations. The primary output consists of the center-of-gravity energy (E_{av}) for each configuration, and those radial Coulomb (F^k and G^k) and spin-orbit (ς) integrals required to calculate the energy levels for that configuration. The input file required by the code is an ascii text file named in36 which contains descriptions of the electronic configurations for which the radial wavefunctions should be calculated. The results of these calculations are then stored for use by the RCN2 code in a binary file called tape2n. The RCN program also produces a text output file called out36. Fig. 2 is an example of the input file in36.

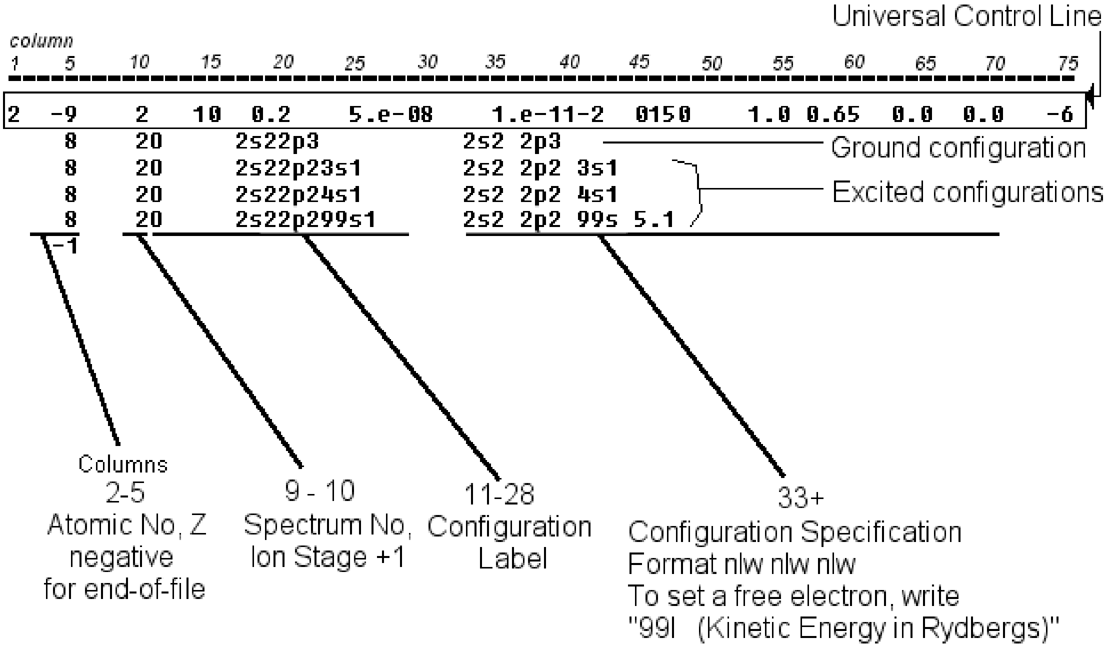

```
2  -9    2   10  0.2    5.e-08    1.e-11-2 0150      1.0 0.65  0.0  0.0   -6
    8   20      2s22p3          2s2 2p3
    8   20      2s22p23s1       2s2 2p2 3s1
    8   20      2s22p24s1       2s2 2p2 4s1
    8   20      2s22p299s1      2s2 2p2 99s 5.1
   -1
```

Figure 2. A sample 'in36' input file [1].

The RCN2 Code

The RCN2 program uses the output wave-functions from RCN (contained in a file called tape2n) to calculate the configuration-interaction Coulomb integrals (R_k) between each pair of interacting configurations. In addition, the electric-dipole ($E^{(1)}$) and/or electric quadrupole ($E^{(2)}$) radial integrals between each appropriate pair of configurations are also calculated. There are two input files required for the execution of the RCN2 code. The first is an ascii text file named in2 in which certain options can be set for the execution of the code. The most important of these is the ability to scale the radial integrals which are calculated. The second (binary) input file is called tape2n and contains the actual radial wavefunctions required to calculate the radial integrals. As noted earlier this file is produced by the RCN program. RCN2 prepares an output file called out2ing that (after being renamed ing11) serves as input to RCG. The RCN2 program also produces an ascii text output file called out2.

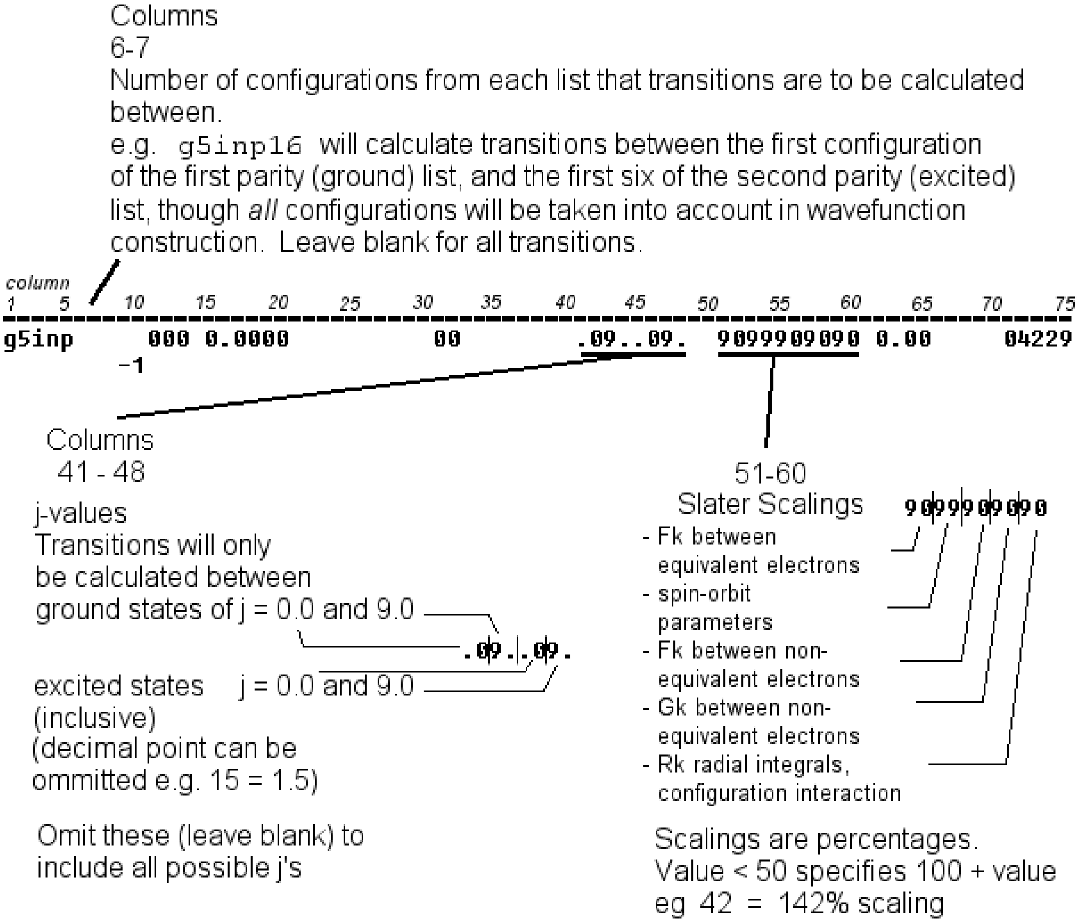

Figure 3. A sample ‘in2’ file [2].

The RCG code

The RCG program sets up energy matrices for each possible value of the total angular momentum J and diagonalizes each matrix to get eigenvalues (energy levels) and eigenvectors (term/configuration mixing amplitudes). It then computes electric dipole radiation spectra, with wavelengths, oscillator strengths, radiative transition probabilities and radiative lifetimes. The output file created by the RCG code is named outg11. This file contains almost all relevant information about the calculation which has been performed.

The RCE code

Not used as part of this thesis but the RCE program can be used to vary the various radial energy parameters E_{av}, F_k, G_k, ς, and R_k to make a least-squares fit of experimental energy levels by an iterative procedure. The resulting least-squares-fit parameters can then be used to repeat the RCG calculation with the improved energy levels and wavefunctions. The input files required for RCE are produced when appropriate options are set in the input to the RCG program. These input files are called tape2e and tape19. A third input file is called ine20. The output produced by RCE is named oute20.

References

[1] R. D. Cowan R D, The Theory of Atomic Structure and Spectra. University of California Press (1982)

[2] Cracking the Cowan Code: A beginner’s guide. SPECLAB UCD, Ireland

[3] C. McGuinness, The Cowan code utilities: Description and Usage (https://www.tcd.ie/Physics/people/Cormac.McGuinness/Cowan/)

Outputs arising to date from the work.

Journal articles arising from the work.

The 5d - 6p VUV photoabsorption spectrum of Bi⁺
H. Lu, L. Varvarezos, P. Hayden, E. T. Kennedy, J.-P. Mosnier and J. T. Costello, *Atoms* **8**, 55. (2020)

The 5d-6p EUV photoabsorption spectra of Bi III and Pb II: evidence of excited states
H. Lu, L. Varvarezos, M. B. Alli, P. Nicolosi, J. T. Costello and P. Hayden, *J. Phys. B: At. Mol. Opt. Phys.* **53**, 115001. (2020)

Conference paper arising from the work.

VUV photoabsorption spectra of Pb and Bi ions using dual laser plasma technique,
H. Lu, P. Hayden, P. Nicolosi and J. T. Costello, *Journal of Physics: Conference Series* **1289**, 012035 (2019)

Conference presentations arising from the work.

Photoionization Cross Section of Calcium Computed using TDLDA and RTDLDA Codes,
H. Lu, P. Hayden, W. Brocklesby and J. T. Costello, ALPS 2015, Warsaw, July 6 – 9 (2015)

Photoabsorption in Laser Produced Short and Ultrashort Duration UV and VUV Laser Fields,
H. Lu, P. Hayden, M. Kelly, B. Brocklesby and J. T. Costello, Photonics Ireland, Maryborough House Hotel, Cork, Ireland, September 2 – 4 (2015)

Photoabsorption of Ca, Pb and Bi in the Vacuum Ultraviolet Region – Towards Controlled Resonance-Enhanced High Harmonic Generation,
H. Lu, P. Hayden, W. S. Brocklesby and J. T. Costello, 44th IOP Plasma Physics Conference, University of Oxford, Oxford, UK, 3 - 6 April (2017)

VUV Photoabsorption Spectra of Pb and Bi Ions Using Dual Laser Plasma Technique,
H. Lu, P. Hayden, P. Nicolosi and J. T. Costello, 24th International Conference on Spectral Lineshapes, ICSLS2018, DCU, Dublin 17 – 22 June (2018)

Other papers.

Oxygen K-shell photoabsorption spectra of photoionized CO_2 plasmas,
L. Varvarezos, **H. Lu**, J. T. Costello, A. Bartnik, P. Wachulak, T. Fok, L. Wegrzynski and H. Fiedorowicz, *J. Phys. B At. Mol. Opt. Phys.* **53**, 105701. (2020)

Soft X-ray photoabsorption spectra of photoionized CH_4 and CO_2 plasmas,
L. Varvarezos, **H. Lu**, J. T. Costello, A. Bartnik, P. Wachulak, T. Fok, L. Wegrzynski and H. Fiedorowicz, J. Phys. B At. Mol. Opt. Phys. **53**, 045701. (2019)